Journal of Materials Chemistry A

REVIEW

View Article Online
View Journal | View Issue

Check for updates

Cite this: J. Mater. Chem. A, 2024, 12, 8014

Challenges and opportunities for characterisation of high-temperature polymer electrolyte membrane fuel cells: a review

Adam Zucconi, [ab] Jennifer Hack,[ac] Richard Stocker,[d] Theo A. M. Suter, [a] Alexander J. E. Rettie *[a] and Dan J. L. Brett *[a]

High-temperature (120–200 °C) polymer electrolyte membrane fuel cells (HT-PEMFCs) are promising energy conversion devices that offer multiple advantages over the established low-temperature (LT) PEMFC technology, namely: faster reaction kinetics, improved impurity tolerance, simpler water and thermal management, and increased potential to utilise waste heat. Whilst HT- and LT-PEMFCs share several components, important differences in the membrane materials, transport mechanisms and operating conditions provide new challenges and considerations for characterisation. This review focuses on phosphoric acid-doped HT-PEMFCs and provides a detailed discussion of the similarities and differences compared to LT-PEMFCs, as well as state-of-the-art performance and materials. Commonly used characterisation techniques including electrochemical, imaging, and spectroscopic methods are reviewed with a focus on use in HT-PEMFCs, how experimentation or analyses differ from LT-PEMFCs, and new opportunities for research using these techniques. Particular consideration is given to the presence of phosphoric acid and the absence of liquid water. The importance of accelerated stress tests for effective characterisation and durability estimation for HT-PEMFCs is discussed, and existing protocols are comprehensively reviewed focusing on acid loss, catalyst layer degradation, and start-up/shutdown cycling. The lack of standardisation of these testing protocols in HT-PEMFC research is highlighted as is the need to develop such standards.

Received 9th November 2023
Accepted 20th February 2024

DOI: 10.1039/d3ta06895a

rsc.li/materials-a

Open Access Article. Published on 07 March 2024. Downloaded on 1/20/2026 7:35:49 PM.
This article is licensed under a Creative Commons Attribution 3.0 Unported Licence.

[a]Electrochemical Innovation Lab, Department of Chemical Engineering, UCL, London WC1E 7JE, UK. E-mail: a.rettie@ucl.ac.uk
[b]Mobility Innovation Hub, HORIBA MIRA, Nuneaton, Warwickshire, CV10 0TU, UK
[c]Department of Materials Science & Engineering, University of Sheffield, Sir Robert Hadfield Building, Mappin Street, Sheffield S1 3JD, UK
[d]HORIBA Instruments Inc., 2890 John R Rd, Troy, Michigan, 48083, USA

Adam Zucconi

Adam Zucconi is a research scientist at HORIBA, and part-time PhD researcher in the Department of Chemical Engineering at UCL. His main research focuses on in situ and operando characterisation of fuel cells and electrolysers, principally low- and high-temperature polymer electrolyte membrane technologies. He has particular interest in electrochemical and exhaust liquid and gas characterisation.

Jennifer Hack

Dr Hack is a Royal Academy of Engineering Research Fellow in the Department of Materials Science and Engineering at the University of Sheffield, UK. She completed her PhD at University College London in 2021 working on fuel cell characterisation. After undertaking an EPSRC Doctoral Prize Fellowship studying zinc–air batteries, followed by a Project Lead role on the Faraday Institution's LiSTAR project, Jennifer joined the University of Sheffield in 2023. Her research focuses on the study of morphology evolution in electrochemical devices, in particular electrolysers and fuel cells, using in situ and operando X-ray and neutron CT.

This journal is © The Royal Society of Chemistry 2024

Open Access Article. Published on 07 March 2024. Downloaded on 1/20/2026 7:35:49 PM. This article is licensed under a Creative Commons Attribution 3.0 Unported Licence.

1. Introduction

1.1 Emergence of PEMFCs

The global dependency on fossil fuels to provide energy has many disadvantages including high carbon and pollutant emissions (CO_2, NO_x, SO_x, particulate matter, *etc.*),[1–4] evidence of a causal link between economic growth, higher mortality rates and environmental degradation,[4–8] fossil fuel price fragility and general increasing price trend,[9–11] and higher economic costs due to trends in climate policy favouring non-fossil fuel markets and carbon taxes.[12,13] Renewable energy combined with electrified power systems is experiencing rapid growth in light of these issues.[14–16]

Polymer electrolyte membrane (also called proton exchange membrane) fuel cells (PEMFCs) are a promising energy conversion technology. These fuel cells convert the chemical energy of the fuel (hydrogen) and oxidant (oxygen) to electrical energy and heat, with water as the waste product. PEMFCs are favoured for applications that require fast start-up, high power density, zero local carbon emissions, low operating temperature, and the use of air as the oxidant.[17,18] Such devices already have an established presence in niche markets such as material handling and remote/back-up power,[19,20] and are expected to play a key role in the decarbonisation of heating, power, and transport.[19] Over 60% of fuel cell units shipped in 2022 were estimated to be PEMFCs, making up 86% of the total fuel cell power output shipped that year.[21]

The technology can be separated into two categories: (i) low-temperature (LT-PEMFC), and (ii) high-temperature (HT-PEMFC). The former is typically operated at 60–80 °C, with the latter operating at 120–200 °C.[22] PEMFCs that operate at 100–120 °C are sometimes referred to as intermediate-

Richard Stocker

Dr. Richard Stocker is a Principle Engineer at HORIBA Instruments Inc. In his 10 years at HORIBA he has focused on Li-ion battery pack projects, including BMS development, cell characterization testing, and simulation modelling. Graduating from the University of Nottingham with a MEng in Mechanical Engineering (2013), they furthered their specialization with a PhD from Coventry University (2020), investigating Li-ion battery cell ageing and developing algorithms to decode ageing mechanisms from electrical cycling data. He has investigated the use of Electrochemical Impedance Spectroscopy (EIS) and Distribution of Relaxation Times (DRT) as applied to batteries and fuel cells.

Alexander J. E. Rettie

Alex Rettie is an Associate Professor in Electrochemical Conversion and Storage in the Department of Chemical Engineering, UCL (UK). His interests are in the experimental discovery and characterisation of electrochemical energy materials and their incorporation into devices, with a focus on electronic and ionic charge transport. He leads a national hydrogen network based at UCL and is the UK's alternate delegate to the IEA's technology collaboration programme on hydrogen.

Theo A. M. Suter

Theo A. M. Suter is a postdoctoral researcher in the electrochemical innovation laboratory at UCL focusing on fuel cell fabrication, testing, and characterization. He completed his PhD in nanomaterial chemistry at UCL in 2018 and now specializes in nanoengineering of the fuel cell catalyst layer, particularly via the use of nanomaterials and heterogeneous catalyst layer fabrication. His interests focus on how the fuel cell catalyst layer morphology and microstructure impacts the performance of fuel cells, and how different fabrication techniques can be used as a tool to improve device durability.

Dan J. L. Brett

Dan Brett specialises in electrochemical power systems. He holds the Royal Academy of Engineering Research Chair in Metrology for Electrochemical Propulsion and is the Director of the UCL Advanced Propulsion Lab. He has co-founded companies including Bramble Energy, Oort Energy, Sention, Element 30, Gaussian and Prosemino. He has been recognised through awards including the De Nora Prize for Applied Electrochemistry (ISE), Baker Medal (ICE) and the Princess Royal Silver Medal (RAEng). He is listed in the Stanford top 2% of scientists in the world and in 2023 the Royal Academy of Engineering and TFL recognised him as an 'Engineering Icon'.

Open Access Article. Published on 07 March 2024. Downloaded on 1/20/2026 7:35:49 PM. This article is licensed under a Creative Commons Attribution 3.0 Unported Licence.

temperature (IT-PEMFCs), and can typically be grouped into two categories: (i) modified LT-PEMFCs where the membrane has been adapted to retain more water at temperatures above 100 °C, often by adding inorganic fillers; and (ii) HT-PEMFCs with phosphoric acid (PA)-doped polybenzimidazole (PBI) membranes.[23] Due to the close relation of IT-PEMFCs to LT-PEMFCs and HT-PEMFCs depending on the membrane material and proton conduction method, this technology is not specified independently in the remainder of the review.

1.2 Motivation for HT-PEMFCs

LT-PEMFCs based on conventional perfluorosulphonic acid-based membrane electrolytes suffer from relatively high membrane cost, water management issues, catalyst poisoning, and expensive precious metal catalysts.[24] Operating at temperatures above 100 °C offers potential solutions to some of these issues. The primary advantages to higher temperature operation include: increased tolerance of Pt catalysts to fuel impurities, faster reaction kinetics, easier water management, easier thermal management due to greater heat rejection resulting from the higher temperature gradient between the stack and ambient environment, and higher quality waste heat generation.[22,24–26]

1.2.1 Higher impurity tolerance. LT-PEMFCs are highly susceptible to anode poisoning. Fuel impurity concentrations as low as 10 ppm for carbon monoxide (CO) and 10 ppb for hydrogen sulphide (H_2S) can significantly reduce performance.[27–31] CO forms a strong bond with Pt, chemisorbing onto the surface. This blocks active sites for the hydrogen oxidation reaction (HOR), reducing reaction rates and increasing overpotential, resulting in lower performance.[27] This low tolerance to impurities requires hydrogen purities of 99.999% or higher, which leads to higher costs.[22] The adsorption of CO onto Pt has high negative entropy, *i.e.*, it becomes less favourable as temperature increases,[32] resulting in an impurity tolerance up to three orders of magnitude higher for HT-PEMFCs.[33–35] This tolerance allows for lower purity, cheaper hydrogen to be used, or even other fuels *e.g.*, methanol, natural gas and liquefied petroleum gas can be used in HT-PEMFCs where hydrogen infrastructure is lacking.[25,26]

1.2.2 Faster reaction kinetics. Increased temperature also benefits reaction kinetics as the HOR and oxygen reduction reaction (ORR) exchange current densities increase.[36,37] LT-PEMFCs have been reported to possess increasing intrinsic exchange current densities as temperature increases; however, the measured exchange current density may peak closer to 80 °C as Pt utilisation decreases due to Nafion dehydration at higher temperatures.[36] This problem is not reported by the same research group conducting studies of PBI HT-PEMFCs from 120–200 °C, where intrinsic and measured exchange current densities continuously increased with temperature.[37] In theory, the higher reaction kinetics should allow for a decrease in Pt loading, and therefore cost. However, current HT-PEMFCs typically have higher Pt loadings than LT-PEMFCs, approximately 1 mg cm^{-2} and 0.1–0.4 mg cm^{-2}, respectively.[38] This is discussed in more detail in Section 2.1.3.

1.2.3 Simplified water management. Water exists in both liquid and vapour states during operation of LT-PEMFCs, and is critical for proton conduction.[39–44] Electrode flooding is a common issue for LT-PEMFCs and is caused by formation and accumulation of excessive liquid water, and ultimately impedes performances.[42,45,46] Operating above the boiling point of water should result in only water vapour being present within the HT-PEMFC at pressures close to atmospheric,[47] simplifying water management. While some types of HT-PEMFCs require water for proton conduction,[48,49] the most common technology (acid-doped PBI membranes) operates under non-humidified conditions and uses PA as the proton conductor.[50] This allows the system to operate without a humidifier, which is beneficial in applications requiring small system volumes such as automotive vehicles.[50]

1.2.4 Simplified thermal management. A vehicle operating with a fuel cell stack at 80 °C with an efficiency of 40–50% requires a heat exchanger twice as large as those in conventionally powered vehicles.[25] Operating at >120 °C is sufficient to mitigate this effect,[26] because higher operating temperatures permit easier heat removal and improved energy recovery.[51] The greater temperature difference between the fuel cell and ambient environment allows for efficient heat rejection and reductions in the cooling system, improving the mass-specific and volume-specific power density.[52] The heat generated from HT-PEMFC stacks can be used for methanol and water evaporation in reformer systems.[53] However, the heat from the stack will generally not have a sufficiently high temperature to drive a reformer directly so will require upgrading for most HT-PEMFC outputs.[54]

1.3 Purpose of this review

Many of the review papers on HT-PEMFCs focus on the membrane.[24,25,55–63] While there are review papers that discuss the characterisation of materials, components, and cells,[38,47] these are limited to subsections of larger reviews. Characterisation techniques for LT-PEMFCs have been reviewed,[20,64–66] yet comprehensive assessment of characterisation for HT-PEMFCs is very limited. Due to the differences in materials, and physical and chemical processes, the diagnostic and measurement techniques also require different approaches and analyses. Combining advanced characterisation techniques with accelerated stress tests (ASTs) is critical to studying degradation and durability. The appropriate characterisation technique will also depend on the application. For example, membrane electrode assembly (MEA) research and development typically requires more detailed information across chemical, physical, and electrical domains; whereas, control or system modelling may require more concise characterisation focusing on key parameters and metrics. This review aims to condense the current understanding of how HT-PEMFCs operate with context from the LT-PEMFC field given where appropriate, and how that affects characterisation and ASTs. This is increasingly important as interest and research into HT-PEMFCs grows, and this technology moves towards commercialisation.

 This journal is © The Royal Society of Chemistry 2024

Open Access Article. Published on 07 March 2024. Downloaded on 1/20/2026 7:35:49 PM. This article is licensed under a Creative Commons Attribution 3.0 Unported Licence.

2. Materials, operation, and differences compared to LT-PEMFCs

The following section provides an overview of HT-PEMFC materials and design, highlighting the differences compared to LT-PEMFCs. This section is not intended to be a comprehensive review of materials and design, as this is well represented in other review articles.[24,25,55–63]

2.1 Materials

2.1.1 Diffusion layers. The gas diffusion electrode (GDE) of a HT-PEMFC contains a gas diffusion layer (GDL), comprising of a macroporous substrate, usually a carbon cloth or paper, and often includes a microporous layer (MPL), typically containing PTFE to increase hydrophobicity much like in LT-PEMFCs,[67] as well as a catalyst layer. Despite these similarities, there are some key differences between HT-PEMFC GDEs compared to LT-PEMFCs. For example, the MPL has an additional role in HT-PEMFCs, which is to encourage PA redistribution in the catalyst layer and inhibit leaching of PA into the GDL.[68,69] The reduction in liquid water at higher temperatures means the diffusion media are less sensitive to electrode morphology.[70] Optimised porosities for HT-PEMFCs are lower in general, typically 25–45% *vs.* 60–90% for the low-temperature technology.[71–76] GDL thicknesses are similar (200–400 μm), although modelling suggests that HT-PEMFCs may use thinner GDLs.[71,76–78]

2.1.2 Membrane. The membrane is the component that differs the most between the two technologies. LT-PEMFCs typically use perfluorosulphonic acid (PFSA) membranes. These membranes have main chains that are highly hydrophobic, and have sulphonic groups at the end of side chains that are highly hydrophilic.[79] This membrane type must be hydrated to achieve high ionic conductivity and durability, which requires humidification strategies and increased complexity of the system.[80] Operation at higher temperatures dramatically reduces the proton conductivity; therefore, different membranes are required to operate at high temperatures and anhydrous conditions.[24]

PFSA membranes have been modified to operate at higher temperatures (up to 120 °C) whilst still using water as the proton conductor.[57,81] Inorganic fillers such as graphene oxide (GO), SiO_2, TiO_2, and ZrO_2 can be added to the PFSA membrane to improve water retention and performance at higher temperatures and lower relative humidity.[81–88] Sulphonated hydrocarbon polymers are another type of membrane investigated for HT-PEMFCs. While they have advantages in mechanical and thermal properties, as well as increased water uptake, they suffer from catalyst layer delamination and membrane thinning due to dehydration under HT-PEMFC operating conditions.[67] Most crucially, both PFSA and sulphonated hydrocarbon membranes still require humidification and liquid water, which retains the complexity of the physical system and control strategy.

The most common membrane for HT-PEMFCs is PA-doped PBI-based. PA is used as the proton conductor due to its high proton conductivity under anhydrous conditions, low gas permeability, and good thermal and chemical stability.[47] Proton conductivity can be increased by increasing the acid doping level; however, this decreases mechanical strength due to the strong plasticising effect.[89–91] The actual proton conduction mechanisms are complex and depend on the water content, temperature, and amount of acid dopant. These factors affect the amount, and pathway, of conduction *via* structural diffusion (also referred to as "proton hopping" and "Grotthuss mechanism"), and *via* vehicular diffusion through H_3O^+ and $H_2PO_4^-$.[67,92,93] Despite their prevalence, PBI membranes still have unresolved issues. These include: acid leaching, reduced mechanical strength due to doping, and reduction in proton conductivities at high temperatures and low water content due to evaporation and acid condensation.[63,67,94–96] Optimisation of acid doping should maximise performance whilst maintaining mechanical strength and minimising acid loss.[67] Improvements in these areas have been achieved using PBI-based composite membranes by the use of crosslinking,[97–99] and three-layered membranes.[100] Advances have also been made with the addition of inorganic fillers,[98,101–103] heteropolyacids (HPAs),[104–106] carbon nanotubes,[107,108] and metal–organic frameworks (MOFs).[109–111]

A promising alternative to PA-PBI are ion-pair coordinated membranes, specifically quaternary ammonium functionalised polymers (QAPs). The quaternary ammonium species causes complete deprotonation of PA, enabling a strong interaction between ammonium cations and biphosphate anions.[55,112] Strong PA retention is possible at lower temperatures (<140 °C), moderate humidification, and higher temperatures (>200 °C).[55] Ion-pair coordinated membranes could allow for operation at a much wider temperature range than PA-PBI. Quaternary ammonium-biphosphate (QAPOH) membranes combined with phosphonated ionomers have shown high peak power outputs from 80–240 °C, and excellent durability as low as 40 °C.[113,114] Additionally, the use of an intrinsically microporous Tröger's base-derived polymer membrane has been shown to allow operation between −20 °C and 200 °C, whilst displaying exceptional performance retention even after start-up/shutdown cycling at 15 °C and −20 °C.[115]

2.1.3 Catalyst layer. One of the motivators for using HT-PEMFCs is the faster reaction kinetics associated with higher operating temperature, meaning that alternative catalysts to Pt may be used.[50] This is important as the balance between good performance due to higher catalyst loadings and reasonable cost is unresolved.[116] Despite this, carbon-supported Pt-based catalysts are still the most utilised in HT-PEMFCs, as in LT-PEMFCs.[25,38] As mentioned in Section 1.2.4, typical HT-PEMFC Pt loadings are around 1.0 mg cm^{-2}. This is attributed to poorer Pt utilisation, slower oxygen transport, and sluggish ORR kinetics in PA.[38,55] Pt alloy catalysts have been researched to reduce material cost and improve performance. Using Pt alloy catalysts, particularly PtCo, can improve performance, and so too can the addition of a heat-treatment step, and an acid-washing step that increases surface roughness.[117–119] However, the stability of the alloys is questionable as Ni and Co are expected to form oxides and hydroxides that dissolve from the

Open Access Article. Published on 07 March 2024. Downloaded on 1/20/2026 7:35:49 PM. This article is licensed under a Creative Commons Attribution 3.0 Unported Licence.

electrode surface.[38] The impact of Pt alloys on phosphate adsorption is unclear and requires additional research to identify the impacts of alloying.[25]

The catalyst supports in HT-PEMFCs are usually carbon-based much like LT-PEMFCs. Operating under typical HT-PEMFC conditions poses greater challenges to the catalyst layer due to higher temperatures increasing Pt particle growth rate and carbon corrosion.[120,121] Studies using graphene and carbon-walled nanotubes in the catalyst support have shown improved stability and power density; however, the electrochemically active surface area was higher for the conventional carbon supports.[120,122,123]

Both the catalyst and support materials in HT-PEMFCs are similar to LT-PEMFCs. However, the binder materials that join these components together can be quite different. LT-PEMFCs typically use a similar PFSA ionomer to the electrolyte which requires hydration for proton conduction in the catalyst layer, PTFE may also be added to improve water management.[124] PTFE is the most common binder material in HT-PEMFCs due to its hydrophobicity and thermal stability.[55] It is an insulating material and therefore requires a proton-conducting material. Ionic conductivity is usually enabled by the presence of PA which originates from the membrane during MEA preparation or cell assembly, or through direct deposition onto the catalyst layer.[116] Optimisation of the PA in the catalyst layer is required as too much PA leads to electrode flooding which impedes oxygen transport to catalyst sites, and non-uniform distribution reduces catalyst utilisation.[125] The catalyst microstructure should be designed to minimise crack width as this is a pathway for PA to penetrate the GDL, and have a sufficiently porous structure to allow the PA to activate the catalyst layer during activation.[126,127] PTFE optimisation is also important as it affects acid uptake and too much will flood the catalyst layers and reduce membrane conductivity.[128] The binder can also obstruct reaction pathways and decrease performance.[55] A recent study using density functional theory and molecular dynamics simulations determined that an overall binder content of 25 wt% made of equal ratios of Nafion and PTFE yielded the best Pt poisoning protection.[129] PA-PBI has also been used as the binder material. Using too much PA-PBI reduces the electrochemically active surface area (ECSA) due to increased blockages of the electron pathway, too little and there is an insufficient ionic conduction and potentially poor binding.[130,131] Phosphonated polymers show promise as ionomeric binders. They have the benefits of greatly reduced acid loss in the presence of water, and the low concentration of phosphonic acid mitigates the impact of phosphate poisoning and PA flooding of the electrode.[113] Protonation of the phosphonated ionomer has been shown to provide excellent performance and durability compared to non-protonated ionomers and state-of-the-art LT-PEMFCs.[114] However, improvements are still required under high voltage conditions, dynamic drive cycles, and partial humidification, along with the practicality of scaling up to a full-size stack (*e.g.*, non-uniform reactant supply and membrane-electrode contact).[114]

2.1.4 Bipolar plates and gaskets. Bipolar plates require high electrical conductivity to minimise ohmic losses, must be able to withstand the high compaction pressure during stack assembly, have stability at high temperatures, and possess very low gas permeability.[132,133] PA can also be redistributed into the bipolar plate causing increased ohmic resistances in the cell, so a material that does not absorb PA is preferable.[47,134] Graphite plates have traditionally been used due to their chemical stability and high electronic conductivity.[50] Composite bipolar plates have been suggested as replacements for pure graphite bipolar plates due to their higher specific strength and stiffness.[132] Carbon composite bipolar plates have exhibited superior electrical and thermo-mechanical properties or at least achieved United States Department of Energy (U.S. DoE) targets.[135–137] Metal bipolar plates are also considered an alternative to pure graphite plates as they typically possess excellent electrical and thermal conductivities, and can be machined to very small thicknesses.[138] Metal foams can also improve mass transport properties and reduce resistance compared to graphite.[139] However, the chemical stability of metallic plates are poorer compared to graphite, this leads to much higher degradation rates and the formation of ferric oxide and iron phosphate on the surface, although surface treatment can significantly reduce the degradation rates.[134,140–143] Due to these issues, graphite-based bipolar plates are currently preferred.[138]

Gaskets must seal the cell, compensate for dimensional changes, be electrically insulating, and provide compression over long periods of time, and they must do this at temperatures up to 200 °C in the presence of PA.[47,138] Fluoroelastomers (FKM), ethylene propylene diene monomer (EPDM), silicon, and PTFE are all commonly employed HT-PEMFC gasket materials.[52,144]

2.2 Operating principles

2.2.1 Basics. The individual components are assembled into an MEA and then into a full cell, the assembly process is discussed in more detail in Section 2.2.3. The basics of componentry and operation are shown in Fig. 1. The electrochemical reaction of HT-PEMFCs is the same as LT-PEMFCs except that the product water is in the gaseous state:

$$2H_2\,(g) + O_2\,(g) \rightarrow 2H_2O\,(g) \quad (1)$$

Due to operating at higher temperatures, the magnitude of the Gibbs free energy is lower than that under LT-PEMFC conditions. This leads to a lower reversible voltage: 1.18 V at 360 K (86.85 °C) and 1.15 V at 440 K (166.85 °C). The voltage decrease is minimal due to the smaller entropy change of forming a gas compared to a liquid.

Operating temperatures typically range from 120–200 °C depending on membrane and proton conduction method (hydrous or anhydrous). HT-PEMFCs relying on water for conduction generally operate up to 120 °C, where PA-based conduction mostly operates in the range of 140–180 °C. The optimum temperature balances a trade-off between cell performance and degradation rate. Operating under humified conditions will also depend on the proton conduction method.

 This journal is © The Royal Society of Chemistry 2024

Open Access Article. Published on 07 March 2024. Downloaded on 1/20/2026 7:35:49 PM.
This article is licensed under a Creative Commons Attribution 3.0 Unported Licence.

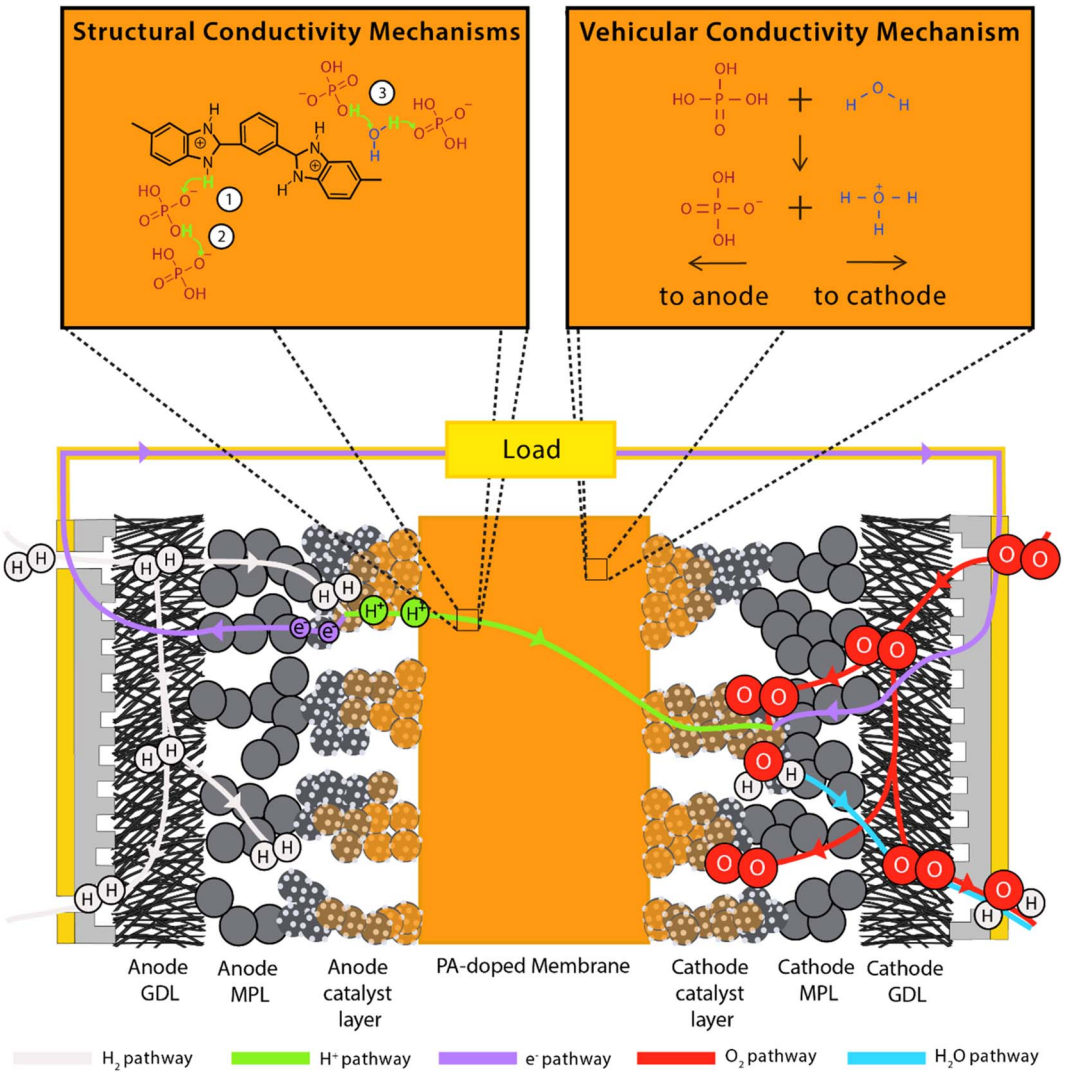

Fig. 1 Schematic of HT-PEMFC operation including structural proton conduction and vehicular conductivity mechanisms. Relative component sizes are not to scale.

Despite typically operating without external humidification, PA-based HT-PEMFCs can achieve conductivity improvements when humidified compared to non-humidified operation due to an increased contribution from the vehicular conduction mechanism (as discussed in detail in the following section) resulting from the higher water content.[92,145] However, PA loss increases with higher water content.[146,147]

2.2.2 Proton conduction. Some HT-PEMFCs require hydrous conditions for proton conduction and thus share the mechanisms with LT-PEMFCs. However, most HT-PEMFC technology uses PA as the proton conductor, often with a PBI polymer. The PBI chain has two basic nitrogen atoms per repeating unit and can trap a maximum of two PA molecules, any additional molecules are referred to as "free acid".[38,67] The proton conduction mechanisms are complex and depend on the doping level and water content.[67,92] There are several mechanisms suggested for proton conduction in PA-PBI fuel cells:[148]

(1) Hopping from the N–H sites to PA anions ($H_2PO_4^-$), most relevant for low doping scenarios *i.e.*, no free acid;

(2) Hopping along PA anions. This occurs in the presence of free acid and leads to conductivity several orders of magnitude higher than (1);

(3) Hopping *via* water molecules. This mechanism is concurrent with (2);

(4) Direct hopping along nitrogen sites of the PBI chains (only relevant for non-doped PBI).

Mechanisms 1, 2, and 3 are illustrated accordingly in Fig. 1. Proton diffusion involving benzimidazole nitrogen sites can be neglected due to its proton exchange process being nine orders of magnitude slower than proton exchange between phosphate species.[93] The high proton conductivity of PA is due to the high degree of hydrogen bond network frustration (a severe imbalance of proton donors to acceptors). This explains the significant contribution of rapid structural diffusion (hopping) to proton conductivity (~97% in neat PA).[92] As temperature increases and water content decreases, PA undergoes condensation reactions and forms higher molecular weight and slower diffusing phosphate species, whilst also reducing the hydrogen bond network

Open Access Article. Published on 07 March 2024. Downloaded on 1/20/2026 7:35:49 PM. This article is licensed under a Creative Commons Attribution 3.0 Unported Licence.

frustration, resulting in a slight decrease in conductivity. Increasing water content leads to an increase in conductivity contribution *via* the vehicular mechanism through the transport of H_3O^+ and $H_2PO_4^-$.[92] This mechanism is shown in Fig. 1. Fig. 2 shows the peak contribution from structural diffusion in neat PA and an increase in vehicular transport as water content increases. Despite the improvement in total conductivity, operation at high temperatures and water content leads to increased PA loss.[149] Although adding PBI to PA decreases the proton conductivity by decreasing the hydrogen bond network frustration, it also reduces the hygroscopicity (water uptake) of PA, which reduces electroosmotic drag and may explain why PA-PBI membranes outperform other PA-based electrolytes.[93]

2.2.3 Assembly and activation. The assembly process of HT-PEMFCs is similar to LT-PEMFCs whereby the membrane is sandwiched between the catalyst-coated substrates (CCS) *i.e.*, gas diffusion electrodes, and hot-pressed. Catalyst coated membranes (CCM) may also be used, in which case the CCM is sandwiched between gas diffusion layers and hot-pressed or directly assembled into the cell without pressing.[22,67] Unlike LT-PEMFCs, HT-PEMFCs are generally not hot-pressed close to the glass transition temperature of the PBI membrane (425–436 °C).[150] Some studies that use hot-pressing to assemble the MEA do not give the hot-pressing temperature.[151–153] Where given, typical temperatures, pressures and durations are 130–200 °C, ~2–10 N mm^{-2}, and 0.5–10 min, respectively.[53,130,154–160] Assembly of HT-PEMFCs can be achieved without hot-pressing as the triple-phase boundary is formed by the liquid PA network within the catalyst layers which can be distributed when the cell is assembled, heated and bolt torque applied.[125,128,161] However, this may cause a greater level of delamination.[162] The effect of hot-pressing conditions has been studied for LT-PEMFCs.[163,164] However, there are few studies in the literature for HT-PEMFCs, and this is an area that requires further study and optimisation. Hot-pressing in HT-PEMFCs is often an important step and is one of the PA loss mechanisms whereby PA penetrates into the diffusion layers and is lost.[22,165]

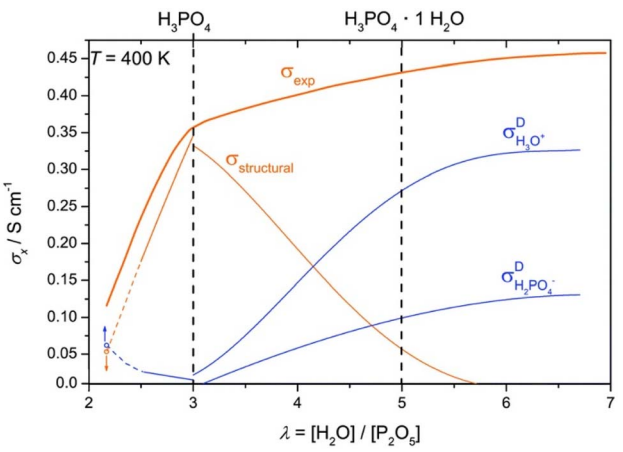

Fig. 2 Total ionic conductivity of PA as a function of water content and the contributions from structural diffusion and ionic transport of H_3O^+ and $H_2PO_4^-$. Adapted from ref. 92 with permission from the Royal Society of Chemistry.

The activation process occurs after assembly but prior to testing or general operation. The aim of this process is to enable the maximum fuel cell performance to be achieved *via* a "break-in" period. The activation of LT-PEMFCs is mainly focused on the hydration of the PFSA membrane.[166] During HT-PEMFC activation, PA is redistributed from the electrolyte driven by current, capillary force, and hydrophilic and hydrophobic properties of the catalyst layer.[155] The optimal interface is achieved when the carbon support, catalyst sites and membrane are connected by a thin film of PA. This optimum is disrupted by the presence of water.[167] Sufficient penetration of PA into the catalyst layers is required for catalyst utilisation and limitation of the charge transfer resistance.[168] The activation procedure used can greatly influence the uniformity of current distribution and required procedure duration, not just the steady-state voltage.[155] The procedure is also required to provide reproducible performance over time.[169] Galvanostatic (constant current) activation is reported to yield the best results compared to current cycling, potential cycling, temperature cycling, and increased back pressure activation.[155,170,171] Uneven distribution of PA within the MEA can initially lead to severe heterogeneous current density distributions which can cause local hot spots, resulting in local catalyst and membrane degradation.[155] Typically, galvanostatic activation is performed at low current densities (0.2 A cm^{-2}) and the duration ranges from 24 to 100 hours.[155,169,172–174] This is in contrast to LT-PEMFCs where the activation procedure duration required is typically 6–20 hours, and often utilises potential cycling.[175–178]

2.2.4 Start-up. HT-PEMFCs operate above the boiling point of water but may be below this value before start-up. LT-PEMFCs have shorter start-up times than HT-PEMFCs due to the lower operating temperature. Start-up processes for HT-PEMFCs using the heat release from the electrochemical reaction to aid in the warming process are generally faster than those that do not use reaction heat; any reaction heating is typically accompanied by gas or coolant heating.[179–182] The issue with using reactant heating for HT-PEMFCs is the formation of liquid water below the boiling point. As is discussed in more detail in Section 2.2.5, the presence of water influences PA loss. Many of the studies on the start-up process for HT-PEMFCs focus almost entirely on the start-up time and energy efficiency and not its effect on performance degradation. Some studies begin reaction heating below 100 °C to minimise start-up time,[180,181] while others only use reaction heating above 100 °C, likely to reduce acid loss.[179,182–184] Further research into the performance degradation due to the heating of the stack from cold is required. Even less research has been conducted into the performance of HT-PEMFCs operating at sub-zero conditions. However, good performance has been achieved by HT-PEMFCs operating at sub-zero conditions due to PA being the main proton conduction mechanism, and therefore are not so sensitive to water in solid form as LT-PEMFCs.[115,185]

2.2.5 Degradation mechanisms specific to HT-PEMFCs. HT-PEMFCs share many degradation processes with LT-PEMFCs, but often at a higher rate due to the increased temperature.[186–188] These include carbon corrosion,[121,189,190] Pt dissolution, detachment, Ostwald ripening, sintering, and agglomeration,[156,189,191,192]

 This journal is © The Royal Society of Chemistry 2024

Open Access Article. Published on 07 March 2024. Downloaded on 1/20/2026 7:35:49 PM. This article is licensed under a Creative Commons Attribution 3.0 Unported Licence.

catalyst layer damage caused by H_2–air interfaces during start-up,[193,194] chemical attacks on the membrane,[195,196] and membrane thinning.[197,198] HT-PEMFCs are also susceptible to carbon monoxide (CO) poisoning as they use a Pt catalyst.[199] However, their tolerance for CO is much higher: HT-PEMFCs can withstand CO contents of 3–5% (30 000–50 000 ppm),[34,200] whereas LT-PEMFCs show significant performance decrease around 0.005% (50 ppm).[201,202] Reformate after the water–gas-shift reaction has a typical CO content of 2%.[203] Therefore, HT-PEMFCs have the potential to use reformate fuel directly, whereas LT-PEMFCs cannot without additional cleaning, which adds cost and complexity. This is a major advantage over LT-PEMFCs in terms of commercialisation, as methods using steam-methane reforming are currently the cheapest way to produce hydrogen.[204] It is even reported that CO can help to mitigate carbon corrosion and ECSA loss during load cycling.[193] Engl *et al.* found CO blocked catalyst sites and inhibited the electrochemical reactions, easing degradation *via* the reverse current mechanism.[205]

Introduction of PA to the system leads to degradation mechanisms that are not present in LT-PEMFCs. One of these mechanisms is acid migration. The number of PA molecules per imidazole group (acid doping level) can be as high as 70.[206] This results in significant quantities of free acid with high mobility. As discussed in Section 2.2.2, there are multiple proton conductions mechanisms. One is the transport of $H_2PO_4^-$ from cathode to anode. Anion migration accounts for approximately 2–4% of the total charge transfer under typical HT-PEMFC conditions.[207] This migration of $H_2PO_4^-$ increases with current density and doping level, and can lead to sufficient acid pressure at the anode to penetrate the catalyst layer and porous structures, potentially resulting in electrode flooding and acid loss.[126,157,208,209] The leaching out of the membrane will cause ohmic resistance to increase, electrode flooding may impede mass transport of reactants, and ultimately reduce cell lifetime.[157,208,209] The increase of $H_2PO_4^-$ at the anode leads to a concentration gradient which causes back diffusion towards the cathode, and under steady-state conditions an equilibrium is reached.[207] The leaching acid typically travels through overlapping catalyst layer and MPL cracks.[157] Designing catalyst layers and MPLs that have smaller cracks, and reducing crack connectivity between the catalyst layer and MPL can significantly reduce acid loss *via* this mechanism.[69,126]

Despite the $H_2PO_4^-$ migration mechanism, the majority of PA leaching during operation occurs at the cathode. Phosphoric acid is highly hygroscopic and hydrophilic, and the generation of water at the cathode causes free PA to be washed out.[147,149,210] A recent study suggests that it is not the PA–water interaction that leads to leaching, but rather the inability of the polymer to hold both water and PA above a certain level.[211] As the membrane is exposed to water, the PA cluster takes up water until it is limited by the polymer chains, the addition of water increases the cluster interaction energy and PA molecules are exchanged for water molecules which results in acid leaching. And as temperature increases, the water vapour pressure exceeds the hydrogen bonding of water to the PA cluster, and water molecules begin to escape; this explains why PA loss has been reported to be negligible at higher temperatures (160–180 °C).[186,187,211] This newly proposed PA loss mechanism due to the exposure to water and high temperatures is shown in Fig. 3.

Another loss mechanism is PA evaporation. Despite the low vapour pressures of PA below 300 °C, acid can still be lost through evaporation, and this loss increases with temperature and reactant gas flow rate.[212]

Acid can also be lost during MEA assembly. If the hot-pressing conditions are not optimised (particularly over-compression) the diffusion layers can be soaked with acid.[22,165] Once this acid enters the electrodes, it will be lost during conditioning or normal operation as the gases remove it from the porous diffusion layers. Therefore, it is important not to over-compress during assembly as this is another mechanism of acid loss. In summary, the acid loss mechanisms are:

(1) Phosphate anion migration from cathode to anode resulting in sufficient acid pressure to cause leaching at the anode;

(2) Significant water content causing free PA to be effectively washed out at the cathode;

(3) Evaporation of PA at high temperatures;

(4) PA penetration into the diffusion layers during hot-pressing.

While not a significant degradation mechanism, it is worth noting that as temperature increases and PA water content decreases, PA condensation reactions occur. The condensation products are polyphosphoric acids of higher molecular weight (*e.g.*, $H_4P_2O_7$, $H_5P_3O_{10}$).[92] This results in slower phosphate diffusion and a reduction in hydrogen bond network frustration, leading to a slight decrease in ionic conductivity.[92,93] Lower molecular weight species (H_3PO_4) are regained by increasing the water content and subsequent hydrolysis reactions. A benefit of PBI membranes is the acid–base interaction reduces the concentration of condensation products while increasing the *ortho*-phosphate species.[93]

HT-PEMFCs also suffer from phosphate adsorption onto the Pt catalyst which block reaction sites and inhibit ORR and HOR.[152,213,214] Adsorption of the phosphate species at the cathode is dependent on temperature and potential. The potential dependence is illustrated in Fig. 4. Hydrogen and oxygen adsorption are dominant below 300 mV and above 800 mV, respectively. Intermediate voltages (300–800 mV) are dominated by phosphate adsorption, and increasing the temperature decreases this window.[152] Phosphate adsorption also occurs at the anode but is not expected to cause serious poisoning and may even assist in stabilising hydrogen adsorption. CO in the anode gas feed can increase phosphate adsorption, whilst the presence of water decreases coverage.[214]

HT-PEMFCs that use phosphonated polymers may also suffer from phosphonic acid anhydride formation which decreases proton conductivity; although, polymers can be designed with hydroxyl groups with low reactivity in phosphonic acid to avoid this formation.[113,114]

2.3 State-of-the-art HT-PEMFC performance

Table 1 gives an overview of HT-PEMFC and LT-PEMFC performance. HT-PEMFCs are clearly able to achieve high

Open Access Article. Published on 07 March 2024. Downloaded on 1/20/2026 7:35:49 PM.
This article is licensed under a Creative Commons Attribution 3.0 Unported Licence.

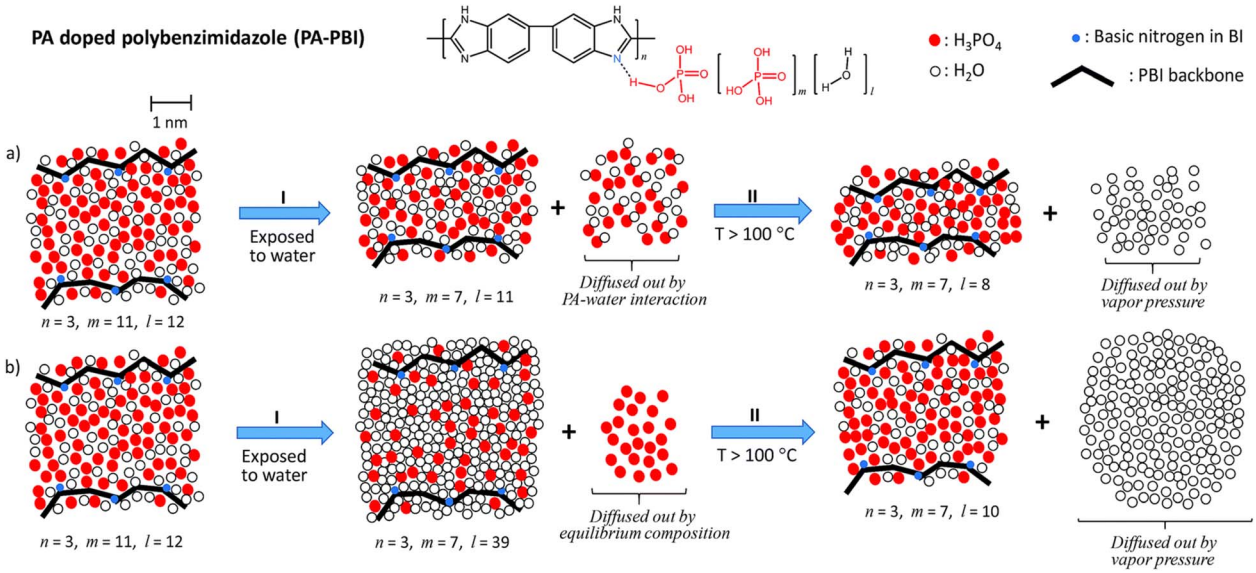

Fig. 3 Schematic of (a) previous PA loss mechanism and (b) newly proposed PA loss mechanism when exposed to water and high temperatures. Reproduced from ref. 211 with permission from the Royal Society of Chemistry.

power densities and proton conductivities. PA-PBI based HT-PEMFCs show good performance at temperatures of ≈160 °C. Operation at temperatures much higher than this can cause issues with PA evaporation.[114,212] A recent study showed good performance and PA retention from −20 to 200 °C using ultramicroporous PA-doped Tröger's base polymers (Fig. 5).[115] The improved retention was attributed to the acid–base interactions and syphoning effect of microporosity. Recent work has also shown the promise of ion-pair membranes, specifically QAPOH which have demonstrated excellent PA retention at lower temperature operation.[112–114,215] The use of ion-pair and phosphonated polymer ionomeric binders have also been shown to improve HT-PEMFC performance by increasing acid retention and limiting anhydride formation.[113,114,215] Fig. 6 shows a comparison of polarisation curves for protonated and non-protonated QAPOH-PA, and PBI-PA HT-PEMFCs to a LT-PEMFC and anion exchange membrane (AEM) FC. Use of QAPOH membranes and protonation of the ionomer showed a significant performance improvement over the PBI HT-PEMFC. The exponential voltage decay at high current densities is visible for the LT-PEM and AEM fuel cells, typically due to electrode flooding impeding reactant transport.[216] Operating at HT-PEMFC temperatures results in a relatively linear *i*–*V* relationship at high current densities, due to the absence of liquid water. The HT-PEMFC using protonated phosphonic acid ionomers can achieve current and power densities comparable to the LT-PEMFC. Although, low current density performance is poorer for HT-PEMFCs due to sluggish ORR rates in concentrated PA.[53,213]

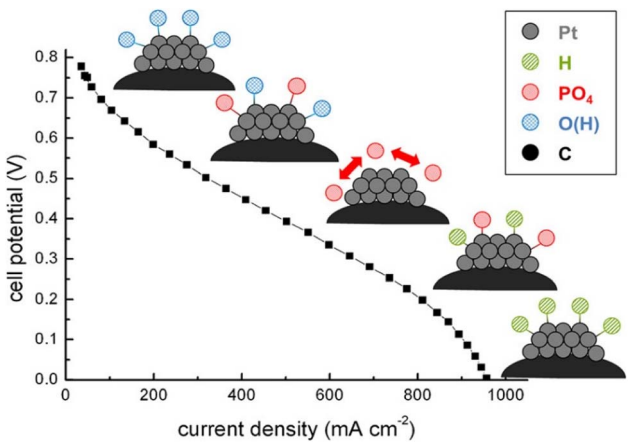

Fig. 4 Dominating species adsorption on Pt catalyst across the polarisation curve. Reprinted with permission from ref. 152, Copyright (2013) American Chemical Society.

While high power densities are achieved with HT-PEMFCs, many of the studies use pure oxygen instead of air to achieve this performance. In many applications such as vehicles, air would be supplied instead, and the peak power density will be significantly reduced. The U.S. DoE has set a rated power target of 1800 mW cm^{-2} to be achieved with air supplied to the cathode by 2025.[217] The data suggests commercial LT-PEMFCs are closest to achieving this target, although much of the information about commercial cells and stacks is proprietary. HT-PEMFCs still require performance improvement to achieve power densities >1000 mW cm^{-2} under H_2/air operation. In addition, the total Pt group metal (PGM) content is recommended to be ≤0.10 mg_{PGM} cm^{-2}.[217] Table 1 and Fig. 6 show that significantly higher Pt loadings are used for HT-PEMFCs to achieve performance similar to LT-PEMFCs. Generally, Pt content needs to be reduced by a factor of 10 to meet the recommended target.

Power density is not the only important performance criterion. Durability is critical to real-world use of fuel cell technology. LT-PEMFCs have shown their durability in applications,

 This journal is © The Royal Society of Chemistry 2024

Open Access Article. Published on 07 March 2024. Downloaded on 1/20/2026 7:35:49 PM.
This article is licensed under a Creative Commons Attribution 3.0 Unported Licence.

Table 1 State-of-the-art HT-PEMFC performance *vs.* LT-PEMFC. *T*, RH, and *P* refer to temperature, relative humidity, and pressure, respectively

T (°C)	RH an./ca. (%)	*P* an./ca. (kPa_{abs})	Flow rate an./ca. flow rate (mL min^{-1}), (cathode gas)	Membrane/thickness (μm)	Pt loading an./ca. (mg cm^{-2})	Peak power density (mW cm^{-2})	Proton conductivity@temperature (mS cm^{-1}@°C)	Ref.
LT-PEMFCs								
60	100/100	101/101	35/70 (O_2)	Phosphosilicate sol-SPEEK/67	0.48/0.48	450	138@70	220
70	—/—	101/101	60/60 (O_2)	SiO_2 SPEEK-Nafion/72	0.40/0.40	589	18@80	221
75	100/100	—/—	100/100 (O_2)	$TiSiO_4$-Nafion/70	0.40/0.40	803	249@70	222
80	50/50	101/101	300/300 (O_2)	Phosphotungstic acid-graphene oxide-SPAEK/45	0.40/0.40	782	261@80	223
80	100/100	—/—	1.4/2.5 stoichiometry (air)	Layered double hydroxide-SPEEK/—	0.40/0.40	560	230@80	224
80	100/100	148/148	500/500 (air)	GORE/15	0.10/0.40	1300[a]	—	114
80	30/50	250/230	1.3/1.5 stoichiometry (air)	—/—	—/—	1344	—	225
94	65/65	250/250	1.5/2.0 stoichiometry (air)	Nafion/14	—/0.20	1300[a]	—	226
94	65/65	250/250	1.5/2.0 stoichiometry (air)	Nafion/14	—/0.05	960[a]	—	226
100	100/100	148/148	500/500 (air)	Nafion/25	0.10/0.10	900[a]	—	114
HT-PEMFCs								
80	0/0	170/170	500/500 (O_2)	QAPOH/35	0.50/0.70	530	4[a]@80	114
120	0/0	101/101	100/200 (air)	Pyridine-PBI/28	0.32/0.32	779	37@120	227
130	100/100	300/300	1.5/2.0 stoichiometry (O_2)	Nafion/51	0.30/0.30	620	—	191
130	100/100	300/300	1.5/2.0 stoichiometry (O_2)	Aquivion/30	0.30/0.30	870	—	191
140	—/—	—/—	300/500 (O_2)	Phosphonated polystyrene/—	0.25/0.375	184	5.8@140	228
160	—/—	—/—	—/— (O_2)	PBI/—	—/—	638	89@160	229
160	0/0	—/—	80/160 (O_2)	PBI/30–50	—/—	713	150@160	230
160	0/0	—/—	82/296 (air)	PBI/106	1.00/1.00	447	214@160	231
160	0/0	—/—	—/— (air)	QA-PBI/—	0.50/1.50	412	75[a]@160	232
160	0/0	101/101	200/200 (O_2)	Dimethylbiphenyl Tröger's base polymer/160	0.50/0.50	815	140[a]@160	115
160	0/0	147/147	500/500 (O_2)	PBI/50	0.50/0.60	500[a]	100[a]@160	113
160	0/0	147/147	500/500 (O_2)	QAPOH/40	0.50/0.60	1130	110[a]@160	113
200	0/0	147/147	500/500 (O_2)	QAPOH/40	0.50/0.60	1503	110[a]@200	113
200	0/0	170/170	500/500 (O_2)	QAPOH/35	0.50/0.70	2010	10[a]@160	114
200	0/0	101/101	200/200 (O_2)	Dimethylbiphenyl Tröger's base polymer/160	0.50/0.50	630[a]	120[a]@200	115
240	0/0	147/147	500/500 (O_2)	QAPOH/40	0.50/0.60	1740	110[a]@240	113
240	0/0	285/285	200/500 (air)	SnP_2O_7-Nafion composite/80	0.60[b]	410	80[a]@160	215

[a] Value estimated from plot. [b] Individual electrode loading not specified.

Open Access Article. Published on 07 March 2024. Downloaded on 1/20/2026 7:35:49 PM.
This article is licensed under a Creative Commons Attribution 3.0 Unported Licence.

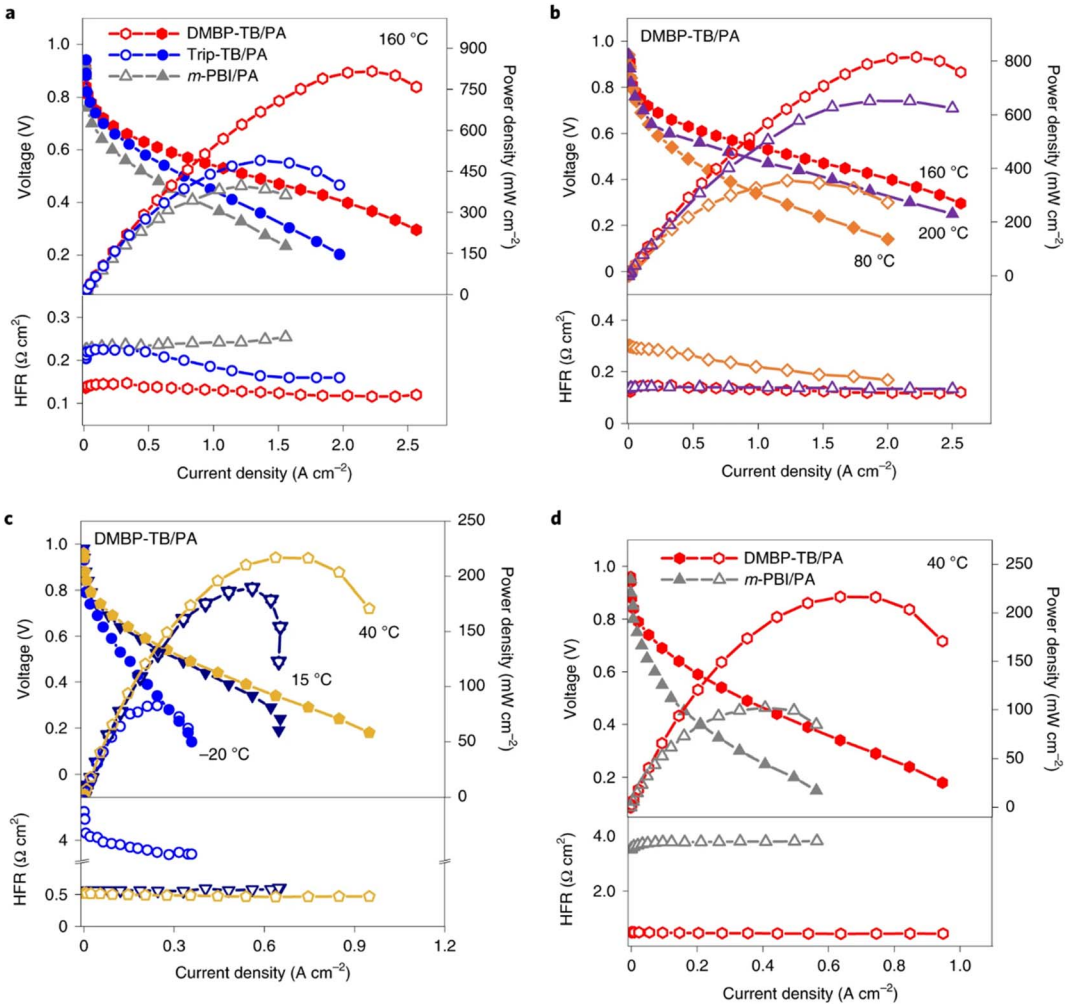

Fig. 5 Polarisation curves, power density and high-frequency resistance of HT-PEMFCs based on TB and m-PBI membranes without back-pressure or humidification: (a) TB/PA and m-PBI MEAs at 160 °C, (b) PA/dimethylbiphenyl (DMBP)-TB performance 80–200 °C, (c) DMBP-TB MEA performance −20–40 °C, and (d) PA/DMBP-TB and PA/m-PBI MEA performance 40 °C.[115]

and have met or exceeded durability targets in some cases, but still require improvement.[218] The U.S. DoE 2025 targets require dynamic durability exceeding 8000 hours based on its own drive cycle protocol. Tables 2 and 3 show the steady-state and dynamic degradation rates of LT and HT-PEMFCs across a range of tests.

Differences in durability testing protocols across studies make direct performance comparisons difficult, but overall

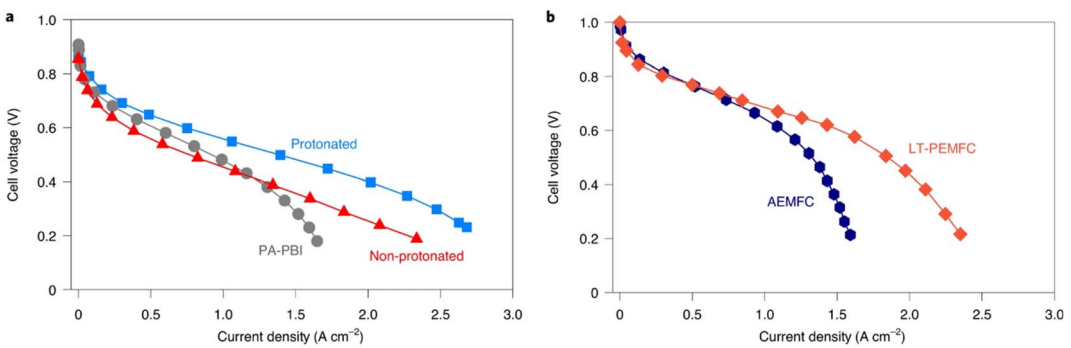

Fig. 6 H_2/air polarisation curves for (a) protonated and non-protonated QAPOH, and PBI HT-PEMFCs at 160 °C and 148 kPa backpressure, and (b) Nafion LT-PEMFC and AEMFC at 80 °C and 148 kPa backpressure, with anode/cathode Pt loadings of 0.5/0.7, 0.5/0.6, 1.0/0.75, 0.1/0.4, and 0.5/0.6 mg_{Pt} cm^{-2}, respectively.[114]

 This journal is © The Royal Society of Chemistry 2024

Open Access Article. Published on 07 March 2024. Downloaded on 1/20/2026 7:35:49 PM.
This article is licensed under a Creative Commons Attribution 3.0 Unported Licence.

Table 2 Steady-state durability tests of HT-PEMFCs *vs.* LT-PEMFCs. *T*, RH, and *P* refer to temperature, relative humidity, and pressure, respectively

T (°C)	RH an./ca. (%)	*P* an./ca. (kPa_{abs})	Membrane/thickness (μm)	Pt loading an./ca. (mg cm^{-2})	Voltage (V)	Current density (A cm^{-2})	Test duration (h)	Degradation rate (μV h^{-1})	Ref.
LT-PEMFC									
55	20/20	101/101	Gore/—	—/—	0.58–0.49[a,b]	0.50	1000	90[b]	233
70	100/100	101/101	GoreSelect/35	0.45/0.60	0.65–0.54	0.80	26 300	4–6	234
75	100/100	480/480	Dow/—	4.00/4.00	0.80–0.79[a]	0.86	11 000	1.3	235
75	100/100	480/480	Dow/—	4.00/4.00	0.85–0.83[a]	0.54	11 000	1.4	235
75	81/81	101/101	Nafion/51	0.50/0.50	0.67[c]–0.61[a]	0.30	2700	22	236
80	100/100	150/150	GoreSelect/25	0.40/0.40	0.78–0.73[a]	0.20	2000	25	237
80	100/100	150/150	GoreSelect/25	0.40/0.40	0.96–0.93[a]	0.00	2000	20	237
HT-PEMFC									
40	0/0	101/101	Dimethylbiphenyl Tröger's base polymer/160	0.50/0.50	0.48–0.41[a]	0.30	150	467	115
80	0/0	148/148	QAPOH/40	0.50/0.60	0.50	0.20	200	0	114
140	0/0	—/—	PBI/50–75	1.00/0.75	0.62–0.59[a]	0.25	1600	13[b]	238
150	0/0	101/101	PBI/—	1.70 (total)	0.42–0.38[a]	1.00	1100	41	147
150	—/—	101/101	PBI/—	0.15/0.35	0.43[a,b]	0.20	1100	22[b]	239
150	0/0	101/101	PBI/—	0.90/1.70	0.70–0.55[a]	0.20	4000	16–53[b]	240
160	0/0	148/148	QAPOH/40	0.50/0.60	0.60[c]–0.59	0.60	2500	3.3[c]	114
160	0/0	147/147	QAPOH/40	0.50/0.60	0.55	0.60	550	0.35	113
160	0/0	101/101	PBI/40	0.30–0.36/0.9	0.62–0.55[a]	0.20	13 000	4.6[c]	241
160	0/0	101/101	PBI/40	0.30–0.36/0.9	0.59–0.57	0.20	13 000	1.4[c]	241
160	0/0	—/—	PBI/45	1.00 (total)	0.67	0.20	187	36	110
160	0/0	—/—	PBI/50–75	1.00/0.75	0.53–0.39	0.40	659	180[b]	242
167	1.5/0	—/—	PBI/—	—/—	0.53–0.49[a]	0.50	810	49[a,b]	243
180	0/0	101/101	PBI/90	0.25/0.78	0.65–0.62	0.20	10 400	2.3	100
200	0/0	—/—	PBI/70	0.10/1.60	0.68–0.53	0.20	2700	27[c]	244

[a] Value estimated from plot. [b] Average of stack. [c] Value after initial performance increase.

Open Access Article. Published on 07 March 2024. Downloaded on 1/20/2026 7:35:49 PM.
This article is licensed under a Creative Commons Attribution 3.0 Unported Licence.

Table 3 Dynamic durability tests of HT-PEMFCs *vs.* LT-PEMFCs. *T*, RH, and *P* refer to temperature, relative humidity, and pressure, respectively

T (°C)	RH an./ca. (%)	*P* an./ca. (kPa_{abs})	Membrane/thickness (μm)	Pt loading an./ca. (mg cm^{-2})	Test profile	Test duration (h or cycles)	Degradation rate (μV h^{-1} or μV per cycle)	Ref.
LT-PEMFC								
40	100/100	—/—	—/20	0.40 (total)	Start-up/shutdown	1200 cycles	125@0.40 A cm^{-2}	245
65	100/100	—/—	—/20	0.40 (total)	Start-up/shutdown	1200 cycles	233@0.40 A cm^{-2}	245
80	100/100	—/—	—/20	0.40 (total)	Start-up/shutdown	1200 cycles	317@0.40 A cm^{-2}	245
55	50/50	101/101	Nafion/23	—/—	Dynamic load cycle (NEDC)	300 h	40@0.00 A cm^{-2}[a,b] 150@1.00 A cm^{-2}[a,b]	246
75	50/50	101/101	Nafion/23	—/—	Dynamic load cycle (NEDC)	300 h	210@0.00 A cm^{-2}[a,b] 560@1.00 A cm^{-2}[a,b]	246
65	95/95	—/—	Nafion/—	0.10/0.40	Start-up/shutdown	1000 cycles	70@0.64 A cm^{-2}[a] 80@1.00 A cm^{-2}[a]	247
65	50/80	101/101	Nafion/25	0.10/0.30	Current step cycling	2000 cycles	19@0.60 A cm^{-2}[b] 130@1.00 A cm^{-2}[b]	248
76	50/50	100/80[c]	GORE-Nafion/18	0.40 (total)	Dynamic load cycle (NEDC)	1000 h	41@1.00 A cm^{-2}[a,b]	249
80	90/90	101/101	Nafion/28	0.09/0.61	Start-up only Shutdown only	750 cycles 930 cycles	27@0.67 A cm^{-2} 32@0.67 A cm^{-2}	250
80	90/90	101/101	Nafion/28	0.09/0.12	Start-up only Shutdown only	360 cycles 660 cycles	472@0.67 A cm^{-2} 273@0.67 A cm^{-2}	250
80	100/100	101/101	—/18	0.018/0.10	Potential cycling	30 000 cycles	4@1.50 A cm^{-2}	251
HT-PEMFC								
160	—/—	101/101	PBI/50–75	1.00/0.75	High current cycling	51 h	400@0.60 A cm^{-2} 500@1.00 A cm^{-2}	189
80–160	1–16/1–16	68.9/68.9[c]	QAPOH/80	0.60/0.60	Thermal cycling	550 cycles[a]	390@0.15 A cm^{-2}	112
80–160	1–16/1–16	68.9/68.9[c]	PBI/50	1.00/0.75	Thermal cycling	70 cycles	11 143@0.15 A cm^{-2} (failure)	112
160	0/1.4	—/—	PBI/40	1.50/1.50	Potential cycling	30 000 cycles	9@0.30 A cm^{-2}[a]	156
25–180	—/—	101/101	PBI/—	1.00/0.75	Start-up/shutdown	4000 h	19@0.20 A cm^{-2}	252
160	—/—	—/—	PBI/—	1.00/1.50	Start-up/shutdown	600 h	30@0.20 A cm^{-2}	194
160	—/—	—/—	PBI/—	1.00/1.50	High current cycling	600 h	84@0.20 A cm^{-2}	194
160	—/—	—/—	PBI/—	1.00/1.50	Low current cycling	600 h	115@0.20 A cm^{-2}	194
160	0/0	100/100	PBI/50–75	1.00/0.75	High current cycling	70 h	486@1.00 A cm^{-2}	146
160	0/0	100/100	PBI/50–75	1.0/0.75	Low current cycling	70 h	363@0.30 A cm^{-2}	146
30–160	—/—	—/—	PBI/—	—/—	Start-up/shutdown	20 cycles	4–73@0.30 A cm^{-2}	219
160	—/—	—/—	PBI[d]/—	—/—	High current cycling	1100 cycles	32–62@0.30 A cm^{-2} 48–144@0.60 A cm^{-2} 68–314@1.00 A cm^{-2}	219
80–180	0/0	—/—	PBI/50–75	1.00/0.75	Start-up/shutdown	1562 cycles	26@0.25 A cm^{-2}[b] 11@0.03 A cm^{-2}[b]	238

[a] Value estimated from plot. [b] Average of stack. [c] Backpressure. [d] Three different MEA manufacturers.

This journal is © The Royal Society of Chemistry 2024

Open Access Article. Published on 07 March 2024. Downloaded on 1/20/2026 7:35:49 PM. This article is licensed under a Creative Commons Attribution 3.0 Unported Licence.

trends can be inferred. Generally, the reported degradation rates in Tables 2 and 3 are similar for LT and HT-PEMFCs. However, LT-PEMFCs can achieve such rates at higher current densities and voltages and therefore can achieve a higher power density with a similar degradation rate to HT-PEMFCs. LT-PEMFCs are closer to achieving the 2025 durability target of 8000 hours under DoE test protocols, likely due to their maturity and greater testing and characterisation under dynamic conditions. There are far fewer studies of HT-PEMFCs using drive cycles, therefore, it is more difficult to state the current status under these test conditions. However, studies have shown cycling at high current densities typically leads to high degradation rates in HT-PEMFCs due to loss of acid from the membrane and through the diffusion layers, and catalyst layer degradation.[146,189,219] Crucially, HT-PEMFCs require significantly higher PGM loadings compared to LT-PEMFCs to achieve these degradation rates as is evident in Tables 2 and 3. Therefore, research efforts should be aimed at improving durability and reducing PGM content, with a key tool in achieving this being effective characterisation.

There are also fewer studies reporting the durability of HT-PEMFC stacks, particularly under dynamic conditions. This may be partly attributable to the increased material cost of testing stacks, as well as the testing hardware available. However, large active area cells assembled into stack hardware is more representative of commercial systems than are small area MEAs. Thus, testing and characterisation at the stack level is an important step in commercialising the technology. The degradation rates in Table 2 for stacks are typically higher than MEAs, suggesting the cell area scale up and stack design may have important effects on durability. These improvements required for HT-PEMFC performance and durability necessitate the development of advanced characterisation techniques and standardised AST protocols. These techniques must allow for comprehensive assessment and comparison across multiple scales from physico-chemical processes, up to overall electrochemical performance.

3. Electrochemical characterisation techniques

The electrochemical performance of the cell must be evaluated as it is one of the most important parameters alongside cost. Electrochemical techniques are used to evaluate the performance, degradation and durability, and are also used to validate and inform modelling efforts.

3.1 Polarisation curve

The polarisation curve is a common method of evaluating PEMFC performance. For HT-PEMFCs, the method involves initially stabilising the fuel cell at constant current, typically 0.2 A cm^{-2} to avoid high potentials which could cause carbon corrosion at lower current densities or PA loss at high current densities.[253,254] After stabilisation, the current density is incrementally increased from 0 A cm^{-2} with a constant step time *e.g.*, 30 s, and the corresponding voltage at each increment is measured, referred to as a galvanostatic sweep. Typically, once the voltage drops below a pre-set value, the current direction is reversed, and the voltage is measured again at each increment. This is particularly important for LT-PEMFCs which can exhibit significant hysteresis behaviour.[216,255] The hysteresis effect is attributed to the water dynamics in the membrane due to the water generation at the cathode, and water storage capabilities of the membrane and GDLs.[216] The influence of water on proton conduction and electrode flooding means the water dynamics affect the performance, with the backward sweep typically yielding better performance.[255] This can be attributed to a greater level of membrane hydration for the backward sweep as water has accumulated at higher current densities during the forward sweep. HT-PEMFCs have also been reported to exhibit hysteresis behaviour, an example of this is shown in Fig. 7.[256,257] However, discussion on the phenomenon in HT-PEMFCs is very limited. PA is hygroscopic, and water is known to improve the conductivity of HT-PEMFCs. Therefore, the hysteresis effect may be attributed to water dynamics as in LT-PEMFCs. In this case, it should be expected that the hysteresis effect for HT-PEMFCs is less severe than for LT-PEMFCs due to the greatly diminished influence of water on membrane conductivity characteristics. However, literature reports are inconclusive as both sweep directions have been reported to yield the best performance depending on the study.[256,257] Further research is required to confirm the cause of hysteresis and the dependence on operating conditions. The degree of hysteresis may then be useful as a diagnostic technique.[216] Due to the length of hold and measurement times, polarisation curves capture the pseudo steady-state performance, which can be useful in steady-state modelling. However, other techniques are required for analysis of dynamic performance.

3.2 Current interrupt (CI)

Current interrupt (CI) is a simple and fast technique for determining high-frequency resistance (HFR). CI involves measuring the voltage response to an abrupt step-change in

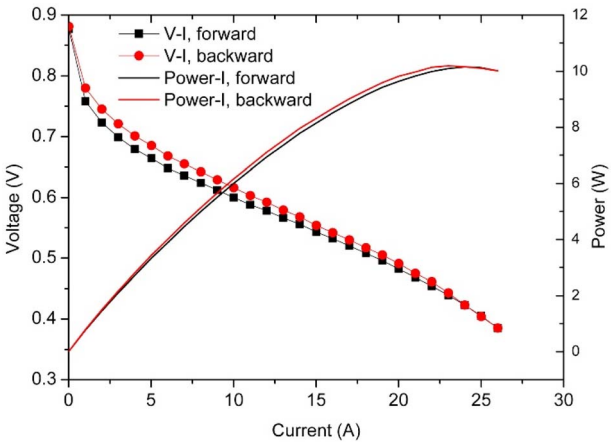

Fig. 7 Polarisation curve showing hysteresis behaviour in HT-PEMFC operating at 160 °C with dry input gases. Reprinted from ref. 256, Copyright (2015), with permission from Elsevier.

Open Access Article. Published on 07 March 2024. Downloaded on 1/20/2026 7:35:49 PM. This article is licensed under a Creative Commons Attribution 3.0 Unported Licence.

current. This measurement can be done in parallel with polarisation curve measurements, which is beneficial as it captures the resistance change as a function of current. CI is often used to estimate HFR, and this is predicated on the principle that the voltage response to ohmic resistance is nearly instantaneous, and therefore can be distinguished from other losses in the response.[258] CI has been reported to give higher resistance values than electrochemical impedance spectroscopy (EIS) due to the larger perturbation of CI causing non-zero potential distributions within the porous electrodes, yielding an additional ohmic loss contribution.[259] Also, if the measurement frequency used to determine HFR during CI is significantly lower than EIS, *e.g.*, 10^2 Hz compared to $>10^5$ kHz, this would result in non-ohmic resistance contributions being measured. Despite this, CI is often used to infer membrane resistance,[20] and has the benefit of being less complex than EIS. The CI method does not differ between LT and HT-PEMFC technology.

3.3 Electrochemical impedance spectroscopy (EIS)

EIS is another widely-used method for characterising electrochemical systems, and for the theory of the technique and application to PEMFCs in general, the reader is referred to existing review articles.[260–262] During an EIS measurement, the fuel cell is held at a constant current (or voltage if using potentiostatic mode), an AC perturbation signal which is typically 5–10% of the DC signal (or approximately 10 mV if using potentiostatic mode) is applied and the voltage (or current) response is measured.[260–262] The optimum amplitude requires a trade-off that allows sufficient signal-to-noise without violating linearity or stability requirements; the optimum amplitude may also vary with frequency. Total Harmonic Distortion (THD) has been used to identify the optimum amplitude as a function of frequency, with values ranging from 5–80% of the DC current signal.[263] Galvanostatic EIS is generally preferred for fuel cells as it is less likely to result in the cell being overloaded compared to potentiostatic mode whereby small voltage changes result in large current changes.[262] However, potentiostatic mode allows for better representation of electrode kinetics which are potential-dependent. The impedance measurement is repeated at intervals across a wide frequency range. The typical frequency range for electrochemical systems is 0.01 Hz to 10 kHz, with 10 points per decade.[260] A range of 0.1 Hz to 100 kHz has been recommended specifically for HT-PEMFCs.[264] The fuel cell should be held at the EIS measurement conditions of interest prior to recording the spectrum to enable stable measurements; values between 5 min and 30 min are reported for HT-PEMFCs,[264–267] and the necessary time may differ with operating conditions. The resulting spectra then only provides a snapshot of the impedance at this condition (*e.g.* potential, temperature, relative humidity, pressure, *etc.*). Therefore, many measurements may need to be taken depending on the application of characterisation data.

The gases used may also differ depending on the desired analysis. Generally, EIS is run with H_2 at the anode, and air (or O_2) at the cathode. This is most useful for analysing the fuel cell under typical operation, and allows analysis of ORR and oxygen mass transport impedances to be measured. However, by supplying N_2 to the cathode, these impedance mechanisms along with water and electrochemical heat generation are removed. By neglecting the anode by assuming fast HOR and no H_2 mass transport limitation, the fuel cell impedance is the sum of the cathode catalyst layer impedance, membrane resistance, and other electronic resistances of the system.[268] Therefore, the proton resistance and charge double layer capacitance of the cathode catalyst layer can be determined by fitting a transition line model, where the 45° line at high frequencies is related to the proton resistance.

EIS is very useful for investigating different mechanisms within the fuel cell *e.g.*, charge transfer, double-layer capacitance, mass transport of reactant species, and ohmic resistance.[269,270] This is due to its ability to measure the impedance evolution and accumulation over a wide frequency range, which enables separation of mechanisms depending on their characteristic time constants. This capability has been used to determine the effects of operating conditions, degradation, and design optimisation.[145,179,271–274] EIS data can be analysed using equivalent circuit models (ECMs). These models can consist of a combination of resistors, capacitors, inductors, and specialised electrochemical components (Warburg diffusion and constant phase elements).[270] Analysis using ECMs is not straightforward due to the complexity of fuel cell operation. EIS data can be fit using a variety of ECMs, and the more circuit elements, the closer the fit. However, purely empirical models lack insight into the underlying physical and chemical parameters.[20] To combat this, physically-representative models are used, and the simplest and most common is the Randles circuit.[270] This ECM consists of a resistor representing the electrolyte resistance connected in series to a parallel combination of a resistor and capacitor representing charge transfer resistance and a double layer capacitance, respectively. However, the simplicity may mean that fidelity is compromised, and impedance processes may be missed. Other more complex models are used to represent a greater number of different impedance mechanisms within fuel cells, these are often developed in conjunction with distribution of relaxation times (DRT) analysis.[275,276] Applying these more complex models will require knowledge of what features are expected in the spectrum and an understanding of the frequency dependence.

These models have been used to analyse the effects of operating conditions in more detail as specific resistance and capacitance values are attributed to individual impedance mechanisms.[186,275,276] The ECMs can also be used to model fuel cell performance with dynamic capability.[276–278]

Despite the usefulness and ubiquity of EIS, difficulty remains in obtaining valid spectra, and proof of the data validity is often missing from studies in the literature. To be valid, EIS measurements must fulfil certain criteria:[260,270]

• Linearity – the response to the input perturbation must be linear- or at least pseudo-linear- for the mathematical analysis to be meaningful. The relationship between voltage and current in a fuel cell is often non-linear. Therefore, sufficiently small perturbations are required to achieve a pseudo-linear response

 This journal is © The Royal Society of Chemistry 2024

Open Access Article. Published on 07 March 2024. Downloaded on 1/20/2026 7:35:49 PM.
This article is licensed under a Creative Commons Attribution 3.0 Unported Licence.

such that the system is under steady-state conditions. However, the signal amplitude must be high enough for a sufficient signal-to-noise ratio.

• Stability – the system response to the perturbation must not cause the system to drift from steady-state. This can be an issue for fuel cells at low frequencies as the system undergoes changes *e.g.*, oxide layer growth, adsorption of impurities, temperature changes, *etc.*

• Causality – the output of the system must only be caused by the perturbation input.

A validity check can be applied to the EIS data to determine if any corruption occurred. The Kramers–Kronig (KK) transformation is often used to test the validity. The KK relation links the real and imaginary impedance and allows one of these contributions to be uniquely calculated if the other is known. The KK transformations were derived under the same assumptions required for valid EIS: linear, stable, and causal.[260] Therefore, if the impedance contribution calculated using the KK transformation does not adequately match the measured spectra, the validity criteria have been violated. The difference between the measured and KK-generated spectra are termed "residuals", Fig. 8 shows an example of KK and EIS-generated spectra along with KK residuals. The residual limit for determining if the data is valid is not defined mathematically and can vary between studies. Generally, the residual limit is 0.5–1.0%.[265,267,279] It is also important to inspect the residuals across the frequency range in order to determine systematic errors that may not yield residuals high residuals but still result in invalid data.[280] Maintaining constant conditions during the measurement *e.g.*, temperature, gas flow, pressure, *etc.*, is required to prevent instability or time-variance that can result in invalid data. It is important to note that many EIS studies of PEMFCs in the literature do not include the validity check, and thus interpretation of the EIS data is problematic.

There are no significant differences between conducting EIS measurements for HT-PEMFCs compared to LT-PEMFCs. At the highest frequencies, inductive behaviour is often visible and is caused by the test cables and equipment.[269,280] This has been reported in both HT-PEMFCs and LT-PEMFCs.[272,279,281] The Z_{re} (also denoted: Z') axis intercept at high frequencies, often referred to as HFR, is ascribed to ohmic resistance.[262] As proton conductivity dominates ohmic resistance, the intercept is used to indicate electrolyte characteristics.[267,279,282] This applies to both LT and HT technology and the only difference is the proton conductivity mechanisms. EIS spectra commonly display one or more arcs. These arcs are attributed to different impedance mechanisms. HT-PEMFCs share many of the same impedance mechanisms, and these will show up in the spectra in a similar way to LT-PEMFCs. These include charge transfer and mass transport limitations. These can then be deconvoluted further using DRT analysis which can provide attributions to electrode-specific processes such as proton conduction, HOR, ORR, and H_2 and O_2 transport impedance.[265]

The main difference when analysing HT-PEMFC EIS spectra is the behaviour at low frequencies. LT-PEMFCs have been repeatedly reported to exhibit an inductive loop at low frequencies (<0.1 Hz); but often studies do not show this behaviour, and

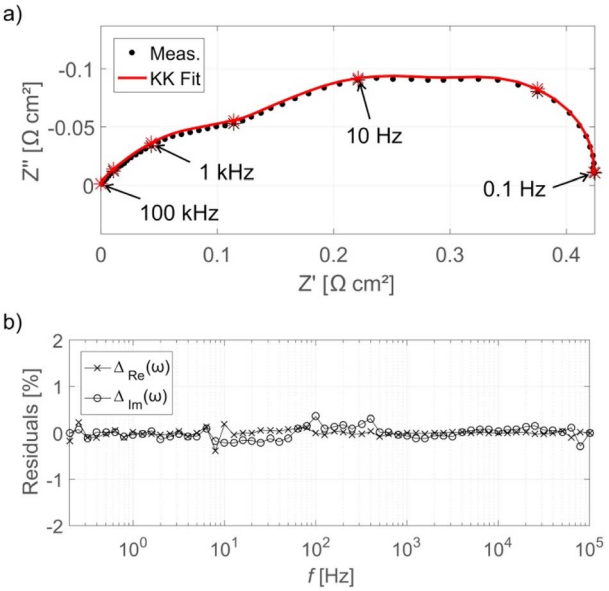

Fig. 8 (a) EIS Nyquist plot for HT-PEMFC operating at 160 °C at 0.3 A cm^{-2} with KK fit, and (b) KK residuals as a function of frequency. The EIS spectra have been normalised by subtracting the high-frequency real axis intercept. Reprinted from ref. 265, Copyright (2017), with permission from Elsevier.

it is unknown if the studies omit it or if it is physically absent.[269] An example of the inductive loop is shown in Fig. 9a. The locations of HFR, total polarisation resistance (total R), last measured point (LMP) which is typically limited by equipment or experimentation time, and the DC point which refers to the resistance that would be measured as the slope of the polarisation curve, are indicated.[269] The cause of the low-frequency inductive loop is disputed. One explanation for the loop involves side reactions with intermediate species. The multi-step ORR mechanism involves adsorption of species onto the catalyst sites and the formation of intermediates such as peroxide.[283–285] One study suggested the inductive loop was caused by an intermediate step and was not dependent on current or potential.[286] The inductive loop has also been predicted by models accounting for hydrogen peroxide intermediate formation as part of ORR. It has also been explained by the formation and relaxation of Pt oxide.[283,285,287] Another explanation involves water dynamics where the product water transport from cathode to anode at high current densities leads to a membrane resistance reduction.[288,289] It has also been suggested that the slow uptake of water by the membrane at high current densities and release at lower current densities causes the inductive loop.[290] The slow hydration of the ionomer may also contribute to this inductive effect.[291] These explanations may be valid under low relative humidity conditions, but other explanations may be required under fully humidified conditions.[269,290,291] CO poisoning is another explanation for the inductive phenomena.[292,293] Oxidation of CO and subsequent desorption of CO_2 results in an increase in the number of sites for H_2 chemisorption onto the Pt surface, reducing the charge transfer resistance.[294] Use of pure O_2 as the oxidant was reported to prevent the appearance of the

Open Access Article. Published on 07 March 2024. Downloaded on 1/20/2026 7:35:49 PM.
This article is licensed under a Creative Commons Attribution 3.0 Unported Licence.

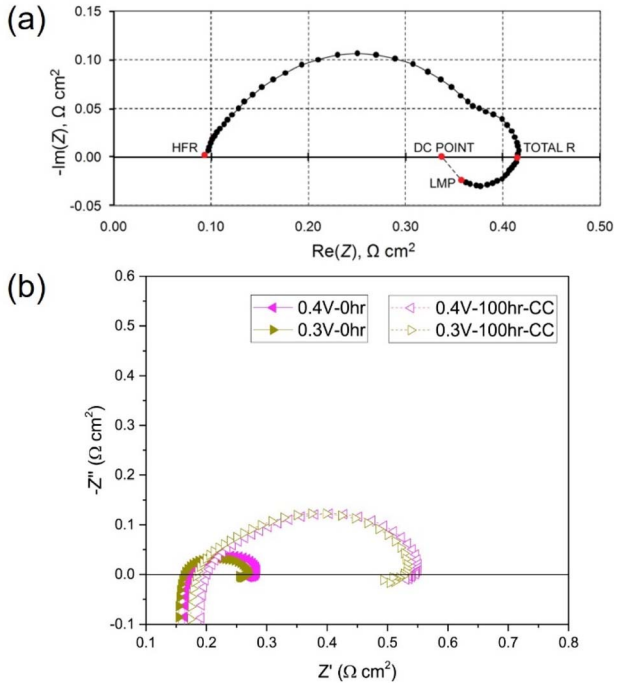

Fig. 9 (a) LT-PEMFC EIS Nyquist plot with inductive loop indicating high-frequency resistance (HFR), total *R*, last measured point (LMP), and DC point locations, reprinted from ref. 269 (open access); (b) HT-PEMFC EIS measurements showing inductive loop at various cell voltages before and after 100 h at 0.2 A cm^{-2}, reprinted from ref. 281, Copyright (2018), with permission from Elsevier.

inductive loop, this was attributed to the direct chemical oxidation of CO without intermediate steps.[294] Overall, the cause of the low-frequency inductive loop is still unclear and may depend on multiple different processes.[269]

There are very few studies that report low-frequency inductive behaviour for HT-PEMFCs (an example is shown in Fig. 9b). This may be for several reasons: (i) there are fewer EIS studies of HT-PEMFCs giving the appearance it occurs less frequently; (ii) the behaviour does occur but is not being reported; (iii) the changes in operating conditions *i.e.*, higher temperature and reduced water content mean that the behaviour appears only at lower frequencies than is being tested, or rarely occurs at all. There are studies that do report the inductive phenomena for HT-PEMFCs and solid acid fuel cells.[266,281,295] Within these studies, the loop is significantly smaller than in the LT-PEMFC studies. Different conclusions may be drawn from this observation. One is that the change in conditions is reducing the impact of intermediate species adsorption, Pt oxidation, CO poisoning, and/or water dynamics. This is feasible especially as ORR reaction rates and CO tolerance increase with temperature, and HT-PEMFCs do not rely on water for proton conductivity.[37] So far, the low-frequency inductive phenomena in HT-PEMFCs has been attributed to phosphate poisoning, although Pt oxide growth and relaxation may also contribute.[281,295]

EIS has also been used to investigate the effects of different operating conditions on HT-PEMFC impedance,[266] as shown in Fig. 10. The effect of increasing temperature on charge transfer is shown in Fig. 10a. The higher temperature was expected to improve the reaction kinetics, reducing charge transfer impedance and activation overpotential. A more complex relationship was visible at higher current densities, as shown in Fig. 10b. There were expected competing impacts of increased temperature on reaction kinetics and changes in humidification due to water vapour pressure changes.[266] Whereas, the effect of air stoichiometry was clear at 1.0 A cm^{-2}, decreasing the stoichiometry from 2.0 to 1.5 results in significantly higher mass transport impedance due, and likely caused inhomogeneous current density distributions. The effect of air humidification is shown in Fig. 10c and d. Increased humidification resulted in a decrease in HFR. This is expected as water is known to improve conductivity by increasing vehicular proton transport.[92] This improvement is offset by increases in charge transfer and mass transport impedance, expected to be caused by increased phosphate anion adsorption and oxygen diffusion resistance, respectively.[266]

In summary, EIS is a powerful tool for HT-PEMFC characterisation and modelling. Careful attention must be paid to the validity of the data, this is also true for LT-PEMFCs. And low-frequency inductive phenomena in HT-PEMFCs requires more research to determine the extent to which it affects HT-PEMFCs and the cause(s).

3.3.1 Distribution of relaxation times (DRT) analysis. DRT is becoming an increasingly used tool to analyse the EIS

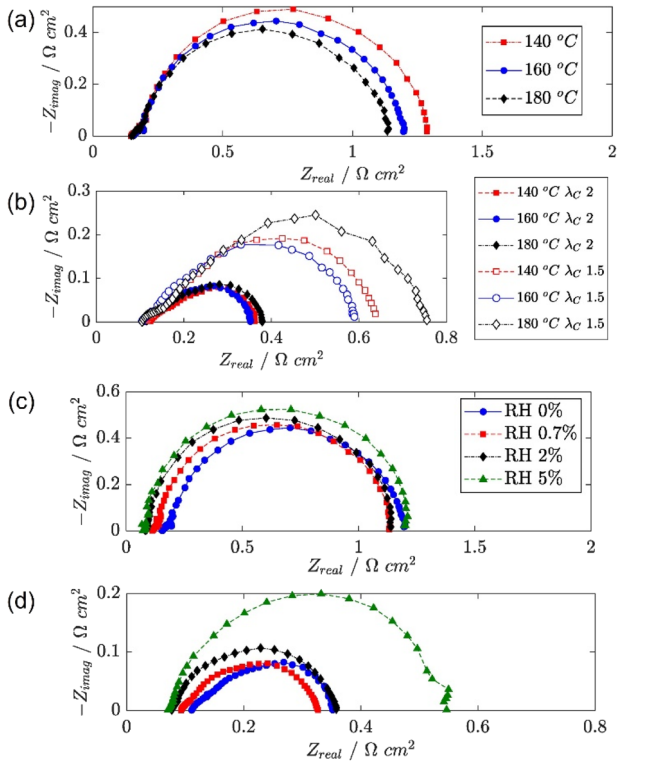

Fig. 10 HT-PEMFC EIS Nyquist plots of (a) temperature effect at 0.05 A cm^{-2}, (b) temperature and air stoichiometry effects at 1.0 A cm^{-2}, (c) air relative humidity effect at 0.05 A cm^{-2} and (d) 1.0 A cm^{-2}. Adapted from ref. 266 (open access).

This journal is © The Royal Society of Chemistry 2024

Open Access Article. Published on 07 March 2024. Downloaded on 1/20/2026 7:35:49 PM.
This article is licensed under a Creative Commons Attribution 3.0 Unported Licence.

impedance spectra of PEMFCs. DRT allows for each electrochemical process to be resolved by its intrinsic time constant, with the magnitude of each process assigned as a share of the total polarisation resistance. The distribution of the magnitude of each process as a function of frequency can be obtained.[265] This gives additional information on the impedance processes compared to the EIS spectra alone. For discussion on the theory and application of DRT, the reader is referred to existing literature.[275,279,296,297] A major benefit of DRT in the analysis of impedance spectra is the lack of *a priori* knowledge required and can be used for a model-free approach. This also provides more information about the number of features and approximate frequencies, allowing the user to construct physically-based ECMs using DRT analysis.[265,275,276] However, assignment of the features to processes and development of representative ECMs requires user expertise.

DRT analysis has been used in LT-PEMFCs to investigate transport properties of a commercial stack,[298] commercial stack fault characterisation,[29] analysis and modelling of electrode properties,[276,279,299] and investigation of low frequency inductive phenomena.[285] Fig. 11 shows the DRT plot for a HT-PEMFC, assignment of peaks, and relation to the individual impedance mechanisms within the EIS spectra. In this case, P1 is assigned to mass transport, P2 and P3 to the ORR, and P4–7 to anode-related processes such as charge transfer kinetics of the HOR.[265] In HT-PEMFC studies, DRT has already been applied to a variety of studies. The effect of operating conditions including CO concentration in the anode gas steam was investigated using DRT.[300] The results suggested the presence of CO increases HOR, ORR, and mass transport impedances. The use of a reference electrode allowed for individual electrode DRT analysis to be conducted. A DRT peak was reported in the anode analysis at around 100 Hz when a CO concentration of 5% was present. This peak was attributed to the influence of CO adsorption on charge transfer. The effect of air stoichiometry on the individual impedance contributions of mass transport, ORR, and HOR has also been investigated and are shown in Fig. 12a.[267] Increasing the air stoichiometry significantly reduced the size and increased the frequency of the peak associated with mass transport. Although there were diminishing returns, especially at stoichiometries above 3. A similar, but less prominent trend was observed in the main peak attributed to ORR when increasing the stoichiometry. However, a minor ORR peak and the HOR peak did not show this trend, and an explanation is not provided for this behaviour. These results support a similar stoichiometry investigation from a previous study.[265] In the same study, the effect of temperature was investigated, the DRT plot is shown in Fig. 12b. Higher temperatures resulted in a minimal decrease in the peak height associated with mass transport, and a larger decrease in peak height and shift to higher frequencies for the main ORR peak, attributable to faster reaction kinetics.[267] An increase in time constants for the minor ORR and HOR/proton transport peaks are not discussed in the study. The effects of activation procedure have been analysed using DRT.[155] The mass transport impedance was observed to decrease for all the activation procedures (galvanostatic, temperature cycling, current cycling,

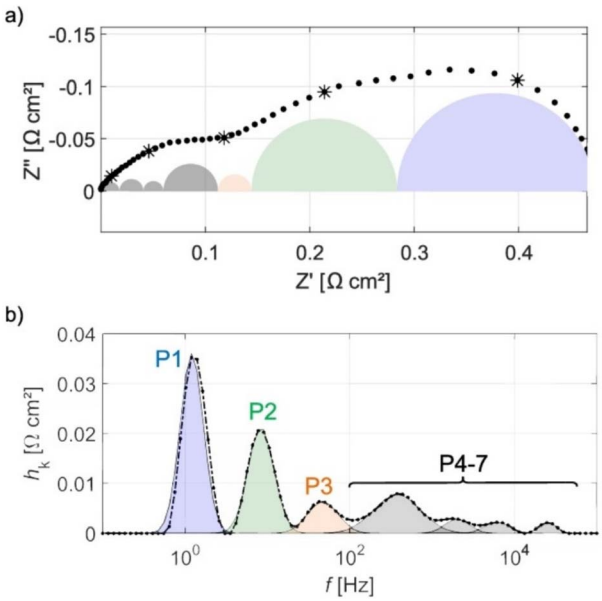

Fig. 11 (a) EIS spectra of HT-PEMFC operating at 160 °C at 0.3 A cm^{-2} with individual impedance contributions, (b) DRT plot showing deconvolution and assignment of impedance contributions. Reprinted from ref. 265, Copyright (2017), with permission from Elsevier.

and elevating backpressure). The time constant for ORR was seen to decrease for all procedures except temperature cycling, indicating an acceleration in the charge transfer during the activation process. The effects of catalyst layer morphology, composition and manufacturing method have also been investigated using DRT.[125,127] The use of a PtCo alloy resulted in a reduction in mass transport peak area, as well as a shift to higher frequencies for the ORR peak, indicating faster reaction kinetics compared to a conventional Pt/C catalyst.[127] An Fe–N–C was also included in the same work, and multiple additional mass transport impedance processes were indicated in the DRT analysis that were not present in the other catalyst compositions. This was explained by the Fe–N–C catalyst morphology exacerbating the issue of poor oxygen accessibility to the catalyst sites. Poor impregnation of H_3PO_4 into the cathode was also expected. The impact of CO and other species such as CO_2 have also been studied using DRT.[272,301] Generally, the introduction of CO and other species does not improve performance, but synergistic effects may occur when species such as H_2O, CO_2, and CH_3OH are also present. However, improvements appeared to depend on current density and can be minimal. A potential new application of DRT for HT-PEMFCs is the investigation of the inductive phenomena. Typically this behaviour is excluded in the analysis, with an exception for a LT-PEMFC study.[285]

The depth of DRT analyses varies between studies, and so too does the detail provided about data validation and parameter choice. DRT requires excellent measurement quality due to its sensitivity, and KK relations should be used to indicate validity.[265] Despite the lack of *a priori* assumptions, DRT is not straightforward. The DRT quality is sensitive to the number of measurement points in the impedance data.[302] The mathematical calculation of DRT poses challenges, and in order to obtain

Open Access Article. Published on 07 March 2024. Downloaded on 1/20/2026 7:35:49 PM. This article is licensed under a Creative Commons Attribution 3.0 Unported Licence.

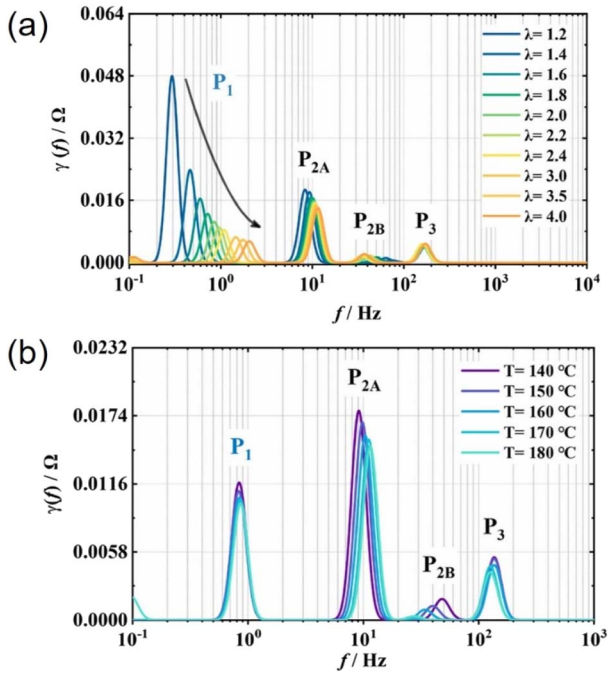

Fig. 12 DRT plots of (a) effect of air stoichiometry and (b) operating temperature on a 45 cm^2 HT-PEMFC at 0.2 A cm^{-2}. Adapted from ref. 267, Copyright (2022), with permission from Elsevier.

a stable numerical solution, Tikhonov regularisation is typically used.[302,303] This method requires the selection of a regularisation parameter, λ, which greatly influences the output DRT.[304] Optimal selection of λ may be obtained through an iterative process combined with user experience, the value should then be applied to all data within that specific dataset.[275] The regularisation parameter has a smoothing effect which is used to remove artificial, erroneous peaks. It is advised that λ should be as small as possible for good resolvability and as large as needed to suppress artefacts, and there is no effective "black box" method to determine this value, *i.e.*, λ must be determined by the user through careful experimentation and analysis.[304] It should also be noted that DRT approaches may extrapolate to frequencies past those used in obtaining the EIS data, meaning inaccurate conclusions could be drawn if impedance mechanisms did not fully evolve within the EIS measurement frequency range.

As DRT analysis uses EIS data, there are no specific considerations for HT-PEMFCs that do not apply to LT-PEMFCs regarding use of the technique, but knowledge of the differences between these systems is required for interpretation of results. And careful attention should be paid to the information provided on data validity when drawing conclusions.

3.4 Cyclic voltammetry (CV)

Cyclic voltammetry is a widely utilised technique to determine the ECSA in PEMFCs. The ECSA is calculated by dividing the charge density related to H adsorption/desorption (or CO oxidation) obtained in the CV by the product of the charge required to oxidise/reduce a monolayer of the adsorbed species and the catalyst loading.[305] The conventional *in situ* method involves supplying H_2 to the electrode of interest and N_2 (or another inert gas) to the other electrode. The first acts as the reference and counter electrodes, and the second is the working electrode. This technique is referred to as the "hydrogen adsorption/desorption" method, where the hydrogen underpotential deposition, H_{upd}, is used for ECSA calculations. The potential is scanned in forward and reverse directions at a rate typically in the range of 10–100 mV s^{-1}.[146,171,186,306]

This technique is frequently used in LT-PEMFC,[189,307–310] and HT-PEMFC ECSA measurements,[114,130,147,161,186,311] although it has been suggested that this method is unreliable for HT-PEMFC ECSA measurements due to phosphate adsorption suppressing the H_{upd} peaks, and high faradaic hydrogen evolution reaction currents superimposing pseudocapacitive H_{upd} currents.[116,312] The oxidation of a monolayer of CO or "CO stripping" is another common method for ECSA determination in HT-PEMFCs which makes use of the affinity of Pt to bind with CO, and is only partly affected by the problems affecting the H_{upd} method.[306] However, there are issues with side reactions that influence the ECSA determination at higher temperatures, and the CO adsorption itself is strongly temperature-dependent and a calibration curve needs to be established to measure ECSA based on oxidation of a monolayer of CO at the temperatures of interest.[116] There are several CO stripping methods to calculate ECSA. One method is to use the current of a second potential sweep as a baseline to determine the CO-related oxidation peak in the first sweep. Another method is to use a reference CV where no CO adsorption occurs, this can then be used to determine the CO-related oxidation peak when the CO monolayer is present. Both methods attempt to isolate CO oxidation from other current sources.[306] A third method involves the detection of CO_2 in the working electrode exhaust to infer the oxidation of the adsorbed CO and thus ECSA.[313] One study used these methods to investigate the effect of the partial pressure of water on the ESCA.[313] It was found that an increase in partial pressure of water above 10 kPa resulted in ECSA reduction when measured with both CV and exhaust CO_2 techniques. This was attributed to the uneven distribution of the PA/water mixture on the catalyst and flooding of porous electrode structure. ECSA values determined *via* CO_2 detection have been reported to have similar values to CO stripping using a reference CV across a wide temperature range (40–180 °C).[306] Fig. 13 shows the trends in ECSA values as a function of temperature using the three methods. The method using the second potential cycle as a baseline was deemed to overestimate ECSA due to the inability to distinguish between CO and other oxidation currents.[306] The CO_2 method has been shown to exhibit slightly lower ECSA values due to the CV methods being influenced by the formation of water and hydroxide species.[313] The CO_2 method requires a second cycle to be subtracted from the first to eliminate CO_2 that is not produced by CO monolayer oxidation but instead by oxidation of carbonaceous species within the cell.[306]

3.5 Linear sweep voltammetry (LSV)

Linear sweep voltammetry is a common technique for detecting electrical shorting and fuel crossover in PEMFCs.[314] The

 This journal is © The Royal Society of Chemistry 2024

Open Access Article. Published on 07 March 2024. Downloaded on 1/20/2026 7:35:49 PM. This article is licensed under a Creative Commons Attribution 3.0 Unported Licence.

technique involves the same gas supply and electrode designation as CV mentioned previously. Hydrogen that crosses from the anode to cathode should be fully oxidised and an instantaneous hydrogen oxidation current density is generated which allows for the estimation of hydrogen crossover rate.[315] The potential is typically scanned from approximately 0 V to around 0.5 V with slow scan rates, *e.g.*, 1–5 mV s^{-1}.

The measurement method is the same for LT-PEMFCs and HT-PEMFCs and has been used to determine the hydrogen crossover rate for both technologies, and is particularly useful in determining membrane degradation.[194,219,274,309,316] The hydrogen crossover was monitored over a 6000 h HT-PEMFC durability test. The crossover current density increased from around 0.5 mA cm^{-2} at the beginning of test to 13.9 mA cm^{-2} after 5705 h of operation. This was attributed to membrane thinning and the formation of pinholes and microcracks.[187] The impact of single-layer graphene (SLG) on hydrogen crossover has also been investigated for ultrathin (7.7 μm) PBI membranes.[274] The addition of SLG was reported to significantly reduce hydrogen crossover, resulting in higher OCV. After 100 h at constant current, the hydrogen crossover current density of ultrathin PBI MEA without SLG increased from 21 to 70 mA cm^{-2}, whereas the use of SLG resulted in a minor increase from 14 to 15 mA cm^{-2}.

3.6 Current distribution mapping

Local variations in the electrochemistry, activity, temperature, and humidity all produce current density inhomogeneities.[317] These inhomogeneities affect fuel cell performance and degradation, potentially causing damage to the membrane and catalyst layers.[318,319] There are various methods to measure the current distribution within the cell. The measurements are typically obtained by introducing a segmented electronically conductive component. This can be in the form of segmented electrodes, flow fields, or current collectors.[318,320] Printed circuit boards (PCBs) are often used to create segmented current collectors.[317,321,322] These methods involve physically altering the fuel cell which can affect operation and performance. A non-invasive method that has been used involves the calculation of current density from the magnetic field surrounding the fuel cell.[323,324]

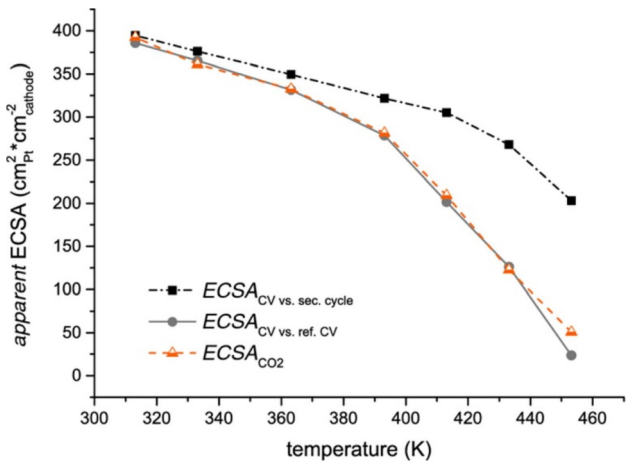

Fig. 13 Apparent ECSA trend as a function of temperature using three methods. Reprinted from ref. 306 (open access).

The current distribution mapping technique for HT-PEMFCs follows the same principles as for LT-PEMFCs. The materials used in the devices may differ due to the different operational environments. Components in HT-PEMFCs must be able to withstand the higher temperatures and presence of PA.

Current distribution mapping in LT-PEMFCs has been used to investigate reactant starvation,[318,320] start-up/shut-down,[250,317,325] effects of operating conditions on single cells,[319,321,326–328] effects of operating conditions on a stack,[329] and localised EIS.[327] One application of current distribution mapping used in HT-PEMFC research is the investigation of flow field geometry effects.[154,330] Fig. 14 and 15 show how this mapping technique has been used to investigate the impact on current density distribution of four different flow field patterns. This is important as current density distribution homogeneity is important to reduce hotspots. The serpentine and pin-type flow fields resulted in lower variation and more even distribution of current density compared to the parallel and interdigitated flow fields. Although, performance when using interdigitated flow channels was comparable to serpentine when using air at high flow rates. Interdigitated geometries have also been reported to achieve higher current and power densities than other geometries.[331,332] Recent work suggested the improvement when using interdigitated geometries is likely due to the enhanced convective mass transport in the GDL, rather than from the pressure and subsequent oxygen concentration increase resulting from the dead-end geometry.[332] The benefit of this is the reduced requirement of pressure drop compared to conventional designs such as serpentine, thus reducing parasitic power losses from the compressor.

The influence of CO concentration in the anode fuel supply from 0% to 3% has also been investigated using current density distribution mapping.[30] The results showed inhomogeneities in current distribution increased with increasing CO content, and this effect was worse at higher current densities. Current values were typically lower at the inlet and highest at the outlet, as increased poisoning effect was suspected at the inlet. Increasing the temperature from 160 °C to 180 °C reduced the relative difference between inlet and outlet current densities. It was also noted that load operation in potentiostatic mode resulted in more even current distribution than galvanostatic mode. Although the explanation for this is unclear.[203] In another study, the current density distribution within a HT-PEMFC stack operating under both hydrogen and reformate conditions was investigated.[51] Under hydrogen/air conditions with co-flow, the local current density was highest at the air inlet and lowest at the air outlet, which was explained by reactant consumption along the flow path. Under reformate/air co-flow conditions with an anode stoichiometry of 2, the depletion of both oxygen and hydrogen along their respective flow paths results in a greater degree of homogeneity. Although current is still higher closer to the anode and cathode inlets compared to outlets. Reducing the anode stoichiometry to 1.2 led to a significant increase in inhomogeneity which was attributed to CO

Open Access Article. Published on 07 March 2024. Downloaded on 1/20/2026 7:35:49 PM.
This article is licensed under a Creative Commons Attribution 3.0 Unported Licence.

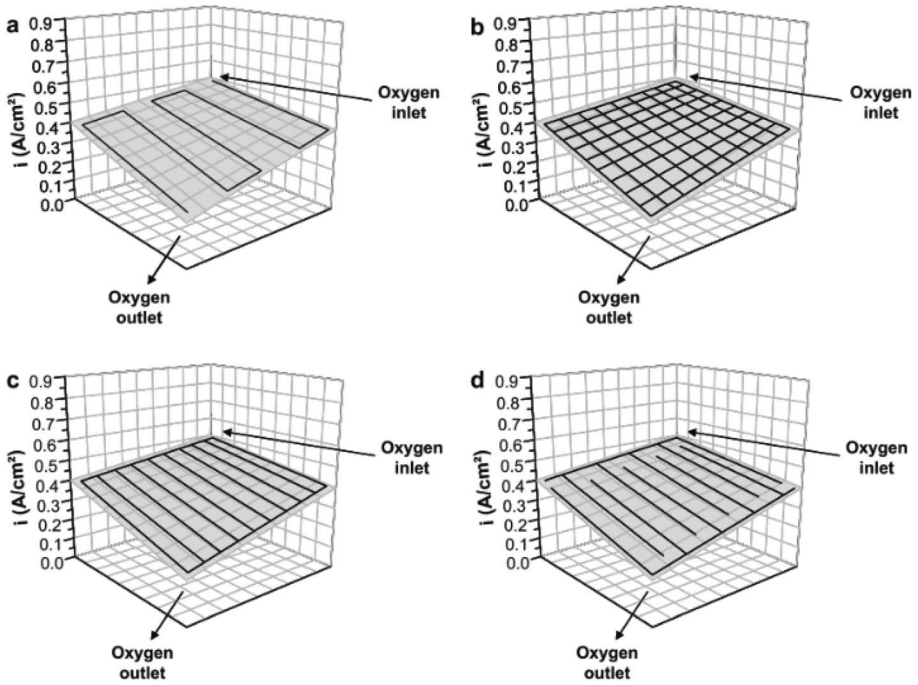

Fig. 14 Flow channel pattern overlayed onto current distribution map with oxygen inlet and outlet indicated. (a) Serpentine, (b) pin-type, (c) parallel, and (d) interdigitated. Reprinted from ref. 154, Copyright (2011), with permission from Elsevier.

poisoning. However, in this case local current density was highest at the inlet and lowest at the outlet. Operating in counter-flow mode was found to reduce the current density inhomogeneity compared to co-flow mode. Studies of the effects of reformate on LT-PEMFC current density distribution have also been conducted, but these use CO concentrations 3 orders of magnitude lower than HT-PEMFC. Once again, highlighting the significant improvement in CO tolerance of HT-PEMFCs.

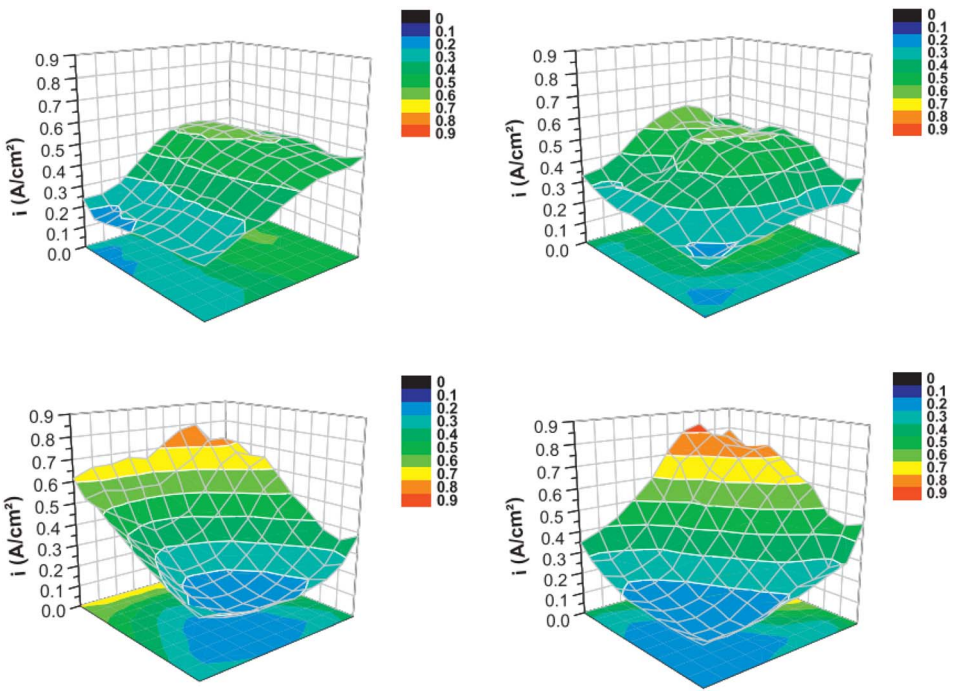

Fig. 15 Current distribution maps at an average current density of 0.38 A cm^{-2} (H_2/O_2 228/76 ml min^{-1}). Flow geometries correspond with those in Fig. 11. Reprinted from ref. 154, Copyright (2011), with permission from Elsevier.

 This journal is © The Royal Society of Chemistry 2024

Open Access Article. Published on 07 March 2024. Downloaded on 1/20/2026 7:35:49 PM. This article is licensed under a Creative Commons Attribution 3.0 Unported Licence.

Other applications of this technique include durability testing,[151,153] effect of catalyst layer deposition,[333] effects of reactant stoichiometry using local EIS,[334] and fuel starvation,[190,335]

Potential future opportunities for this technique to be used in HT-PEMFC include the effects of start-up and shutdown processes, particularly under sub-zero conditions. As mentioned in Section 2.2.4 there are several start-up strategies that are typically analysed regarding time taken to heat up rather than impact on cell performance, and using current distribution mapping to assess these different methods may provide useful insight. As noted previously, sub-zero operation of HT-PEMFCs is likely to be easier than LT-PEMFCs due to the reduced sensitivity to liquid water.[115,185] Greater understanding of degradation and inhomogeneities at these conditions could be provided by current distribution mapping, as long as the device is capable of operation under these conditions.

4. X-ray techniques

Techniques such as those using X-rays and neutrons provide detailed material information that is not accessible using electrochemical techniques. These techniques provide useful information about the internal structure and processes occurring within the MEA spanning nm to mm length scales, which can be used in conjunction with electrochemical characterisation to progress development of fuel cell technology.

4.1 X-ray radiography and CT

X-ray computed tomography (X-ray CT) is now a widely used technique for analysing the morphology of PEMFCs across multiple length- and time-scales. The technique works by passing a beam of X-rays through a sample, with the X-rays that pass through the sample being collected by a detector. The attenuation of X-rays is proportional to the atomic number, as well as the density of the material. Radiographs are collected at angles through 360°, termed "projections", and these projections are then reconstructed using a computer algorithm to create a 3D dataset comprising of voxels (volume pixels).

X-ray CT is a particularly adaptable technique, owing to the fact that multiple lenses and optics can be added to the detector to match the spatial resolution to the feature of interest, allowing for features from catalyst layer pores to flow fields to be resolved.[336,337] Furthermore, as well as *ex situ* studies of PEMFC morphology, *in situ*/*operando* studies are now becoming more common for time-resolved studies of PEMFCs.

4.1.1 *Ex situ* studies. Owing to the simple nature of *ex situ* studies, they are commonly used for analysing component morphology. *Ex situ* studies of LT-PEMFCs have been applied to studying the morphology of different features across multiple length scales.[338] Comparative studies have investigated the wettability and water breakthrough in fresh and degraded GDLs,[339] and comparison of catalyst layer morphology pre- and post-AST.[340] However, since direct comparison of samples at the beginning and end of life is not possible, the results of such studies are mainly qualitative. A more detailed discussion of *ex situ* X-ray CT for LT-PEMFCs can be found in the review by Tan *et al.*[341]

Since HT-PEMFC research is not as mature as for LT-PEMFCs, most of the studies carried out using X-ray CT have been *ex situ*, and the majority have focussed on the GDE. Diedrichs *et al.*[271] and later Hoppe *et al.*[342] used *in situ* compression rigs to correlate morphology changes in the GDL to fuel cell performance, arising from different compression levels and different flow-field misalignments, respectively. Start-stop conditions have also been investigated in HT-PEMFCs using X-ray CT, including studies into the idling temperature, showing that degradation leads to catalyst deactivation and pore collapse in the GDE,[343] as well as a decrease in tortuosity of the GDL.[219]

As well as understanding the relationship between morphology and performance, *ex situ* X-ray CT has been used to investigate PA behaviour across the MEA. These have included visualisation of PA migration away from the membrane into the GDL fibres as a result of operation,[69,344] and demonstration that the presence of an MPL can enhance PA redistribution in the catalyst layer, but prevent PA leaching into the flow channel, a common challenge for HT-PEMFC operation.[68] PA has also been injected into different GDL materials and the 3D invasion pathways were investigated, as well as the effect of intrusion through an MPL (Fig. 16).[69] Because of the poor contrast between PA, membrane, MPL and GDL, synchrotron X-ray sources have been widely used in these studies because of the higher flux and enhanced contrast that can be achieved.[68,69] However, recent work by Bailey *et al.* has proven that lab-based X-ray CT can be used for imaging the PA distribution, when combined with a machine learning (ML) approach to segmentation.[344] This work was extended to show that the addition of SLG can somewhat block the release of PA into the GDL/MPL.[274] However, this work still relies on the method of subtracting a "dry" scan containing no PA from a "wet" scan where PA has been introduced to the same component *e.g.*, GDL (Fig. 16). This is not ideal as it increases imaging and analysis complexity and limits *in situ* and *operando* studies where morphology may change. Future work should continue to find methods for improving contrast/segmentation of phases in HT-PEMFCs; for example, by applying deep-learning algorithms for segmentation.[345]

As well as microscale studies of MEA morphology, X-ray nano-CT has been used to study the pore-structure of LT-PEMFC catalyst layers.[338,346,347] Whilst unable to resolve individual particles of the catalyst layer or MPL, X-ray nano-CT can be used to investigate the morphology of these layers,[348] as well as the pore size distribution, with the comparison of results to mercury intrusion porosimetry (MIP) showing that nano-CT can capture information about pores greater than 50 nm in diameter.[347] X-ray nano-CT has also been used to study changes in the nano-scale morphology of the catalyst layers before and after AST,[349] with results showing an increase in the average pore size from the beginning to end-of-life (EOL) sample with a decrease in the porosity. There is some opportunity for X-ray nano-CT of HT-PEMFC catalyst layers, although since the properties of low-

Open Access Article. Published on 07 March 2024. Downloaded on 1/20/2026 7:35:49 PM.
This article is licensed under a Creative Commons Attribution 3.0 Unported Licence.

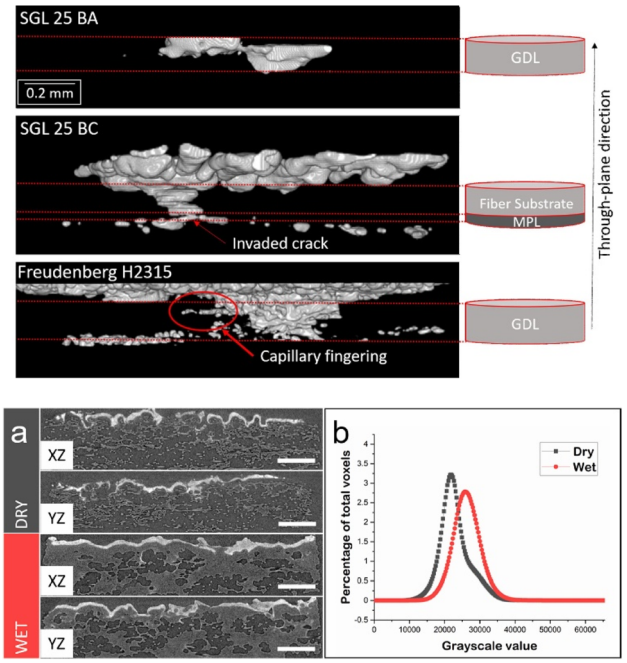

Fig. 16 PA breakthrough in various GDLs, with and without an MPL (top), reprinted from ref. 69, Copyright (2017), with permission from Elsevier; lab-based X-ray CT of dry and wet GDEs, with the differences between dry and wet GDL samples, (a), highlighted by the histogram, (b), (bottom), reprinted from ref. 344, Copyright (2021), with permission from Elsevier.

and high-temperature catalyst layers tend to be similar, the scope for novel nanoscale investigations is potentially limited.

4.1.2 *In situ*/*operando* studies. For LT-PEMFCs, *in situ*/*operando* X-ray CT has been most commonly used for two types of study: observing water formation/migration in the GDL, and degradation of the MEA components. Studies have been used to observe water dynamics in the GDL,[350–353] as well as studying the preferential water formation under the land regions over the channel regions both in the GDL and MPL.[354,355] Furthermore, cell temperature and relative humidity have been shown to affect water transport properties,[356] with *operando* X-ray radiography highlighting that different amounts of liquid and vapour water are present with varying operating conditions. The design of different fuel cell fixtures for multi-length scale imaging of water in LT-PEMFCs has been described by Kulkarni *et al.*[357] Degradation studies have focussed on the use of ASTs to target specific degradation modes inside the MEA on a time-scale more reasonable for *in situ*/*operando* studies. The first studies carried out by White *et al.* observed degradation in the catalyst layer using an AST designed by the researchers.[358] Later work by the group extended the investigation to include the joint-visualisation of water formation in the GDL as well as degradation of the catalyst layer.[359] Since it is widely accepted that the current, temperature and humidity across PEMFCs is non-uniform, other work using *in situ* cells highlighted the variation in degradation levels across the cathode catalyst layer from inlet to outlet.[360] Other degradation modes that have been probed using X-ray CT are related to membrane degradation, where cracks formed in the membrane during cycling have been observed.[361,362]

In situ/*operando* X-ray CT studies of HT-PEMFCs are emerging, with a focus primarily on PA distribution in the MEA. Halter *et al.* used *operando* X-ray CT to study the effect of current on the re-distribution of PA in the MEA of a HT-PEMFC. Results showed that PA breakthrough from the membrane to the catalyst layer happened only in the anode, and only in regions where the catalyst layer and MPL cracks overlapped.[157] This highlights the presence of a potential degradation mechanism for HT-PEMFCs that could be studied in more detail over a longer period of time in future studies. Further work by the group also highlighted that by designing catalyst layers with controlled crack widths, connectivity and accessibility, PA migration from the catalyst layer can be mitigated.[126]

Remaining challenges for *in situ*/*operando* studies of HT-PEMFCs is the development of cells suitable for imaging that can also achieve elevated temperatures of 160 °C. Whilst this is more feasible for beamline-based experiments, owing to the larger spaces and cell sizes that can be used because of the higher beam flux, achieving this in the small cavity of a lab-based system is a challenge. Difficulties remain when separating the PA from other components of the fuel cell during the segmentation as part of the analysis, this is typically overcome using a subtraction method whereby the GDL is first imaged without PA and this dataset is subtracted from the main dataset of interest;[69,157,344,363] however, this is time-consuming and limits *in situ*/*operando* studies. The authors recently reported the use of a contrast enhancement agent to overcome this issue in HT-PEMFC X-ray imaging.[165] The agent used was a Cs compound which acted as a phosphoric acid tracer. The higher atomic number of Cs significantly improved the contrast between the PA and surrounding materials. This technique was demonstrated using an *in situ* study of the hot-press process. Radiographs before and after hot-pressing, with and without the tracer, are shown in Fig. 17a–d. The tracer allowed visualisation of the PA in the electrode (appearing dark due to X-ray attenuation), which was imaged in real-time (videos available in the supplementary data of the source publication).[165] Orthoslices from the reconstructed X-ray CT data are shown in Fig. 17e–h. The PA appears bright with high contrast, making it easily distinguishable from the other materials, allowing for simpler image analysis without the need for the subtraction of a reference dataset. Nonetheless, innovations in fixture design, cell operating environments, and post-scan analysis techniques will bring about significant advancements for studying PA dynamics, as well as HT-PEMFC MEA degradation.

4.2 X-ray absorption spectroscopy (XAS)

X-ray absorption spectroscopy (XAS) is a technique that can be used to study the local environment of PEMFC catalysts, which includes information about the electronic structure and redox state, as well as the coordination environment and bond lengths around atoms. XAS works by delivering X-rays to a sample, upon which they are absorbed, resulting in the release of a photoelectron of a specified energy, and a corresponding

 This journal is © The Royal Society of Chemistry 2024

sharp increase in the absorption intensity, or 'edge', in the XAS spectrum. There are two main components of XAS spectra that can be investigated: extended X-ray absorption fine structure (EXAFS) and X-ray absorption near-edge spectroscopy (XANES). The differences are the energy at which the features occur. In EXAFS, higher energies are probed, where absorptions give information about inter-atomic lengths and coordination numbers of atoms. XANES probes the absorption edge of an element, which allows the oxidation state and symmetry of elements in the sample to be understood.

Open Access Article. Published on 07 March 2024. Downloaded on 1/20/2026 7:35:49 PM.
This article is licensed under a Creative Commons Attribution 3.0 Unported Licence.

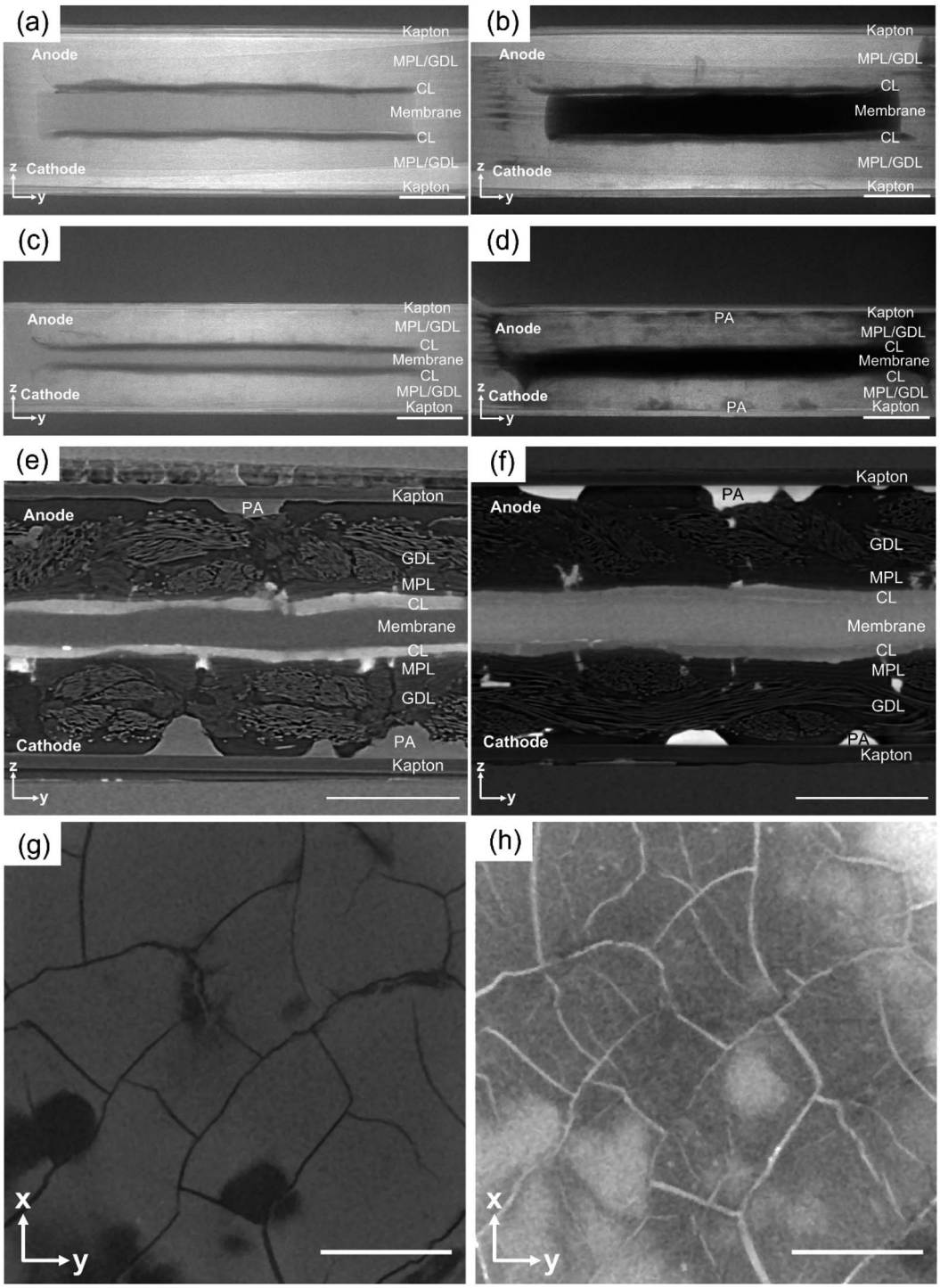

Fig. 17 A comparison of the effect of using a contrast enhancement tracer on PA visualisation during HT-PEMFC hot-pressing. Radiographs: (a) hot-press start – no tracer (b) hot-press start – with tracer, (c) hot-press end – no tracer, and (d) hot-press end – with tracer. Orthoslices of 3D reconstructed datasets: (e) no tracer and (f) with tracer. Cathode cracks and PA visualisation: (g) before hot-press and (h) after hot-press. All scale bars are 500 μm. Reprinted from ref. 165 (open access).

Open Access Article. Published on 07 March 2024. Downloaded on 1/20/2026 7:35:49 PM.
This article is licensed under a Creative Commons Attribution 3.0 Unported Licence.

Whilst XAS has been widely used for *ex situ* characterisation of novel PEMFC catalysts for both LT-PEMFCs and HT-PEMFCs.[364–367] *In situ* and *operando* studies are the ideal use of XAS, and are thought to be powerful tools for developing new catalysts with higher activity and stability.[368] The ability to study and identify changes occurring within the catalysts during operation will ultimately inform the development of novel, durable catalysts. This is especially important when considering the need to reduce the amount of Pt in the catalyst layer, or removal altogether. *In situ*/*operando* XAS studies have been carried out on both three-electrode and two-electrode cells.[369] The difference between these is that three-electrode cells operate in an aqueous environment, which do not fully represent the operating conditions of PEMFCs; studies are typically done at room temperature, with no gas flow to/from the electrodes. In contrast, two-electrode cells operate under standard fuel cell conditions, with elevated operating temperatures, gas flow on the anode and cathode and water formation/removal through the flow channels. Thus, with the change from three- to two-electrode cells, the behaviour of electrocatalysts under *operando* conditions can be observed.[369]

For HT-PEMFCs, XAS has been used in a number of studies for investigating catalyst poisoning.[152,214,370,371] *Operando* XAS has been used to track the changing adsorption of species, from H, to PO_4 to O, with increasing voltage, and PO_4 coverage at different temperatures (Fig. 18).[152,372] *In situ* half-cells, with and without electrolyte flow under ambient conditions, have also been used to study these adsorbed intermediate species in more detail.[371] While these studies shed light on the catalyst poisoning mechanisms in HT-PEMFCs, there is clear opportunity to extend such studies to *operando* systems operating at standard and elevated temperatures, to further elucidate the poisoning mechanism and allow for improved catalyst layer design. Given that HT-PEMFCs are tolerant to less pure hydrogen, adsorbates on the anode were studied using *in situ* XAS, using an anode gas feed containing CO and water to represent reformate hydrogen.[214] Results showed that CO concentrations above 2% significantly decreased the HOR activity on the anode.

Recent work has shown it is possible to spatially resolve the XAS spectra across a catalyst layer using XAS-CT, which collects XAS information at each projection during a CT scan.[373] This has allowed for a range of studies of catalysts, including observation of heterogeneous degradation and ceria-migration occurring in LT-PEMFC MEAs during stress-testing.[374,375] Applying similar methods to HT-PEMFCs represents a new opportunity for XAS-CT. Furthermore, the emergence of dedicated beamlines for *in situ*/*operando* XAS combined with a range of other X-ray techniques (XRD, X-ray CT, X-ray emission spectroscopy (XES)), such as the BL36XU beamline at Spring-8, will allow the realisation of such advanced experiments in the coming years.[376]

4.3 X-ray diffraction and XRD-CT

X-ray diffraction (XRD) is used to study the crystalline structure of samples. Incident X-rays focussed on the sample are scattered by the atomic planes in the sample and if they are coherent, the diffracted X-rays are collected at the detector. Information about the crystal lattice can be obtained, as well as changes to the lattice parameters if carrying out *in situ*/*operando* studies. Information about phase changes can also be obtained since different compounds will have different crystal structures.

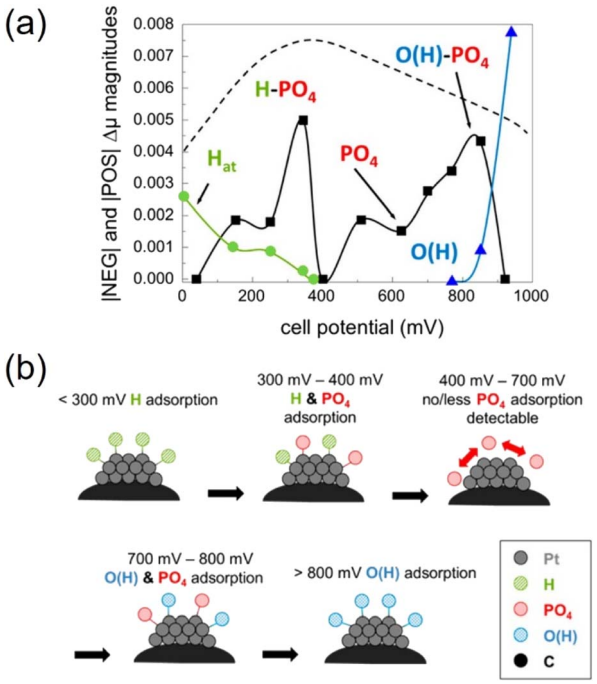

Fig. 18 (a) Coverage of different adsorbates at across cell potential range, dashed line indicates expected PO_4 coverage according to He *et al.*,[372] (b) diagram illustrating adsorbate condition at different cell potentials. Figures reprinted with permission from ref. 152, Copyright (2013) American Chemical Society.

XRD has been widely used for PEMFCs, especially for analysing new materials. Since each phase has a unique set of diffraction lines and intensities, various features of novel HT-PEMFC components have been characterised. This includes the study of novel catalysts, like PtNiCu,[377] confirming the successful distribution of GO in PBI/GO membranes,[378] or analysing the coating of Ni onto electrospun fibres for novel GDEs.[379] XRD has also been used for studying degradation in HT-PEMFCs. Batet *et al.* conducted XRD over the course of a durability study of a HT-PEMFC stack, by extracting one MEA from the stack at each interval. XRD was then done on the anode and cathode catalyst layers, with results showing an increase in average crystallite size over the durability test.[380] XRD was also used to confirm the successful impregnation of silica nanoparticles into the PBI membrane, with results showing that an intermediate silica content leads to improvement in performance and a lower degradation rate.[381]

Regarding *in situ*/*operando* studies, a few studies have been conducted on LT-PEMFCs to monitor the evolution of Pt surface oxides in an operating fuel cell,[382] as well as in combination with small angle scattering (SAXS) to measure crystallite size and decouple different Pt degradation modes (like aggregation,

Open Access Article. Published on 07 March 2024. Downloaded on 1/20/2026 7:35:49 PM. This article is licensed under a Creative Commons Attribution 3.0 Unported Licence.

coalescence, Ostwald ripening).[383] The combination of XRD with spatially resolved CT (XRD-CT) has further advanced the ability to study fuel cell catalysts in five dimensions, *i.e.*, three spatial dimensions plus time and spatially-resolved diffraction data. XRD-CT involves the collection of XRD spectra for each voxel in a sample across a slice in a tomogram. Thus, as well as 3D information about the evolution of catalyst layer morphology that can be gathered from CT, the chemical composition of a phase can be spatially resolved, as shown by Martens *et al.*[384] In the same study, the group combined XRD-CT with SAXS-CT, to simultaneously resolve the local nanostructure of the PEMFC components. Whilst such studies hold significant potential for elucidating information about PEMFCs across length-scales, they are practically very challenging to carry out, which may limit their use in practice. Nonetheless, there is significant scope for application to HT-PEMFCs, for example, to study phenomena such as the phase change of PA during heating, and degradation of the various MEA components during ASTs.

5. Neutron techniques

The neutron interaction with matter occurs at the atomic nucleus, where incoming neutrons interact with the nucleus, resulting in both absorption and scattering. Unlike X-rays, where the strength of the interaction scales with the elemental number, Z, the neutron interaction is not related to the atomic number. Thus, elements across the periodic table have characteristic cross-sections, with the added advantage that some isotopes can be distinguished using neutrons. The advantage of this for PEMFCs is that common materials found inside fuel cells have widely different cross-sections, where the neutron cross-section is a measure of the interaction between the neutron and the sample, measured in barn (10^{-28} m^2). For example, hydrogen has a large cross-section, so appears bright in a neutron image, whereas carbon has a small cross-section and is less visible in neutron images. Thus, the visualisation of water is particularly possible, which cannot be as easily achieved using X-rays, given the low atomic number of hydrogen. Furthermore, given the isotope effect, deuterium (*i.e.*, hydrogen with a proton and a neutron) has a very low neutron cross-section and is hardly visible in neutron images, meaning that deuterated water can be used for humidification to further differentiate between water formed from the electrochemical reaction and water from humidification.

5.1 Neutron imaging

The use of neutrons for imaging is one of the most widely used applications of neutrons for PEMFCs. Because of the relatively low flux of neutron sources, the trade-off is that spatial resolutions (*i.e.*, the size of the smallest resolvable features) are typically on the order of 10–100 μm.[385,386] Furthermore, exposure times for each radiograph are on the order of milliseconds (for high-speed imaging) to minutes (for high-resolution imaging),[387] with longer exposure times reducing the signal-to-noise ratio (with a resulting loss of temporal resolution). The result of these two conditions is that the feature of interest, especially for *operando* studies, tends to be water formation in the flow channels. Most studies have been radiography studies, where a 2D radiograph, which is an averaged image through the through- or in-plane direction, is collected. These studies are normally time-resolved, meaning that images are gathered continuously throughout an experiment. Through-plane measurements are performed to understand the distribution of water along the length of the flow channel, with many studies on LT-PEMFCs observing the tendency for water to pool at the bends of serpentine flow channels,[388] or studying the effect of introducing multiple serpentine channels into the design.[389] In-plane measurements are done with the cell in line with the beam direction and can be used to observe the back-diffusion of water into the anode flow channels,[390,391] as well as studying the preferential formation of water under "land" regions (rather than under channel regions) during operation.[392] Advances in beamline technologies mean that the spatial resolution achievable using neutron sources continues to improve. Pixel sizes as low as 2.5 μm have been reported,[393] which is a particular advantage for in-plane studies, since it allows for water in each layer of the MEA to be resolved. Finally, LT-PEMFC start-up has been investigated using neutron radiography to observe the formation of ice during cold-start,[394] the phase transition between ice and liquid water,[395] and the effect of residual water in the flow channels on the start-up profile of LT-PEMFCs.[396] Such start-up behaviour is also of interest for HT-PEMFCs, as will be discussed later in the section.

As well as using in- or through-plane imaging, isotope exchange has been applied in neutron studies of LT-PEMFCs. Since the cross section of deuterium is much smaller than that of hydrogen, switching the inlet anode gas between H_2 and D_2 has allowed for distinction of the ion exchange in the membrane,[397] as well as water exchange between the GDL and the flow channels.[398]

For HT-PEMFCs, the effect of water on fuel cell performance is less of a concern during operation, since operating temperatures are above 100 °C.[22,47] This means that liquid water is less likely to exist in a transient form in the GDL or flow channels during normal operation. Thus, the majority of studies using neutrons carried out on HT-PEMFCs have taken advantage of H/D isotope contrast to monitor acid distribution and exchange of protons/deuterons through the membrane during operation. Work by Arlt *et al.* used H/D contrast to monitor the distribution of hydrogen in a PBI membrane.[399] By switching the anode feed gas between hydrogen and deuterium, the exchange between protons and deuterons could be observed. It was found that exchange occurred first at the gas inlet, with exchange at the gas outlet occurring later (Fig. 19a). Later work by Lin *et al.* built on this to monitor the rate of exchange at different current densities, with increasing current density resulting in a faster exchange through the anode flow channels (Fig. 19b).[400] The movement of PA through the cell has also been studied, with the amount of PA measured from radiographs being in reasonable agreement with the expected amount of acid inside the cell.[401] Deuteration was also used in this study to observe isotope exchange at different dewpoints of 30 and 70 °C.

Open Access Article. Published on 07 March 2024. Downloaded on 1/20/2026 7:35:49 PM.
This article is licensed under a Creative Commons Attribution 3.0 Unported Licence.

A handful of neutron tomography studies have been carried out so far on LT-PEMFCs. Because the flux of neutron sources are relatively low, exposure times for imaging have typically been on the order of multiple seconds. Thus, early studies carried out a single tomography on the order of hours.[402,403] High-resolution neutron tomography has been used in recent years for observing fine structure, such as work by Manzi-Orezzoli *et al.* to study coating on GDLs, combined with X-ray CT, with spatial resolution down to 10 μm.[404] Alrwashdeh *et al.* reported a voxel size of 6.5 μm for the study of water distribution in different GDL materials, although the exposure time for a single radiograph, in this case, was still 15 s.[405] Most recently, work by Ziesche *et al.* showed that it was possible to collect a single tomogram in 40 s, which allowed for *operando* monitoring of water distribution in the flow channels.[406] Owing to the third spatial dimension, the volume of water was quantified, allowing for comparison of the actual volume of water residing in the flow channels to the theoretical volume calculated according to Faraday's law.

With these recent advancements in 3- and 4D neutron imaging, there is clear scope for similar studies to be conducted on HT-PEMFCs. Furthermore, whilst the radiography studies of HT-PEMFCs described here show some initial understanding of ion-exchange and PA migration, there is considerable opportunity for studying the role of water during start-up and shut-down of HT-PEMFCs in four dimensions, as well as investigating freeze–thaw dynamics.

5.2 Neutron scattering

During neutron scattering, neutrons scattered by the sample are collected and analysed and neutrons transmitted through the sample in the plane of the incident beam are ignored. In comparison to neutron imaging, which has a relatively low spatial resolution (on the order of microns), neutron scattering experiments can resolve changes at the angstrom level,[407] meaning it is a powerful technique for probing properties of electrocatalysts, catalyst layers, and diffusion in PEMFCs.

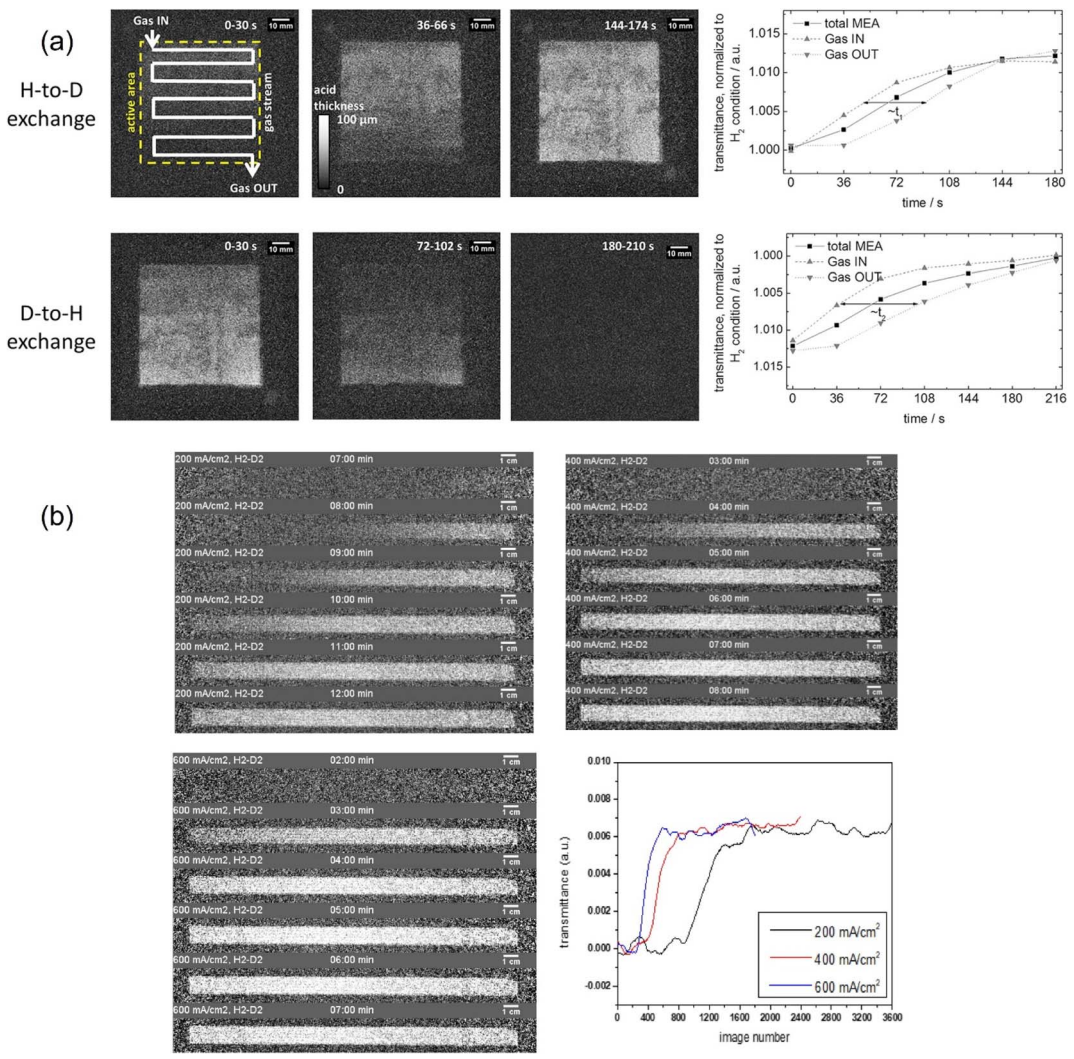

Fig. 19 (a) Neutron radiographs showing the H-to-D and D-to-H exchange in a HT-PEMFC operating at 160 °C, reprinted from ref. 399, Copyright (2015), with permission from Elsevier; and (b) the effect of current density (200, 400 and 600 mA cm^{-2}) on the speed of H-to-D exchange, with faster exchange at higher current density, reprinted from ref. 400 (open access).

 This journal is © The Royal Society of Chemistry 2024

Open Access Article. Published on 07 March 2024. Downloaded on 1/20/2026 7:35:49 PM.
This article is licensed under a Creative Commons Attribution 3.0 Unported Licence.

Furthermore, as with imaging, H/D isotope distinction is used during scattering experiments to allow for distinction between the "mobile" protons contributing to structural diffusion and those which are bound to the polymer chain.[408] As with imaging, neutron scattering experiments must be done at national facilities, since neutron sources are not available in the lab. There are different types of neutron scattering experiments, with two of the most common being quasi-elastic neutron scattering (QENS) and small-angle neutron scattering (SANS). They are distinct in that QENS experiments are spectroscopic and are used to study dynamics by measuring changes in neutron velocity. In contrast, SANS uses diffraction to study the structure of samples by measuring the change in neutron direction.[409,410]

In situ SANS has been used to study water dynamics in the catalyst layer of LT-PEMFCs, in combination with neutron radiography (NR) for capturing macroscale information about water distribution.[411] Furthermore, information about local hydration, as well as catalyst layer microstructure, was elucidated using the technique, including the use of H_2O/D_2O.[412] Contrast variation (CV)-SANS allows for the investigation of partial scattering functions, *i.e.* the scattering function of each component in a sample, such as the constituent materials of a catalyst layer ink.[413] Thus, the local structure of the catalyst layer components, Pt, carbon and ionomer, can be deconvoluted. For LT-PEMFCs, CV-SANS studies have included investigations into the effect of Pt-loading on ionomer adsorption, where the ionomer layer decreased as Pt-loading increased.[414] Further work by Harada *et al.* used CV-SANS to distinguish between adsorbed ionomer (forming a thin film on the Pt-surface) and deposited ionomer (found at throats in aggregated carbon particles).[415] Given the importance of electrolyte/Pt interfaces in HT-PEMFCs, CV-SANS is also expected to be a useful technique for studying novel catalyst layer designs or compositions with optimised performance as research into HT-PEMFC catalyst layers continues to increase.

For HT-PEMFCs, SANS has been applied to the study of catalyst layers, where the structure of a range of catalyst layers was studied across a range of length scales, by including wider angles.[416] SANS was also combined with SAXS to highlight the structure of different components in HT-PEMFC electrodes, using H_3PO_4/D_3PO_4 contrast.[417]

QENS studies have been used to probe water dynamics in LT-PEMFCs, including investigations into water distribution in the catalyst layers.[418] QENS data allowed for the quantification of water molecules per sulphonic acid group of different types (immobile, slow and fast), as well as identifying the effect of temperature on the type of water molecules observed. Although there is minimal liquid water in operating HT-PEMFCs, QENS could still be a useful technique for understanding water dynamics, particularly during start-up/shutdown. Furthermore, QENS has been applied to the study of PA at different Pt-loadings of the catalyst layer of HT-PEMFCs, with results suggesting stronger trapping of PA at higher Pt-loadings.[419] QENS has also been applied to the study of proton motion in the membrane. Early QENS application to HT-PEMFC membranes compared the proton dynamics measured with QENS to conductivity studies, which showed diffusion processes occurring at a rate between PA doped in a PBI membrane and pure PA.[420] QENS has also been used to study proton diffusion in the membrane, with the extraction of fractal diffusion dimensions allowing for study and verification of diffusion processes across a broad range, from ps to ns.[408] The proton dynamics of PA from the solid to the molten state has been studied using QENS.[421] This application may be useful in studying the performance of HT-PEMFCs at sub-zero conditions during cold start-ups – an area which has received little attention to date.

6. Raman and infrared spectroscopy

6.1 Raman spectroscopy

Raman spectroscopy uses the inelastic scattering of light at a given wavelength to differentiate between chemical structures in samples. The peaks in the spectra are used to identify specific local bonding arrangements, allowing for detailed structure determination. Raman spectroscopy is a flexible, non-invasive analytical technique with micron spatial resolutions.[422] Raman spectroscopy in LT-PEMFC research has been used to investigate the chemical structure of catalyst and support materials,[423–425] analyse membrane degradation,[426] including the distinction between loss of sulphonic end groups and fluorinated backbone,[427] and determine membrane water content.[428] One benefit of Raman over infrared spectroscopy is that the spectra are not overwhelmed by the presence of liquid water. This has allowed for *in situ* studies of water transport in LT-PEMFCs.[429] A particular type of Raman spectroscopy, coherent anti-Stokes Raman scattering (CARS), can be used to investigate dynamic studies of water transport due to the higher intensity signal and faster time resolution.[430] One study used CARS spectroscopy and a bespoke cell design with a quartz window to investigate the hydration states of the membrane as a function of relative humidity and current density.[430]

Research in HT-PEMFCs share similarities due to similar components in the catalyst layer; for example, the technique has been used to investigate the structure of catalyst and carbon supports.[379,431,432] The structure of composite membranes has also been analysed in HT-PEMFC research.[274,433] Raman spectroscopy was used to study the effects of acid doping on PBI membranes as it is highly sensitive to the structural changes that occur during the acid–base proton exchange.[38] Also, Raman mapping has been used to determine the acid distribution as a function of the doping method.[434] *In situ*/*operando* studies using operating cells are not reported in the current literature, and there are only a small number of these studies for LT-PEMFCs. Studying the chemical structure in the membrane during operation at HT-PEMFCs conditions is a potentially useful yet challenging application of Raman spectroscopy that is yet to be demonstrated.

6.2 Infrared spectroscopy

Fourier Transform Infrared (FTIR) Spectroscopy uses the absorption and transmission of incident IR light to obtain information about the sample. The frequencies of light absorbed are related to the physical characteristics of the material. IR spectra can be obtained using a monochromatic beam which

Open Access Article. Published on 07 March 2024. Downloaded on 1/20/2026 7:35:49 PM. This article is licensed under a Creative Commons Attribution 3.0 Unported Licence.

changes in wavelength over time, or now more commonly, by using a Fourier transform instrument to measure a wide range of wavelengths at the same time. Software combined with the FTIR spectroscopy method can search through a large number of reference spectra to determine the identity of the substance under measurement.[435] FTIR spectroscopy has been used to investigate the acid-doping process similar to Raman spectroscopy.[436] The FTIR spectra showed evidence of an acid–base proton exchange reaction resulting in the formation of $H_2PO_4^-$ and protonated imidazolium cations. Fig. 20 shows the presence of $H_2PO_4^-$ (942 cm^{-1}) was clear at lower doping levels but became partially masked by the large amount of free H_3PO_4 (998 cm^{-1}) at high acid concentrations.[436] Other applications of FTIR spectroscopy in HT-PEMFC research include characterisation of acid groups in membranes,[99,437,438] characterisation of electrocatalysts,[438] and investigation of adsorption of PA onto Pt.[439] A cell design allowing for *in situ* FTIR measurements of an operating HT-PEMFC was used to measure the spectroscopic signature of adsorbed CO on the Pt surface as a function of temperature.[440] An FTIR gas spectrometer has been used to measure the CO_2 content in the cathode exhaust caused by carbon corrosion induced by simulated start-up/shutdown in a LT-PEMFC.[441] A similar study was conducted for an HT-PEMFC whereby the cell was subjected to 30 minutes at potentials of 0.9, 1.0, 1.1 and 1.2 V, and the CO_2 in the cathode exhaust gas was measured using an IR spectrometer.[442] The higher the potential, the greater the carbon corrosion and the more CO_2 was emitted. Operating at 160 °C and 1.2 V resulted in a peak CO_2 content of approximately 1600 ppm for a 100 cm^{-2} cell. The measurement of CO_2 in the exhaust using IR spectroscopy has also been utilised in determining the ECSA of an HT-PEMFC electrode and is deemed to be a reliable method.[306] Fig. 21 shows the IR spectra of PA–water mixtures. The broad

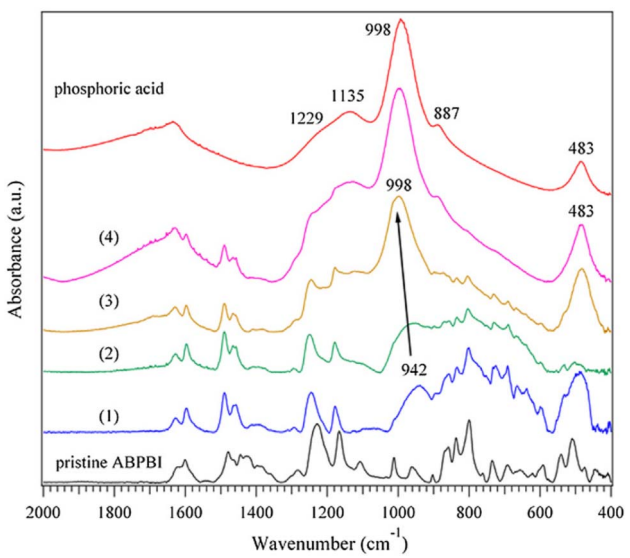

Fig. 20 FTIR spectra of pristine ABPBI, acid-doped ABPBI and phosphoric acid. Spectra numbered (1)–(4) correspond to ABPBI membranes with increase acid doping levels. Reprinted from ref. 436, Copyright (2014), with permission from Elsevier.

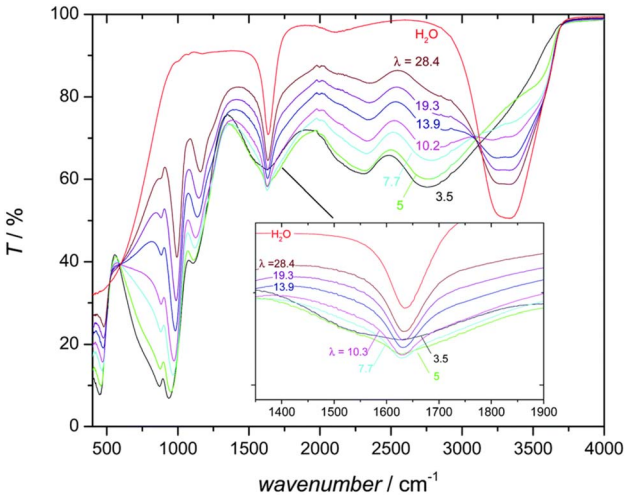

Fig. 21 IR spectra of water and PA–water mixtures as a function of water content, λ. Reprinted from ref. 92 with permission from the Royal Society of Chemistry.

intense absorption above 3000 cm^{-1} corresponds to the stretching vibration of OH involved in a hydrogen bond with the oxygen of another water molecule. This feature decreases with increasing PA content and disappears at a PA–water ratio of 1 : 1 ($\lambda = 5$). This was explained by water molecules being separated and only able to form hydrogen bonds with phosphate species.[92]

7. Optical and infrared imaging

7.1 Optical imaging

Transparent cells have been designed to investigate water flooding in LT-PEMFCs through direct visualisation of the water behaviour using charge-coupled device (CCD) digital cameras.[443–448] The transparent cells are comprised of the same components as a conventional PEMFC except that a window made from materials such as polycarbonate, acrylic, or plexiglass allows for optical observation inside the cell.[448] Careful consideration and design are required to minimise the difference in the performance of a typical PEMFC and a transparent PEMFC, important aspects include size and shape of the active area, uniform heating, and validation against typical PEMFC.[448] The technique is also limited due to the difficultly in quantifying water transport inside the cell which is not visible to the camera. This is where X-ray and neutron techniques provide advantages with greater penetration into the sample and visualisation of the cell interior. However, the advantages of transparent cells and optical imaging are that they provide high temporal and spatial resolutions, allow for *operando* experiments whilst being lower cost and are simpler and less hazardous.[447,449] Due to the high operating temperatures, visualisation of liquid water for HT-PEMFCs in this way is not as useful, other than during start-up or any operation below 100 °C. A possible application may be visualisation of PA since it is in liquid form at typical operating temperatures and leaches out to the GDL and bipolar plates. However, the quantities may be insufficient to make detection using this method practical or possible.

 This journal is © The Royal Society of Chemistry 2024

Open Access Article. Published on 07 March 2024. Downloaded on 1/20/2026 7:35:49 PM. This article is licensed under a Creative Commons Attribution 3.0 Unported Licence.

Optical fibres have gained interest and application as a sensor for PEMFCs. Optical fibre sensors have been used to detect temperature,[450] relative humidity,[450,451] membrane water content,[452] and species related to membrane degradation.[453,454] The application of optical fibres in HT-PEMFC is less common. One use has the fibres included as part of micro-electro-mechanical systems (MEMS) technology for detecting internal conditions such as temperature.[455] Optical fibres have been used as pH sensors,[456,457] which could be useful to infer acid distribution in HT-PEMFCs, but there are no studies applying optical fibres to sense PA in HT-PEMFCs to the best of our knowledge.

7.2 Infrared imaging

Infrared (IR) imaging, also known as infrared thermography, detects the infrared radiation emitted by an object and creates an image from which the temperature distribution can be inferred. IR thermography can be used in single-frame mode to take a snapshot of the system, or transient imaging can be used to image the system as a function of time.[458] Exothermic chemical reactions and ohmic heating in the fuel cell release heat energy and can be used for multiple types of analysis. One such type is to investigate fuel crossover, which can in turn be used to investigate membrane degradation. If the membrane is truly impermeable to the reactants, hydrogen and oxygen cannot react directly (as opposed to the electrochemical route required for fuel cell operation). However, low levels of fuel crossover do occur and this is increased by perforations forming in the membrane.[27] The direct reaction leads to local temperature hotspots where higher crossover is present, this enables the identification of pinhole size and location.[459] IR transparent windows have been used in LT-PEMFCs to investigate cathode and flow channel temperature distributions.[460,461] The presence of liquid water interferes with the IR radiation and temperature estimation becomes difficult.[462] However, water transport visualisation has been achieved using optical and IR imaging.[463] To the authors' knowledge, there are no reported studies using IR thermography combined with IR transparent windows in HT-PEMFC research. However, IR thermography has been used to detect the external stack temperature distribution.[464]

8. Gas and ion chromatography

8.1 Gas chromatography

Gas chromatography (GC) involves a sample being injected into the system and carried to a column by a carrier gas known as the mobile phase. Once in the column, the sample mixture interacts with the stationary phase (typically a liquid film) and is separated into its various components based on the time taken for the compound to progress through the column to the detector (retention time). GC is typically combined with a mass spectrometer (MS) to allow for the separation and analysis of trace elements of chemical species in the exhaust gas at the anode and cathode outlets.[20] GC has been used in LT-PEMFC research to investigate catalyst poisoning effects,[465–467] degradation products,[468] water distribution,[469] and gas crossover.[470–472]

GC requires a column to separate the gases prior to analysis. However, some columns may be suitable for certain gases *e.g.*, H_2 but not others *e.g.*, CO_2.[473] In some studies, gas is directed to the mass spectrometer without separation, and this is referred to as direct gas mass spectrometry (DGMS). This technique has been used to analyse degradation products such as HF, H_2O_2, CO_2, SO, SO_2, H_2SO_2, and H_2SO_3.[473,474]

There are only a couple of studies in the literature that use GC or DGMS to analyse HT-PEMFC exhaust gas.[190,475] Attention has focused on the CO_2 released at the anode during hydrogen starvation,[190,476] or ECSA calculation by monitoring CO_2 during CO stripping.[313] Another use of GC is to identify the concentration of gas species exiting a reformer and entering the HT-PEMFC.[477,478] One of the disadvantages of GC techniques is the relatively slow sampling time (min); therefore, real-time gas analysers using techniques such as DGMS which can provide faster sampling may be useful for more dynamic studies.[65]

8.2 Ion chromatography

Ion chromatography (IC) shares a similar process to GC whereby the sample is injected into a mobile phase (eluent) and enters the analytical column, here the ions in the sample adsorb onto a stationary phase (either anion or cation exchange resins). Ions with a higher affinity to the stationary phase will take longer to pass through the column and be detected and thus different ions are separated. IC is utilised more in HT-PEMFCs than GC. IC can be used to detect fluoride, sulphate, nitrate, and phosphate anions, as well as sodium and calcium cations.[479] IC has been used to determine the main PA degradation products in the fuel cell exhaust: PO_4^{3-} along with HPO_4^{2-}, $H_2PO_4^{-}$, and H_3PO_4.[147] Detection and quantification of phosphate ions are used to investigate PA content and loss in HT-PEMFCs.[147,149,208,212,363,479] Inductively coupled plasma mass spectrometry (ICP-MS) has also been used to quantify acid loss; here exhaust water is analysed and Pt loss can also be detected.[146,480] Several studies use the detection of HPO_4^{2-} to determine the loss rate of PA (H_3PO_4) by assuming all forms of PA are converted to HPO_4^{2-} due to the equilibrium associated with this tri-protic acid.[149,212] Across the studies it was generally found that increasing operating temperature, reactant flow rate, and current density led to faster PA loss and reduced durability, with the cathode loss typically higher than anode loss.[147,149,208,212] IC has also been used to investigate the effects of contaminated air on HT-PEMFC operation.[481,482] Sampling frequency in these studies is typically in the tens of hours or several days, meaning that highly dynamic studies of PA loss are unlikely to use IC.

IC has likewise been used in LT-PEMFC research to study degradation. Most commonly IC is used to detect fluoride and sulphate content of water samples which is indicative of membrane degradation.[483–485] Online measurements of fluoride ions from a PEM water electrolyser have also been made using IC; however, dynamic capability is limited by the sampling time, which in turn, was limited by the rinsing and recording time to 24 min.[486]

Open Access Article. Published on 07 March 2024. Downloaded on 1/20/2026 7:35:49 PM.
This article is licensed under a Creative Commons Attribution 3.0 Unported Licence.

9. Electron microscopy

9.1 Scanning electron microscopy

Scanning electron microscopy (SEM) is used for imaging structures and materials from the nm–μm range. This technique utilises a beam of electrons that is focused onto the surface of a sample, the interaction with the electron beam and the sample create several different types of electrons and X-rays, including secondary electrons and backscattered electrons. This allows for direct surface imaging across a wide variety of length scales depending on the exact magnification chosen. Most samples for LT- and HT-PEMFCs are either individual components (membranes, catalysts, support materials) or full MEAs (top surfaces, cross-section). Samples are typically deposited onto carbon tape and then coated with a thin layer of conductive materials (either gold or more typically carbon), to minimise sample charging. However, cross-sectional SEM samples typically require encasement in a resin followed by polishing, microtoming or freeze fracturing to ensure a flat sample.[487]

Focussed ion beam (FIB)-SEM is the most advanced preparation technique, in which an ion beam is used to mill the surface of the sample, creating a flat surface to image.[70,127,186,488,489] The FIB-SEM can be used to alternate between period of milling followed by imaging, thereby building a 3D image of the sample, which can in turn be used as a basis for 3D image-based modelling. The high resolution of SEM allows for the particle and pore structure of the MPL and catalyst layer to be imaged, which are beyond the typical resolution limit of other 3D imaging techniques like X-ray CT. Since the catalyst layers in LT- and HT-PEMFCs are similar, studies using FIB-SEM are largely similar for the two different technologies. For HT-PEMFCs, Prokop *et al.* used FIB-SEM to evaluate the 3D microstructure of catalyst layers,[490] and used the microstructures to model transport properties, with models showing good agreement with experimental studies.[491] Further modelling work has also used PEMFC catalyst layer datasets to generate deep-learning algorithms for accurate segmentation of FIB-SEM datasets, *i.e.*, ensuring the correct assignment of a label to each phase in the catalyst layer.[492] Finally, the morphology of different HT-PEMFC catalysts, including Pt/C and Pt_3Co/C, was studied using FIB-SEM, with analysis of the porosity showing that larger average pore size results in better acid distribution.[127]

SEM is also typically combined with energy-dispersive X-ray spectroscopy (EDX or EDS), which can measure and quantify the amounts of each element within the sample by collecting the characteristic X-rays of the element. EDX has been used in HT-PEMFC samples in conjunction with SEM imaging,[159,480,493] most interestingly it has been utilised to map the PA distribution within the structure of the catalyst layer (shown in Fig. 22).[168] SEM has also been widely used for qualitatively assessing the surface of the deposited material or layers; such as catalyst layer or membranes.[493–499] Cross-sectional SEM is a useful technique to assess membrane and electrode thickness, pore size distribution, catalyst location, catalyst layer structure and defects.[70,103,127,161,378,380,488,489,493–495,499–501] For HT-PEMFCs this has been shown to be useful for tracking acid loss out of the membrane *via* thickness changes.[380] Cross-sectional SEM has also been shown to significantly improve understanding of structural degradation during ASTs by observing the direct impact of the MEA thickness, pore structure, catalyst migration and support degradation.[122,124,125,127,186,488,489,496] While the experimental methods and analysis are very similar between LT- and HT-PEMFCs the differences in electrode composition, in particular the importance of PA in the catalyst layer, gives SEM an increased importance for HT-PEMFC compared to LT-PEMFC.

9.2 Transmission electron microscopy

Transmission electron microscopy (TEM) is a sample analysis technique that focuses a beam of electrons onto a sample, the electrons pass through the sample, interacting with it before reaching the detector behind the sample. TEM has high resolution; however, given the electron beam must pass through the sample, the materials have to be exceptionally thin. Samples are typically prepared *via* deposition onto specialised TEM grids, leaving clusters of materials no more than 10–100 nm thick. As a result of this preparation method this technique is only useful for imaging a small part of fuel cell materials, typically support materials, ionomer and most commonly catalysts.[493,498,502] TEM is often used to investigate catalyst characteristics due to the nano-scale resolution of this technique. Examples include catalyst particle size before and after cell reversal caused by air

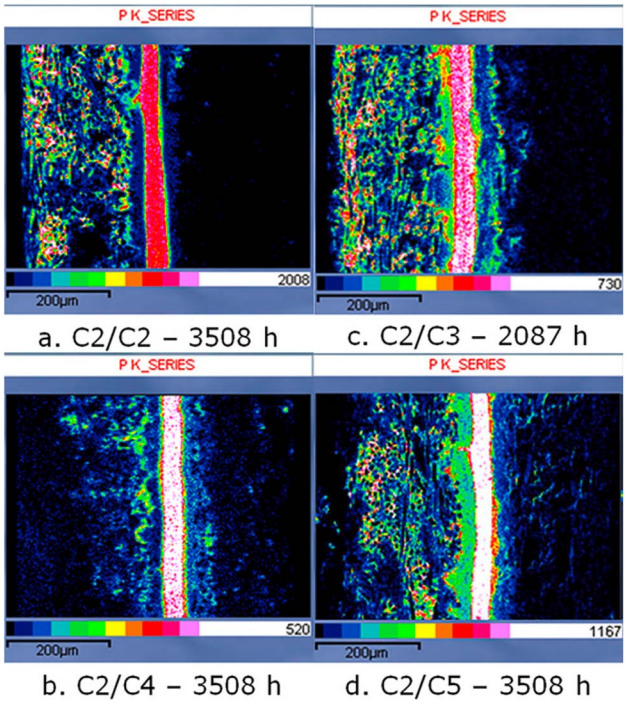

Fig. 22 Cross-sectional SEM images of HT-PEMFC MEAs with EDX mapping of phosphorous. The MEAs feature various anode/cathode GDL combinations imaged at the end of testing: (a) H23C2/H23C2, (b) H23C2/H23C4, (c) H23C2/H24C3, and (d) H23C2/H24C5. The distinct band in the centre is the membrane, with the anode and cathode on the left and right sides respectively. Reprinted from ref. 168, Copyright (2018), with permission from Wiley.

This journal is © The Royal Society of Chemistry 2024

Open Access Article. Published on 07 March 2024. Downloaded on 1/20/2026 7:35:49 PM. This article is licensed under a Creative Commons Attribution 3.0 Unported Licence.

and fuel starvation,[503,504] catalyst aggregation and surface area,[505] catalyst particle size and distribution.[506] TEM has also been applied to HT-PEMFCs to determine Pt particle size and size distribution.[120,162,192] There is little to no difference in sample preparation reported between LT and HT-PEMFCs, although, sample preparation typically involves sonication in water which is likely to significantly disrupt the PA distribution in HT-PEMFCs.

10. Magnetic resonance

10.1 Nuclear magnetic resonance

Nuclear Magnetic Resonance (NMR) is the absorption and reemission of radiofrequency (RF) pulses by nuclear spins in a magnetic field, or the responses of spins to external RF excitations.[507] NMR techniques can only probe nuclei with non-zero spins, essentially nuclei with odd number of protons and/or neutrons *e.g.*, ^{1}H, ^{2}H, ^{13}C, ^{19}F, ^{31}P, ^{195}Pt. There are many different techniques that use NMR such as solution-state, solid-state, pulsed-field gradient (PFG) and static-field gradient (SFG), relaxometry, and others. For a more in-depth review of different NMR techniques and applications to PEMFCs, the reader is referred to dedicated review articles.[507,508] NMR techniques are used in LT-PEMFCs to characterise structural properties, and proton and water transport properties. Membrane structural characterisation studies typically use NMR to target ^{1}H, ^{13}C, ^{19}F and ^{31}P nuclei, and can be used to identify structural changes caused by degradation.[507–509] Analysis of exhaust water following membrane degradation has utilised ^{19}F NMR.[510] Water and proton transport properties such as the water diffusion and electroosmotic drag coefficients have been investigated using NMR methods.[511–513] NMR has been used similarly in HT-PEMFCs, although focusing on proton transport in acid-doped membranes rather than water-saturated PFSA membranes. Proton conduction mechanisms in PA–water and PA–benzimidazole systems have been investigated using ^{1}H, ^{17}O and ^{31}P NMR spectroscopy.[92,93] The studies identified the changes in proton transport mechanism as a function of water content, as well as identifying the importance of hydrogen bond frustration and why PA-PBI are suited to HT-PEMFCs. ^{31}P NMR has also been used to examine the impact of water on the energetics of PA interaction with the membrane and suggest a new acid loss mechanism based on the change in PA cluster energy.[211] Fig. 23 shows the chemical peaks of ^{31}P NMR for hydrous and anhydrous PA-PBI and biphosphate-TMA systems. The chemical shift downfield indicates a higher cluster interaction energy. Adding water to PA-PBI significantly increases the interaction energy; whereas, only a minor increase occurs when adding water to the biphosphate-TMA system. The lower interaction energy of the PA-PBI system is used to explain the poorer PA retention when water is present in contrast to the QAP-based systems.[211]

10.2 Magnetic resonance imaging

Magnetic resonance imaging (MRI) is based on the principles of NMR, and is commonly used in medical applications, whereby magnetic field gradients enable for spatial reconstruction to form the image. MRI has been used for *in situ* water visualisation in LT-PEMFCs.[514–516] Local current density has also been measured using the shift in obtained NMR signal caused by the magnetic field of the local current density.[517] While MRI has benefits such as being non-invasive and compatible with operating fuel cells, it does face challenges regarding the fuel cell material,[518] being incompatible with ferromagnetic and paramagnetic materials. This means that the typical materials within the electrode are not suitable for MRI, and MRI-specific component designs are required to enable successful imaging.[507] Currently, there are no studies in the literature using MRI to study HT-PEMFCs. Other than requiring specialist equipment and cell componentry, the main reason is likely that the lack of liquid water to be visualised means there is little interest in using this technique. However, ^{31}P MRI is utilised in medical applications to noninvasively detect phosphorous-containing biological tissues.[519,520] It may therefore be theoretically possible to use ^{31}P MRI as a method to investigate PA distribution in HT-PEMFCs.

11. Accelerated stress tests

Accelerated stress tests (ASTs) are tests designed to replicate long-term operation, allowing characterisation of degradation in a controlled manner and estimation of durability. ASTs may also be referred to as accelerated durability/degradation tests (ADTs), and ageing tests.

11.1 Background on LT-PEMFC ASTs

Given the importance of durability testing and the relative maturity of LT-PEMFCs, multiple organisations have developed

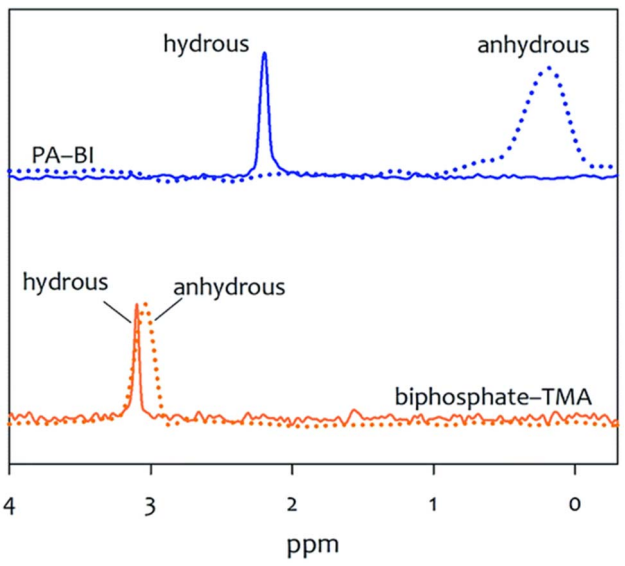

Fig. 23 ^{31}P NMR spectra comparison between hydrous and anhydrous PA-PBI and biphosphate-TMA. Hydrous conditions have water to PA ratio of 10. Reproduced from ref. 211 with permission from the Royal Society of Chemistry.

Open Access Article. Published on 07 March 2024. Downloaded on 1/20/2026 7:35:49 PM. This article is licensed under a Creative Commons Attribution 3.0 Unported Licence.

AST standards, including the U.S. DoE and those developed as part of the ID-FAST project funded by H2020.[521–523]

Chemical failure modes arise due to chemical attack on various components in the MEA and are most relevant for the membrane and the GDL. The main reason for the chemical degradation of the membrane is a result of the formation of hydrogen peroxide (H_2O_2) and subsequent breakdown to free-radicals (*e.g.*, ·OH, ·OOH and ·H);[524,525] these react with both side-chains and the polymer backbone in the PFSA membrane,[526] *via* a complex number of reactions that are discussed in detail by Coms.[525] It is thought that the presence of impurities, like Fe^{2+} or Cu^{2+}, accelerates the formation of free radicals in the membrane,[525] as shown by an OCV durability test.[527]

Hydrogen peroxide can also result in degradation of the GDL *via* oxidation.[528] To emulate this form of degradation, GDLs can be soaked in H_2O_2 for a number of hours, followed by performance testing and comparison of MEAs prepared with aged GDLs to those prepared with pristine GDLs. A range of conditions for GDL soaking are found in the literature: 35 wt% H_2O_2 for 12 h at 90 °C;[529] 30 wt% for 16 h or 24 h at 90 °C;[339,530] 30 wt% H_2O_2 for 15 h at 95 °C;[531] H_2O at 80 °C for 1000 h.[532] Despite differences in the degradation protocol used, the result of the immersion in most cases was found to be reduced fuel cell performance, along with increased water accumulation in the GDL.

Mechanical failure modes mostly affect the membrane (though carbon corrosion could be considered a mechanical failure mode of the catalyst layer due to the formation of cracks). Humidity cycling during MEA operation can cause the membrane to crack and pinholes can be formed.[362,533] This results in performance loss by way of gas crossover or significant inhomogeneity in current density distribution.[534,535] Furthermore, pinhole formation, in particular, is thought to be accelerated by way of combined chemical and mechanical degradation,[536] where gas crossover, growth of pinholes and side/main-chain degradation are all observed.[536,537]

Carbon corrosion is most likely to occur during start-up/shutdown of the fuel cell, where significant overpotentials arising as a result of an air/hydrogen boundary lead to oxidation of the carbon and gas formation in the form of carbon monoxide and carbon dioxide.[538,539] By cycling in a triangular-sweep profile between 1.0 and 1.5 V for 5000 cycles, the carbon support can be degraded. As well as the formation of gases, the morphology of the catalyst layer is significantly impacted, with the formation of cracks through the catalyst layer,[349,360] as well as the collapse of the electrode leading to reduced porosity.[540] Both effects increase the mass transport losses in the cell, since gas diffusion and water transport are inhibited in the CL and electron transport pathways are minimised due to the cracks.[541]

Electrocatalyst degradation occurs during operation over many thousands of hours, and the AST used to resemble this involves square-wave cycling between 0.6 and 0.95 V for 30 000 cycles. The voltage window relates to the activation region of the polarisation curve, where the performance of the fuel cell is limited most by electrocatalyst kinetics. Over the course of cycling, the Pt undergoes degradation *via* several key mechanisms, including agglomeration, Ostwald ripening and dissolution, as discussed by Meier *et al.*[542] Cyclic voltammetry is one of the key techniques for characterising and understanding the progress of degradation in the cycle, since CV allows for quantification of the ECSA and as the catalyst nanoparticles coalesce/agglomerate, their active surface area available for reaction decreases.[543] The electrocatalyst AST is particularly useful in the search for low- to non-Pt-containing electrocatalysts,[251] since the long-term stability of these can be measured using the AST. Other effects, like the particle size effect,[544] the use of alternative supports like carbon nanofibres,[545] tantalum-modified titanium oxide,[546] have been investigated using the electrocatalyst AST.

11.2 HT-PEMFC ASTs

A comprehensive list of ASTs for HT-PEMFCs is given in Table 4 and will be discussed in detail in this section. ASTs commonly focus on acid loss, catalyst degradation, and the effects of start-up/shutdown procedures.

11.2.1 Acid loss. PA can be lost from the cell through evaporation, electrolyte migration towards the anode, removal due to water which has entered the PA cluster, and during hot-pressing.[126,211,212] Therefore, acid loss is dependent on temperature and applied current density. Current has multiple effects, one being the migration of $H_2PO_4^-$ to the anode, and the other being the generation of water and subsequent interaction with PA and polymer membrane. This relationship is reflected in the types of ASTs used to induce acid loss. Current cycling from low current density to moderate or high current density is frequently used. Using higher maximum current densities during cycling leads to greater acid loss due to increased water generation, greater $H_2PO_4^-$ migration to the anode and removal through the flow field.[194,209] The high current density cycling protocol promoted by the group at the University of Oldenburg and developed in the Construction of Improved HT-PEM MEAs and Stacks for Long Term Stable Modular CHP Units (CISTEM) project (grant agreement ID: 325262) is shown in Fig. 24.[189] The results show higher phosphorous content detected in the fuel cell exhaust water when using higher current density cycling.

The length of time the cell is held at the current density set points also has an effect. Longer hold times lead to lower degradation rates; this was explained by more time at low current densities allowing for a greater amount of acid which had migrated into the electrodes to re-enter the membrane.[547] Multiple studies have reported using the same or very similar current cycling profiles; however, the test duration, gas supply parameters, and temperature are not consistent across all studies.[146,219,274,548,549] This makes it difficult to reliably compare MEA performance between different studies. Constant current or potential testing is reported in the literature with the former being more common for acid loss testing due to the dependence on water generation and therefore current rather than potential, but current cycling is used most and induces greater degradation rates.[146,550] Thermal cycling is also used to accelerate acid loss due to the impact of temperature on evaporation and the impact of water partial pressure changes occurring when

Open Access Article. Published on 07 March 2024. Downloaded on 1/20/2026 7:35:49 PM.
This article is licensed under a Creative Commons Attribution 3.0 Unported Licence.

Table 4 HT-PEMFC AST protocols in the literature

Type of stress	Cycle description	Temperature range	Gases supplied (anode//cathode)	Duration	Ref.
Acid loss					
Current cycling	0.60 A cm^{-2} (4 min) 1.00 A cm^{-2} (16 min) 0 A cm^{-2} (10 min every 6 h)	160 °C	H_2//air (dry)	70–230 h	146
Current cycling	0.60 A cm^{-2} (4 min) 1.00 A cm^{-2} (16 min) 0.00 A cm^{-2} (10 min every 6 h)	150 °C	H_2//O_2 (dry)	70 h	274 and 548
Current cycling	0.60 A cm^{-2} (4 min) 1.00 A cm^{-2} (16 min)	160 °C	H_2//air (unspecified)	500 h	219 and 549
Current cycling	0.20 A cm^{-2} 0.80 A cm^{-2} (20 min per cycle)	160 °C	H_2//air (unspecified)	600 h	194
Current cycling	0.20 A cm^{-2} (15–120 s hold times) 0.80 A cm^{-2} (21–168 s hold times)	160 °C	H_2//air (dry)	2000 h	547
Current cycling	0.20–0.60 A cm^{-2} (0.05 A cm^{-2} step every 5 min)	160 °C	H_2//air (unspecified)	100 h	186
Constant current	0.20 A cm^{-2}	190 °C	H_2//air (dry)	2830 h	212
Constant potential	0.20 V	150 °C	H_2//air (dry)	100 h	564
Thermal cycling	0.20 A cm^{-2}	140 °C (1 h) 160 °C (1 h) 180 °C (1 h)	H_2//air (unspecified)	100 h	186
Thermal cycling	0.15 A cm^{-2}	80–160 °C (10 °C min^{-1} ramp rate)	H_2//O_2 (p_{H_2O} = 9.7 kPa)	550 cycles	112
Catalyst layer degradation					
Potential cycling	0.60–1.00 V (0.05 mV s^{-1} scan rate)	160 °C	H_2//N_2 (dry)	10 000 cycles	123
Potential cycling	0.60 V (8 s) 1.00 V (8 s)	160 °C	H_2//N_2 (dry and wet N_2 tests)	30 000 cycles	125 and 156
Potential cycling	OCV (3 min) 0.50 V (30 s)	160 °C	H_2//air (unspecified)	100 h	281
Potential cycling	0.90 V (3 min) 0.50 V (3 min)	160 °C	H_2//air (dry)	5000 cycles	551
Potential cycling	0.60–1.20 V (0.05 mV s^{-1} scan rate)	160 °C	H_2//N_2 (dry)	5000 cycles	122
Current cycling	0.00 A cm^{-2} (20 min) 0.20 A cm^{-2} (20 min)	160 °C	H_2//air (dry)	100 h	480
Current cycling	0.0–0.2 A cm^{-2} (0.05 A cm^{-2} step every 5 min)	160 °C	H_2//air (unspecified)	100 h	186
Current cycling	0.04 A cm^{-2} 0.20 A cm^{-2} (20 min per cycle)	160 °C	H_2//air (unspecified)	600 h	194
Current cycling	0.00 A cm^{-2} (4 min) 0.30 A cm^{-2} (16 min)	160 °C	H_2//air (unspecified)	1000 h	550

Open Access Article. Published on 07 March 2024. Downloaded on 1/20/2026 7:35:49 PM.
This article is licensed under a Creative Commons Attribution 3.0 Unported Licence.

Table 4 (*Contd.*)

Type of stress	Cycle description	Temperature range	Gases supplied (anode//cathode)	Duration	Ref.
Bipolar plate degradation					
Potential cycling	0.10 V (15 min) 0.97 V (15 min)	120 °C	$H_2//O_2$ (unspecified)	83 h	142
Membrane degradation					
Temperature cycling	0.00 A cm^{-2}	30 °C (30 min) 180 °C (30 min)	Unspecified	150 h	557
Temperature cycling	0.6 V	40 °C (2 h) 160 °C (2 h)	Unspecified	2500 h	559
Start-up/shutdown					
Current and thermal cycling	0.00 A cm^{-2} (25 → 200 °C OCV stabilise) 0.60 A cm^{-2} (1 h at 200 °C) 0.00 A cm^{-2} (200 → 25 °C)	25–200 °C	$H_2/N_2//air/N_2$ (dry)	100 cycles	555
Potential cycling at constant temperature	1.0 V (5 min, fuel valves open) 0.10 V (5 min, cell off, valves closed) (0.025 mV min^{-1} scan rate)	−20 °C 15 °C 40 °C	$H_2//O_2$ (dry)	150 cycles	115
Thermal cycling at constant voltage	0.50 V	40–160 °C (15 °C min^{-1} ramp rate)	H_2//air (dry)	700 cycles	114
Current and thermal cycling	0.30 A cm^{-2} (approx. 12 h, 160 °C) 0.00 A cm^{-2} (approx. 12 h, ≤120 °C)	30–160 °C	$H_2/N_2//air/N_2$ (unspecified)	500 h	219
Current and thermal cycling	0.20 A cm^{-2} (16 h, 180 °C) 0.00 A cm^{-2} (approx. 8 h, 25 °C)	25–180 °C	H_2//air (dry)	157 cycles	252
Current and thermal cycling	0.00 A cm^{-2} (30 s, 115 °C) 0.25 A cm^{-2} (990 s, 165 °C) 0.03 A cm^{-2} (600 s, 25 °C)	80–165 °C (2.5 °C min^{-1} ramp rate)	H_2/reformate/N_2//air (dry)	1562 cycles	238
Fuel cycling	No load applied Anode gas switched between H_2 and air in 90 s intervals (air as cathode gas)	180 °C	H_2/air//air	150 cycles	252
Potential cycling	1.5 V (30 min)	160 °C	$H_2//N_2$ (100% RH)	2.5 h	565
Duty cycle					
Current cycling	Duty cycle based on new European drive cycle (NEDC)	160 °C	H_2//air	500 cycles	566
Current cycling	Annual CHP unit profile 0.40 A cm^{-2} (250 h) 0.20–0.40 A cm^{-2} (120 h) 0.20 A cm^{-2} (120 h) 0.00–0.20 A cm^{-2} (240 h) 0.20–0.40 A cm^{-2} (120 h) 0.20 A cm^{-2} (120 h)	160 °C	H_2/CO//air	970 h	567

This journal is © The Royal Society of Chemistry 2024

Open Access Article. Published on 07 March 2024. Downloaded on 1/20/2026 7:35:49 PM. This article is licensed under a Creative Commons Attribution 3.0 Unported Licence.

cycling with set points above and below phase change temperatures. Thermal cycling has been reported to cause more significant PA leaching than low or high load current cycling.[186] It is clear that ASTs, including high temperatures >180 °C and/or current density cycling with upper set points ≥0.6 A cm^{-2}, are effective and common methods to study acid loss in HT-PEMFCs. However, a standardised approach is lacking and is required to allow reliable comparisons across studies.

11.2.2 Catalyst degradation. The degradation of the catalyst layer can occur through several different mechanisms: carbon corrosion,[121,189,190] Pt dissolution, detachment, Ostwald ripening, sintering, and agglomeration.[156,189,191,192] As can be seen in Table 4, potential cycling is much more common for inducing catalyst layer degradation than acid loss. This is due to the established dependence of catalyst degradation mechanisms on potential. Carbon corrosion is typically targeted using cycling with upper limits >1.0 V, whereas Pt degradation mechanisms can be targeted with slightly lower limits ~0.9 V.[122,551,552] Potential cycling ASTs often operate with H_2 and N_2 supplied to the anode and cathode, respectively, to avoid superimposed currents caused by the oxidation of hydrogen interfering with corrosion current measurements.[156] Many AST studies targeting catalyst degradation in HT-PEMFCs use dry gases as would be typical in normal operation; however, unlike during operation, these ASTs result in no water at the cathode during cycling which has a significant effect on recorded degradation; humidified conditions can lead to irreversible degradation, whereas performance was reported to be recoverable after operating in dry conditions as the dehydration-restricted Pt dissolution mechanisms that require ion conductivity involve reaction with water.[156] This effect is shown in Fig. 25, where the difference in polarisation curves after 30 000 cycles with subsequent 24 hours of operation for both humidified and dry H_2/N_2 conditions can be seen.

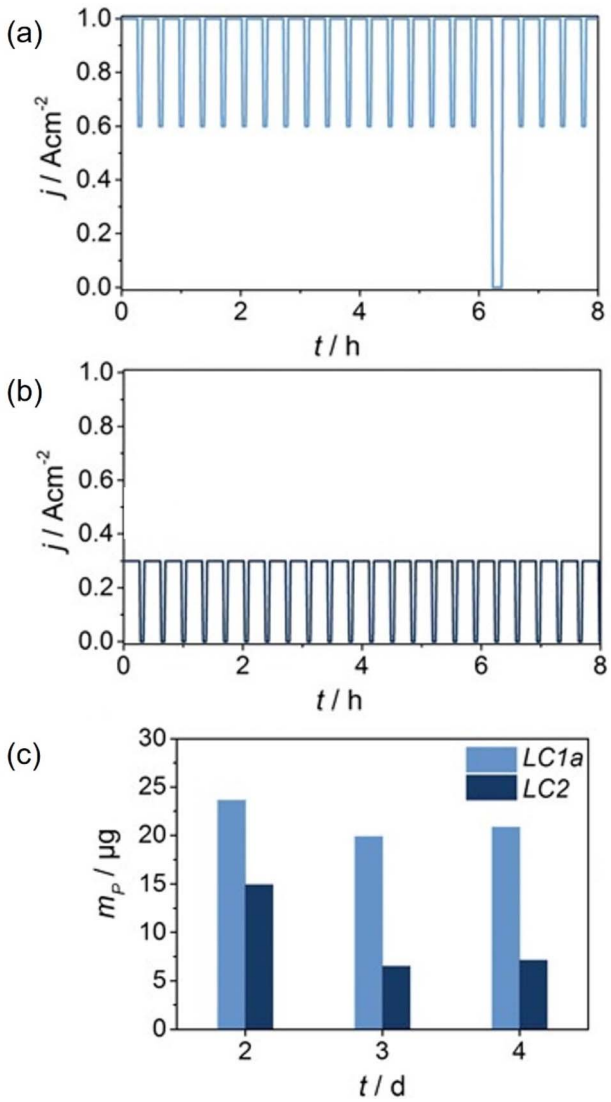

Fig. 24 AST profiles for inducing PA loss using (a) high (LC1a) and (b) low (LC2) current density cycling, and (c) mass of phosphorous in the fuel cell exhaust water determined by ICP-MS. Adapted from ref. 146, Copyright (2016), with permission from Wiley.

Triangular and square wave cycling is frequently used in catalyst layer degradation protocols. Other than the potential limits, triangular and square wave cycles are defined by their scan rate and hold times respectively. Generally, square wave ASTs lead to faster degradation rates due to rapid potential changes and longer hold times at high potential.[553,554] However, which type of wave used during AST cycling will accelerate degradation more depends on the conditions of the individual cycles.[552] Current cycling is also used to investigate catalyst degradation in HT-PEMFCs. These cycles are typically from 0.0 A cm^{-2} to 0.2 A cm^{-2} and are generally square waves with up to 20 min hold times. This type of cycling is more representative of real fuel cell operation as OCV and non-zero currents are used under hydrogen and air conditions. To the authors' knowledge there are currently no standards for ASTs targeting catalyst degradation in HT-PEMFCs. Studies do use established cycles used for LT-PEMFCs, and this is reasonable as the catalyst layer materials and structure shares many similarities with LT-PEMFCs. However, higher temperature operation, water in the vapour phase, the presence of PA, use of reformate gas, and different binder materials mean that catalyst degradation in HT-PEMFCs ultimately occurs under different conditions. Therefore, specific catalyst degradation AST protocols should be defined for HT-PEMFCs. It is also worth noting that AST studies of catalyst degradation in the literature typically run a predetermined number of cycles or duration, whereas acid loss studies may do this or run the cell until failure.

11.2.3 Start-up/shutdown. The start-up/shutdown event in PEMFCs can lead to air and fuel coexisting at the anode which causes high potentials at the cathode resulting in severe carbon corrosion.[250] Depending on the length of time since the fuel cell last operated, the change in temperature during the start-up/shutdown event could be >120 °C. Starting up the fuel cell or shutting it down would typically involve a step change in current either from or to 0 A cm^{-2}. Therefore, ASTs targeting the start-up/shutdown process could include high potential, thermal and current cycling. As this type of process is more complex than just inducing acid loss or catalyst degradation (and often causes these mechanisms to occur), these ASTs show the greatest

Open Access Article. Published on 07 March 2024. Downloaded on 1/20/2026 7:35:49 PM.
This article is licensed under a Creative Commons Attribution 3.0 Unported Licence.

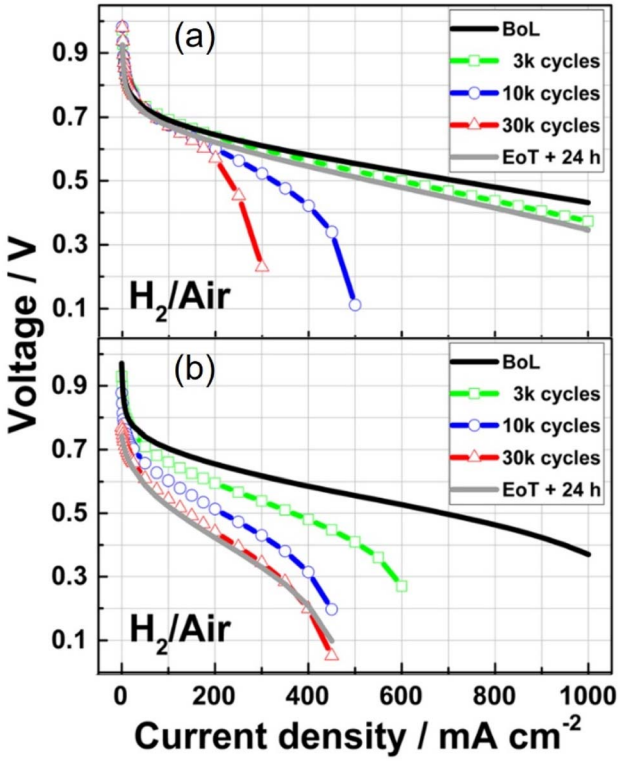

Fig. 25 Polarisation curves at beginning of life (BoL), after specified number of cycles, and end of test (EoT) with 24 hours of operation at 0.2 A cm^{-2}. (a) Dry and (b) humidified H_2/N_2 cycling between 0.6 and 1.0 V (graph modified from original).[156]

variation across studies. The duration of hold times at current or voltage set points range from 30 s to 16 h, where there are many cycles per day to increase degradation or one cycle per day which is more realistic of how frequently the fuel cells would be started up. Some of the studies purge the cell with N_2 during start-up and shutdown to prevent carbon corrosion or for safety,[219,238,555] while others do not purge with N_2 (or do not specify).[114,115,252] ASTs using thermal cycling have lower and upper temperature limits ranging from 25–80 °C and 160–200 °C, respectively, and some studies define temperature ramp rates while others do not. Very few studies investigate the impact of start-up and shutdown at temperatures below 0 °C.[115] Another study investigates the impact of H_2/air fronts in the anode by alternating gas flow between H_2 and air every 90 seconds with no load applied.[252] This method was deemed to be a realistic simulation of start-up/shutdown events compared to a 4000 h durability study with 157 start-up/shutdown cycles.[252] Due to the lack of standardisation of ASTs and the complexity of this process, reliable comparison of degradation rates between different studies in the literature is challenging. Standardisation of ASTs is the only way to reliably solve this issue. Attempts at standardising start-up/shutdown ASTs for LT-PEMFCs have been made by the U.S. DoE and H2020 European ID-FAST Project.[217,523,556] Adaptions to operating conditions of these existing protocols may provide a simple pathway to similar standardisation for HT-PEMFCs. However, specifically targeting acid loss during start-up/shutdown for degradation studies may require different protocols.

11.2.4 Other ASTs. ASTs targeting mechanisms other than acid loss, catalyst degradation and the start-up/shutdown process are much less common, likely because they are not deemed to be as crucial to durability. ASTs for membrane degradation found in the literature use thermal cycling to assess durability with lower and upper temperature limits of 30–40 °C and 160–180 °C respectively. The thermal cycling exposes the membrane to thermal and mechanical stress due to contraction and expansion of the membrane, and at low temperatures liquid water is formed and can contribute to acid loss.[557] At OCV conditions, reactants are not being consumed for electrochemical reaction which can result in higher crossover. The crossover of oxygen to the anode can result in the formation of hydrogen peroxide and subsequent radicals that chemically attack the membrane.[558] This is a problem for LT-PEMFCs, and cross-linked PBI showed similar susceptibility to Nafion membranes, with pristine PBI being even more susceptible.[559] ASTs have been developed for LT-PEMFCs to assess chemical stability.[560,561] The equivalent does not currently exist for HT-PEMFCs, although adaption of the LT-PEMFC protocols should be relatively straightforward. Chemical durability is typically assessed using Fenton's reagent tests.[562]

Research focusing on bipolar plate degradation and durability in HT-PEMFCs is relatively low.[563] ASTs for HT-PEMFC bipolar plates are even rarer. Only one AST was found in the literature. The study itself did not solely focus on bipolar plate degradation, but instead assessed the effects of potential cycling on both the MEA and bipolar plates.[142] Therefore, ASTs for HT-PEMFC bipolar plates are still lacking.

11.3 Summary of recommendations

Due to the importance of ASTs in allowing for controlled inducement of degradation mechanisms and estimation of lifetime, focus must be given to the development and standardisation of ASTs for HT-PEMFCs. Recommendations from this review include:

- Standardisation of acid loss ASTs. These should use high current density cycling with upper set points ≥0.6 A cm^{-2}, higher temperatures (>180 °C) may also be combined with the current density cycling to induce acid loss. However, the expected operating temperature of the fuel cell should be considered when estimating lifetime, with many PBI-based MEAs operating at 160 °C.
- ASTs targeting catalyst layer degradation (*e.g.*, carbon corrosion, catalyst surface area loss) can be adapted from standardised LT-PEMFC ASTs such as those generated by the U.S. DoE. However, the difference in operating conditions must be factored in when making adaptions to existing LT-PEMFC ASTs (*e.g.*, higher temperature, and dry reactant gases). The impact of the presence of water during potential cycling using N_2 on degradation and lifetime estimation should also be considered.
- Start-up/shutdown ASTs are the most complex with significant variation, and also require standardisation.

 This journal is © The Royal Society of Chemistry 2024

Open Access Article. Published on 07 March 2024. Downloaded on 1/20/2026 7:35:49 PM. This article is licensed under a Creative Commons Attribution 3.0 Unported Licence.

Adaption of existing protocols such as the U.S. DoE AST for LT-PEMFC start-up/shutdown may be a relatively simple pathway to achieving improved standardisation, as only the operating conditions would need to be altered. However, targeting specific HT-PEMFC degradation mechanisms during start-up/shutdown such as acid loss may require additional protocol adaption.

• ASTs for other components and degradation mechanisms have received less attention and require more development before standardisation can be achieved.

• Whilst adaptions to existing LT-PEMFC AST protocols may hasten standardisation of HT-PEMFC ASTs, it is not sufficient to cover all degradation mechanisms that are unique to HT-PEMFCs. Therefore, efforts should be made to build on the work of the DENMEA (grant agreement ID: 245156) and CISTEM projects with similar efforts to those of LT-PEMFC AST development (*e.g.*, H2020 European ID-FAST Project, U.S. DoE) to develop standardised ASTs for HT-PEMFCs.

12. Summary and concluding remarks

HT-PEMFCs offer multiple potential benefits over conventional LT-PEMFCs including higher impurity tolerance, simplified water and thermal management as well as potentially faster reaction kinetics. The recent development of PA-based ion-pair membranes for high-temperature operation offers significant improvements in performance across a wide temperature range, and improved PA retention in the presence of water. However, state-of-the-art performance and durability of HT-PEMFCs do not match that of commercial LT-PEMFCs. Additionally, the Pt loading is significantly higher for HT-PEMFCs. Thus, further work is required to address these issues.

This review introduced HT-PEMFC technology, the applications and important considerations of common characterisation techniques, how this differed from LT-PEMFCs, and highlighted areas required to advance characterisation and progress HT-PEMFC technology to commercialisation. Key conclusions and future directions are summarised below:

(1) *Operando* and *in situ* characterisation techniques are required to provide information about the fuel cell under realistic operating conditions. Methods that are non-destructive and allow the fuel cell to operate as it would in real-world applications require fewer assumptions and caveats when analysing the results, and therefore are the most useful. While there are *operando* and *in situ* techniques applied currently, the existing mature application of techniques to LT-PEMFCs may provide useful insight for further development and opportunities for HT-PEMFCs.

(2) Electrochemical characterisation techniques are essential for *operando* characterisation of HT-PEMFC performance. These characterisation methods share many similarities in their application with LT-PEMFCs, and the differences mainly occur in the results and their interpretation. The greatly reduced sensitivity to proton conduction *via* water molecules appears to lead to a reduction in hysteresis behaviour during polarisation curves, and the low-frequency inductance loop commonly found in LT-PEMFC EIS is scarcely reported. Further research is required to determine the extent to which these phenomena occur across operating conditions and to conclusively determine the impact of low-frequency inductive behaviour for HT-PEMFCs, and thus inform more accurate ECMs. The importance of linear EIS validity is also highlighted, especially when using DRT analysis which requires high-quality, valid data to allow meaningful interpretation. CV methods using the hydrogen underpotential method to determine ECSA may not be accurate for HT-PEMFCs, and CO stripping may be a better alternative.

(3) Imaging techniques such as X-ray and neutron radiography and CT, and optical and MRI imaging are commonly used in LT-PEMFCs to visualise water content and some offer similar applicability in characterising PA distribution in HT-PEMFCs. X-ray and neutron tomography techniques permit 3D and 4D *in situ* and *operando* studies providing useful information on the fuel cell morphology and dynamic transport of water and PA. Challenges arise with these techniques due to limited access to synchrotron facilities. Although X-ray radiography and CT are possible using lab-based systems, lab-based studies typically require a subtraction method to allow segmentation of the PA which necessitates time-consuming additional experimental and image processing steps. This ultimately limits the scope for *in situ* or *operando* studies where morphology changes prevent subtraction or preliminary "dry" scans are not possible. Therefore, new methods to improve PA segmentation by enhancing contrast would simplify existing PA visualisation methodologies.

(4) Non-invasive *operando* measurement of exhaust gases or analysis of effluent water can provide information on degradation. Gas and ion chromatography techniques are typically used for this purpose, with the latter most common for determining PA loss in HT-PEMFCs. These techniques offer the potential to monitor various degradation mechanisms such as carbon corrosion, membrane degradation, and PA loss; ICP-MS can also be used to identify trace elements such as Pt in effluent water. Current methods require long sampling times or for the sample to be collected and analysed *ex situ*. Development of techniques or methodologies with short sampling times (seconds to a couple of minutes) would allow for non-invasive dynamic studies of degradation as a function of operating conditions.

(5) Raman and IR spectroscopy are used to characterise the structure of catalyst layers and membranes in HT-PEMFCs. Raman spectroscopy has the advantage of high sensitivity even in the presence of liquid water, and this has allowed for dynamic studies of water transport in LT-PEMFCs. *Operando* studies of PA transport in HT-PEMFCs could offer insight into the chemical states of the acid-doped membrane. IR spectroscopy allows for *in situ* and *operando* studies of HT-PEMFC exhaust gases, often focusing on CO_2 caused by corrosion. NMR spectroscopy has been useful in probing the water and proton transport properties in LT-PEMFCs and has been applied similarly in PA-based systems in HT-PEMFCs; this has allowed a new PA loss mechanism to be suggested and insights into the success of PA-PBI systems and the improved PA retention of ion-pair membranes.

Open Access Article. Published on 07 March 2024. Downloaded on 1/20/2026 7:35:49 PM. This article is licensed under a Creative Commons Attribution 3.0 Unported Licence.

(6) ASTs are crucial for estimating real-world durability in a controlled lab-based setting. When combined with advanced characterisation techniques, ASTs are valuable in targeting specific degradation mechanisms, which ultimately assists the progress towards increased durability. Standardised ASTs for HT-PEMFCs are lacking, making meaningful durability comparisons between different studies impossible. Modifying existing standardised ASTs for LT-PEMFCs may be a potential remedy for this issue, an example being the adjustment of existing ASTs (*e.g.*, U.S. DoE) targeting catalyst degradation as the technologies share similar catalyst and support componentry. Careful consideration must also be given to the humidification state of the inlet gas in common catalyst layer ASTs. This parameter varies across tests and has been shown to have a significant impact on the degradation and representation of real-world operation. Unique mechanisms such as PA loss require new protocols. The most effective existing ASTs for inducing PA loss use high current density cycling (upper set point $\geq$0.6 A cm^{-2}), yet standardisation across studies is missing. The presence of PA must also be considered when designing new ASTs for components such as bipolar plates. Start-up/shutdown ASTs show considerable variation between studies, likely due to the complex nature of the process and the number of parameters involved. The initial and final temperatures, ramp rate, gases supplied, current and voltage cycling all vary significantly and have a critical impact on degradation, making it difficult to draw comparisons across studies and highlighting the need for standardisation.

The progression of HT-PEMFC technology to commercialisation relies on the utilisation of existing characterisation techniques as well as the development of new methodologies. A combination of electrochemical, multi-scale imaging, and spectroscopic techniques under fuel cell operating conditions is required for a deeper understanding of underlying physical and chemical mechanisms as well as the characterisation of performance, degradation and durability of cells and stacks. Another key takeaway is the identification of standardised ASTs as an essential next step to allow comparisons of technologies across studies.

Author contributions

Adam Zucconi: conceptualisation, investigation, project administration, visualisation, writing – original draft, writing – review & editing. Jennifer Hack: investigation, writing – original draft, writing – review & editing. Richard Stocker: writing – review & editing. Theo A. M. Suter: investigation, writing – original draft. Alexander J. E. Rettie: writing – review & editing. Dan J. L. Brett: writing – review & editing.

Conflicts of interest

There are no conflicts to declare.

Acknowledgements

AZ acknowledges funding support from HORIBA MIRA. JH acknowledges The Royal Academy of Engineering under the Research Fellowship programme and funding from EPSRC (EP/T517793/1) and the Faraday Institution (FIRG014 and FIRG058). DB acknowledges The Royal Academy of Engineering, the National Physical Laboratory and HORIBA MIRA for sponsoring his Research Chair in Metrology for Electrochemical Propulsion, and the authors are grateful for to EPSRC for sponsoring hydrogen research in the Electrochemical Innovation Lab (EP/X023656/1, EP/W03395X/1, EP/W033321/1, EP/S018204/2).

References

1 R. Turconi, A. Boldrin and T. Astrup, *Renewable Sustainable Energy Rev.*, 2013, **28**, 555–565.
2 M. A. Mac Kinnon, J. Brouwer and S. Samuelsen, *Prog. Energy Combust. Sci.*, 2018, **64**, 62–92.
3 G. Wang, J. Deng, Y. Zhang, Q. Zhang, L. Duan, J. Hao and J. Jiang, *Sci. Total Environ.*, 2020, **741**, 140326.
4 I. Hanif, S. M. Faraz Raza, P. Gago-de-Santos and Q. Abbas, *Energy*, 2019, **171**, 493–501.
5 L. Jamel and A. Derbali, *Cogent Econ. Finance*, 2016, **4**, 1170653.
6 E. Rasoulinezhad, F. Taghizadeh-Hesary and F. Taghizadeh-Hesary, *Energies*, 2020, **13**, 2255.
7 A. Rehman, A. Rauf, M. Ahmad, A. A. Chandio and Z. Deyuan, *Environ. Sci. Pollut. Res.*, 2019, **26**, 21760–21773.
8 F. Perera, *Int. J. Environ. Res. Public Health*, 2017, **15**, 16.
9 S. Shafiee and E. Topal, *Appl. Energy*, 2010, **87**, 988–1000.
10 C. Day and G. Day, *Econ. Model.*, 2017, **63**, 153–160.
11 IEA, *World Energy Outlook 2022*, 2022.
12 M. D. Delis, K. de Greiff and S. R. G. Ongena, *EBRD Working Paper No. 231*, 2019, DOI: **10.2139/ssrn.3451335**, **https://ssrn.com/abstract=3451335**.
13 World Bank, *State and Trends of Carbon Pricing 2021*, The World Bank, Washington, DC, 2021.
14 IEA, Renewables Information 2022**https://www.iea.org/data-and-statistics/data-tools/energy-statistics-data-browser?country=WORLD&fuel=Energysupply&indicator=RenewGenBySource**, accessed 7 June 2023.
15 R. Zhang and S. Fujimori, *Environ. Res. Lett.*, 2020, **15**, 034019.
16 N. Rietmann, B. Hügler and T. Lieven, *J. Cleaner Prod.*, 2020, **261**, 121038.
17 T. Wilberforce, Z. El-Hassan, F. N. Khatib, A. Al Makky, A. Baroutaji, J. G. Carton and A. G. Olabi, *Int. J. Hydrogen Energy*, 2017, **42**, 25695–25734.
18 S. J. Peighambardoust, S. Rowshanzamir and M. Amjadi, *Review of the Proton Exchange Membranes for Fuel Cell Applications*, Elsevier Ltd, 2010, vol. 35.
19 I. Staffell, D. Scamman, A. Velazquez Abad, P. Balcombe, P. E. Dodds, P. Ekins, N. Shah and K. R. Ward, *Energy Environ. Sci.*, 2019, **12**, 463–491.
20 G. Hinds, *Curr. Opin. Electrochem.*, 2017, **5**, 11–19.
21 ERM, *The Fuel Cell Industry Review 2022*, 2024.
22 R. E. Rosli, A. B. Sulong, W. R. W. Daud, M. A. Zulkifley, T. Husaini, M. I. Rosli, E. H. Majlan and M. A. Haque, *Int. J. Hydrogen Energy*, 2017, **42**, 9293–9314.

 This journal is © The Royal Society of Chemistry 2024

Open Access Article. Published on 07 March 2024. Downloaded on 1/20/2026 7:35:49 PM. This article is licensed under a Creative Commons Attribution 3.0 Unported Licence.

23 T. Xiao, R. Wang, Z. Chang, Z. Fang, Z. Zhu and C. Xu, *Prog. Nat. Sci.: Mater. Int.*, 2020, **30**, 743–750.
24 G. Li, W. Kujawski and E. Rynkowska, *Rev. Chem. Eng.*, 2020, 87–100.
25 T. Myles, L. Bonville and R. Maric, *Catalysts*, 2017, **7**, 16.
26 J. O. Jensen, H. A. Hjuler, D. Aili and Q. Li, in *High Temperature Polymer Electrolyte Membrane Fuel Cells*, ed. Q. Li, D. Aili, H. A. Hjuler and J. O. Jensen, Springer International Publishing, Cham, 2016, pp. 1–4.
27 R. Borup, J. Meyers, B. Pivovar, Y. S. Kim, R. Mukundan, N. Garland, D. Myers, M. Wilson, F. Garzon, D. Wood, P. Zelenay, K. More, K. Stroh, T. Zawodzinski, J. Boncella, J. E. McGrath, M. Inaba, K. Miyatake, M. Hori, K. Ota, Z. Ogumi, S. Miyata, A. Nishikata, Z. Siroma, Y. Uchimoto, K. Yasuda, K. I. Kimijima and N. Iwashita, *Chem. Rev.*, 2007, **107**, 3904–3951.
28 J. Tjønnås, F. Zenith, I. J. Halvorsen, M. Klages and J. Scholta, *IFAC-PapersOnLine*, 2016, vol. 49, pp. 302–307.
29 S. Simon Araya, F. Zhou, S. Lennart Sahlin, S. Thomas, C. Jeppesen and S. Knudsen Kær, *Energies*, 2019, **12**, 152.
30 M. Boaventura, H. Sander, K. A. Friedrich and A. Mendes, *Electrochim. Acta*, 2011, **56**, 9467–9475.
31 B. Shabani, M. Hafttananian, S. Khamani, A. Ramiar and A. A. Ranjbar, *J. Power Sources*, 2019, **427**, 21–48.
32 H. P. Dhar, L. G. Christner and A. K. Kush, *J. Electrochem. Soc.*, 1987, **134**, 3021–3026.
33 Q. Li, R. He, J.-A. Gao, J. O. Jensen and N. J. Bjerrum, *J. Electrochem. Soc.*, 2003, **150**, A1599.
34 S. K. Das, A. Reis and K. J. Berry, *J. Power Sources*, 2009, **193**, 691–698.
35 V. B. Venkatesh, G. Varghese, T. V. Joseph and P. Chippar, *Int. J. Hydrogen Energy*, 2021, **46**, 8179–8196.
36 C. Song, Y. Tang, J. L. Zhang, J. Zhang, H. Wang, J. Shen, S. McDermid, J. Li and P. Kozak, *Electrochim. Acta*, 2007, **52**, 2552–2561.
37 J. Zhang, Y. Tang, C. Song and J. Zhang, *J. Power Sources*, 2007, **172**, 163–171.
38 R. Zeis, *Beilstein J. Nanotechnol.*, 2015, **6**, 68–83.
39 R. Sur, T. J. Boucher, M. W. Renfro and B. M. Cetegen, *J. Electrochem. Soc.*, 2010, **157**, B45.
40 J. P. Owejan, J. E. Owejan, W. Gu, T. A. Trabold, T. W. Tighe and M. F. Mathias, *J. Electrochem. Soc.*, 2010, **157**, B1456.
41 J. M. LaManna and S. G. Kandlikar, *Int. J. Hydrogen Energy*, 2011, **36**, 5021–5029.
42 Y. Wu, J. I. S. Cho, M. Whiteley, L. Rasha, T. P. Neville, R. Ziesche, R. Xu, R. Owen, N. Kulkarni, J. Hack, M. Maier, N. Kardjilov, H. Markötter, I. Manke, F. R. Wang, P. R. Shearing and D. J. L. Brett, *Int. J. Hydrogen Energy*, 2020, **45**, 2195–2205.
43 L. Liu, W. Chen and Y. Li, *J. Membr. Sci.*, 2016, **504**, 1–9.
44 S. Deabate, G. Gebel, P. Huguet, A. Morin and G. Pourcelly, *Energy Environ. Sci.*, 2012, **5**, 8824.
45 I. A. Schneider, D. Kramer, A. Wokaun and G. G. Scherer, *Electrochem. Commun.*, 2005, **7**, 1393–1397.
46 X. D. Wang, Y. Y. Duan, W. M. Yan and F. B. Weng, *J. Power Sources*, 2008, **176**, 247–258.
47 S. S. Araya, F. Zhou, V. Liso, S. L. Sahlin, J. R. Vang, S. Thomas, X. Gao, C. Jeppesen and S. K. Kær, *Int. J. Hydrogen Energy*, 2016, **41**, 21310–21344.
48 P. Xiao, J. Li, H. Tang, Z. Wang and M. Pan, *J. Membr. Sci.*, 2013, **442**, 65–71.
49 S. H. Woo, A. Taguet, B. Otazaghine, A. Mosdale, A. Rigacci and C. Beauger, *Electrochim. Acta*, 2019, **319**, 933–946.
50 A. Chandan, M. Hattenberger, A. El-Kharouf, S. Du, A. Dhir, V. Self, B. G. Pollet, A. Ingram and W. Bujalski, *J. Power Sources*, 2013, **231**, 264–278.
51 L. Lüke, H. Janßen, M. Kvesić, W. Lehnert and D. Stolten, *Int. J. Hydrogen Energy*, 2012, **37**, 9171–9181.
52 J. Zhang, Z. Xie, J. Zhang, Y. Tang, C. Song, T. Navessin, Z. Shi, D. Song, H. Wang, D. P. Wilkinson, Z. S. Liu and S. Holdcroft, *J. Power Sources*, 2006, **160**, 872–891.
53 D. Aili, D. Henkensmeier, S. Martin, B. Singh, Y. Hu, J. O. Jensen, L. N. Cleemann and Q. Li, *Electrochem. Energy Rev.*, 2020, **3**, 793–845.
54 J. Zhang, D. Aili, S. Lu, Q. Li and S. P. Jiang, *Research*, 2020, **2020**, 1–15.
55 J. Jung, J. Ku, Y. S. Park, C.-H. Ahn, J.-H. Lee, S. S. Hwang and A. S. Lee, *Polym. Rev.*, 2022, 1–37.
56 E. Quartarone, S. Angioni and P. Mustarelli, *Materials*, 2017, **10**, 687.
57 X. Sun, S. Simonsen, T. Norby and A. Chatzitakis, *Membranes*, 2019, **9**, 83.
58 M. Ebrahimi, W. Kujawski, K. Fatyeyeva and J. Kujawa, *Int. J. Mol. Sci.*, 2021, **22**, 5430.
59 A. C. Dupuis, *Prog. Mater. Sci.*, 2011, **56**, 289–327.
60 N. P. Chikhaliya, Y. J. Rathwa and T. Likhariya, *High Perform. Polym.*, 2021, **33**, 998–1011.
61 S. Subianto, *Polym. Int.*, 2014, **63**, 1134–1144.
62 S. Bose, T. Kuila, T. X. H. Nguyen, N. H. Kim, K. Lau and J. H. Lee, *Prog. Polym. Sci.*, 2011, **36**, 813–843.
63 Z. Guo, M. Perez-Page, J. Chen, Z. Ji and S. M. Holmes, *J. Energy Chem.*, 2021, **63**, 393–429.
64 A. E. Russell and A. Rose, *Chem. Rev.*, 2004, **104**, 4613–4635.
65 J. Wu, X. Zi Yuan, H. Wang, M. Blanco, J. J. Martin and J. Zhang, *Int. J. Hydrogen Energy*, 2008, **33**, 1747–1757.
66 Q. Meyer, Y. Zeng and C. Zhao, *Adv. Mater.*, 2019, **31**, 1–25.
67 R. Haider, Y. Wen, Z.-F. Ma, D. P. Wilkinson, L. Zhang, X. Yuan, S. Song and J. Zhang, *Chem. Soc. Rev.*, 2021, **50**, 1138–1187.
68 S. Chevalier, M. Fazeli, F. Mack, S. Galbiati, I. Manke, A. Bazylak and R. Zeis, *Electrochim. Acta*, 2016, **212**, 187–194.
69 N. Bevilacqua, M. G. George, S. Galbiati, A. Bazylak and R. Zeis, *Electrochim. Acta*, 2017, **257**, 89–98.
70 F. Mack, M. Klages, J. Scholta, L. Jörissen, T. Morawietz, R. Hiesgen, D. Kramer and R. Zeis, *J. Power Sources*, 2014, **255**, 431–438.
71 L. Xia, M. Ni, Q. He, Q. Xu and C. Cheng, *Appl. Energy*, 2021, **300**, 117357.
72 P. O. Olapade, J. P. Meyers, R. L. Borup and R. Mukundan, *J. Electrochem. Soc.*, 2011, **158**, B639.

Open Access Article. Published on 07 March 2024. Downloaded on 1/20/2026 7:35:49 PM. This article is licensed under a Creative Commons Attribution 3.0 Unported Licence.

73 E. Carcadea, M. Varlam, M. Ismail, D. B. Ingham, A. Marinoiu, M. Raceanu, C. Jianu, L. Patularu and D. Ion-Ebrasu, *Int. J. Hydrogen Energy*, 2020, **45**, 7968–7980.
74 L. Xing, Y. Wang, P. K. Das, K. Scott and W. Shi, *Chem. Eng. Sci.*, 2018, **192**, 699–713.
75 L. Karpenko-Jereb, C. Sternig, C. Fink, V. Hacker, A. Theiler and R. Tatschl, *J. Power Sources*, 2015, **297**, 329–343.
76 A. Ozden, S. Shahgaldi, X. Li and F. Hamdullahpur, *Prog. Energy Combust. Sci.*, 2019, **74**, 50–102.
77 G. Lin and T. Van Nguyen, *J. Electrochem. Soc.*, 2005, **152**, A1942.
78 J. H. Chun, K. T. Park, D. H. Jo, S. G. Kim and S. H. Kim, *Int. J. Hydrogen Energy*, 2011, **36**, 1837–1845.
79 Y. Wang, B. Seo, B. Wang, N. Zamel, K. Jiao and X. C. Adroher, *Energy AI*, 2020, **1**, 100014.
80 Y. Chang, Y. Qin, Y. Yin, J. Zhang and X. Li, *Appl. Energy*, 2018, **230**, 643–662.
81 A. Ibrahim, O. Hossain, J. Chaggar, R. Steinberger-Wilckens and A. El-Kharouf, *Int. J. Hydrogen Energy*, 2020, **45**, 5526–5534.
82 Z. Jie, T. Haolin and P. Mu, *J. Membr. Sci.*, 2008, **312**, 41–47.
83 D. C. Lee, H. N. Yang, S. H. Park and W. J. Kim, *J. Membr. Sci.*, 2014, **452**, 20–28.
84 M. Amjadi, S. Rowshanzamir, S. J. Peighambardoust, M. G. Hosseini and M. H. Eikani, *Int. J. Hydrogen Energy*, 2010, **35**, 9252–9260.
85 E. Chalkova, M. B. Pague, M. V. Fedkin, D. J. Wesolowski and S. N. Lvov, *J. Electrochem. Soc.*, 2005, **152**, A1035.
86 K. T. Park, U. H. Jung, D. W. Choi, K. Chun, H. M. Lee and S. H. Kim, *J. Power Sources*, 2008, **177**, 247–253.
87 Y. Zhai, H. Zhang, J. Hu and B. Yi, *J. Membr. Sci.*, 2006, **280**, 148–155.
88 K. T. Adjemian, R. Dominey, L. Krishnan, H. Ota, P. Majsztrik, T. Zhang, J. Mann, B. Kirby, L. Gatto, M. Velo-Simpson, J. Leahy, S. Srinivasan, J. B. Benziger and A. B. Bocarsly, *Chem. Mater.*, 2006, **18**, 2238–2248.
89 J. Yang, D. Aili, Q. Li, Y. Xu, P. Liu, Q. Che, J. O. Jensen, N. J. Bjerrum and R. He, *Polym. Chem.*, 2013, **4**, 4768.
90 J. Yang, J. Wang, C. Liu, L. Gao, Y. Xu, Q. Che and R. He, *J. Membr. Sci.*, 2015, **493**, 80–87.
91 Y. Oono, A. Sounai and M. Hori, *J. Power Sources*, 2009, **189**, 943–949.
92 J.-P. Melchior, K.-D. Kreuer and J. Maier, *Phys. Chem. Chem. Phys.*, 2017, **19**, 587–600.
93 J. P. Melchior, G. Majer and K. D. Kreuer, *Phys. Chem. Chem. Phys.*, 2017, **19**, 601–612.
94 N. Üregen, K. Pehlivanoğlu, Y. Özdemir and Y. Devrim, *Int. J. Hydrogen Energy*, 2017, **42**, 2636–2647.
95 B. Heggen, S. Roy and F. Müller-Plathe, *J. Phys. Chem. C*, 2008, **112**, 14209–14215.
96 R. A. Krueger, L. Vilčiauskas, J.-P. Melchior, G. Bester and K.-D. Kreuer, *J. Phys. Chem. B*, 2015, **119**, 15866–15875.
97 Y. Özdemir, N. Özkan and Y. Devrim, *Electrochim. Acta*, 2017, **245**, 1–13.
98 N. N. Krishnan, S. Lee, R. V. Ghorpade, A. Konovalova, J. H. Jang, H.-J. Kim, J. Han, D. Henkensmeier and H. Han, *J. Membr. Sci.*, 2018, **560**, 11–20.
99 S. Bhadra, N. H. Kim and J. H. Lee, *J. Membr. Sci.*, 2010, **349**, 304–311.
100 A. Kannan, D. Aili, L. N. Cleemann, Q. Li and J. O. Jensen, *Int. J. Hydrogen Energy*, 2020, **45**, 1008–1017.
101 E. Quartarone, P. Mustarelli, A. Carollo, S. Grandi, A. Magistris and C. Gerbaldi, *Fuel Cells*, 2009, **9**, 231–236.
102 P. Mustarelli, E. Quartarone, S. Grandi, A. Carollo and A. Magistris, *Adv. Mater.*, 2008, **20**, 1339–1343.
103 Y. Devrim, H. Devrim and I. Eroglu, *Int. J. Hydrogen Energy*, 2016, **41**, 10044–10052.
104 D. Aili, J. Zhang, M. T. Dalsgaard Jakobsen, H. Zhu, T. Yang, J. Liu, M. Forsyth, C. Pan, J. O. Jensen, L. N. Cleemann, S. P. Jiang and Q. Li, *J. Mater. Chem. A*, 2016, **4**, 4019–4024.
105 A. Verma and K. Scott, *J. Solid State Electrochem.*, 2010, **14**, 213–219.
106 C. Xu, X. Wu, X. Wang, M. Mamlouk and K. Scott, *J. Mater. Chem.*, 2011, **21**, 6014.
107 R. Kannan, H. N. Kagalwala, H. D. Chaudhari, U. K. Kharul, S. Kurungot and V. K. Pillai, *J. Mater. Chem.*, 2011, **21**, 7223.
108 C.-M. C. Suryani, Y.-L. Liu and Y. M. Lee, *J. Mater. Chem.*, 2011, **21**, 7480.
109 J. Escorihuela, Ó. Sahuquillo, A. García-Bernabé, E. Giménez and V. Compañ, *Nanomaterials*, 2018, **8**, 775.
110 Y. Wu, X. Liu, F. Yang, L. Lee Zhou, B. Yin, P. Wang and L. Wang, *J. Membr. Sci.*, 2021, **630**, 119288.
111 J. Chen, L. Wang and L. Wang, *ACS Appl. Mater. Interfaces*, 2020, **12**, 41350–41358.
112 K. S. Lee, J. S. Spendelow, Y. K. Choe, C. Fujimoto and Y. S. Kim, *Nat. Energy*, 2016, **1**, 1–7.
113 V. Atanasov, A. S. Lee, E. J. Park, S. Maurya, E. D. Baca, C. Fujimoto, M. Hibbs, I. Matanovic, J. Kerres and Y. S. Kim, *Nat. Mater.*, 2021, **20**, 370–377.
114 K. H. Lim, A. S. Lee, V. Atanasov, J. Kerres, E. J. Park, S. Adhikari, S. Maurya, L. D. Manriquez, J. Jung, C. Fujimoto, I. Matanovic, J. Jankovic, Z. Hu, H. Jia and Y. S. Kim, *Nat. Energy*, 2022, **7**, 248–259.
115 H. Tang, K. Geng, L. Wu, J. Liu, Z. Chen, W. You, F. Yan, M. D. Guiver and N. Li, *Nat. Energy*, 2022, **7**, 153–162.
116 T. Engl, L. Gubler and T. J. Schmidt, in *High Temperature Polymer Electrolyte Membrane Fuel Cells*, Springer International Publishing, Cham, 2016, pp. 297–313.
117 N. Bevilacqua, R. R. Gokhale, A. Serov, R. Banerjee, M. A. Schmid, P. Atanassov and R. Zeis, *ECS Trans.*, 2018, **86**, 221–229.
118 N. M. Zagudaeva and M. R. Tarasevich, *Russ. J. Electrochem.*, 2010, **46**, 530–536.
119 A. Schenk, C. Grimmer, M. Perchthaler, S. Weinberger, B. Pichler, C. Heinzl, C. Scheu, F. A. Mautner, B. Bitschnau and V. Hacker, *J. Power Sources*, 2014, **266**, 313–322.
120 Y. Devrim, E. D. Arıca and A. Albostan, *Int. J. Hydrogen Energy*, 2018, **43**, 11820–11829.
121 H.-S. Oh, J.-H. Lee and H. Kim, *Int. J. Hydrogen Energy*, 2012, **37**, 10844–10849.
122 Y. Devrim and E. D. Arıca, *Int. J. Hydrogen Energy*, 2019, **44**, 18951–18966.

 This journal is © The Royal Society of Chemistry 2024

Open Access Article. Published on 07 March 2024. Downloaded on 1/20/2026 7:35:49 PM. This article is licensed under a Creative Commons Attribution 3.0 Unported Licence.

123 Y. Devrim and E. D. Arıca, *Int. J. Hydrogen Energy*, 2020, **45**, 3609–3617.
124 T. A. M. Suter, K. Smith, J. Hack, L. Rasha, Z. Rana, G. M. A. Angel, P. R. Shearing, T. S. Miller and D. J. L. Brett, *Adv. Energy Mater.*, 2021, **2101025**, 2101025.
125 J. Zhang, H. Wang, W. Li, J. Zhang, D. Lu, W. Yan, Y. Xiang and S. Lu, *J. Power Sources*, 2021, **505**, 230059.
126 J. Halter, N. Bevilacqua, R. Zeis, T. J. Schmidt and F. N. Büchi, *J. Electroanal. Chem.*, 2020, **859**, 113832.
127 N. Bevilacqua, T. Asset, M. A. Schmid, H. Markötter, I. Manke, P. Atanassov and R. Zeis, *J. Power Sources Adv.*, 2021, **7**, 100042.
128 F. Mack, T. Morawietz, R. Hiesgen, D. Kramer, V. Gogel and R. Zeis, *Int. J. Hydrogen Energy*, 2016, **41**, 7475–7483.
129 S. H. Kwon, S. Y. Lee, H.-J. Kim, S.-D. Yim, Y.-J. Sohn and S. G. Lee, *Sci. Rep.*, 2022, **12**, 3810.
130 J. Lobato, P. Cañizares, M. A. Rodrigo, J. J. Linares and F. J. Pinar, *Int. J. Hydrogen Energy*, 2010, **35**, 1347–1355.
131 J.-H. Kim, H.-J. Kim, T.-H. Lim and H.-I. Lee, *J. Power Sources*, 2007, **170**, 275–280.
132 D. Lee, J. W. Lim and D. G. Lee, *Compos. Struct.*, 2017, **167**, 144–151.
133 D. Lee, J. W. Lim, S. Nam, I. Choi and D. G. Lee, *Compos. Struct.*, 2015, **128**, 284–290.
134 C. Hartnig and T. J. Schmidt, *Electrochim. Acta*, 2011, **56**, 4237–4242.
135 M. Kim, J. W. Lim and D. G. Lee, *Compos. Struct.*, 2015, **119**, 630–637.
136 A. Ghosh and A. Verma, *Fuel Cells*, 2014, **14**, 259–265.
137 D. Lee and D. G. Lee, *J. Power Sources*, 2016, **327**, 119–126.
138 I. Kundler and T. Hickmann, in *High Temperature Polymer Electrolyte Membrane Fuel Cells*, Springer International Publishing, Cham, 2016, pp. 425–440.
139 C. J. Tseng, Y. J. Heush, C. J. Chiang, Y. H. Lee and K. R. Lee, *Int. J. Hydrogen Energy*, 2016, **41**, 16196–16204.
140 C.-Y. Chen and S.-C. Su, *Int. J. Hydrogen Energy*, 2018, **43**, 13430–13439.
141 W.-M. Yan, C.-Y. Chen and C.-H. Liang, *Energy*, 2019, **186**, 115836.
142 C. Alegre, L. Álvarez-Manuel, R. Mustata, L. Valiño, A. Lozano and F. Barreras, *Int. J. Hydrogen Energy*, 2019, **44**, 12748–12759.
143 A. Tang, L. Crisci, L. Bonville and J. Jankovic, *J. Renewable Sustainable Energy*, 2021, **13**, 022701.
144 S. Galbiati, A. Baricci, A. Casalegno and R. Marchesi, *Int. J. Hydrogen Energy*, 2012, **37**, 2462–2469.
145 F. Zhou, D. Singdeo and S. K. Kær, *Fuel Cells*, 2019, **19**, 2–9.
146 D. Schonvogel, M. Rastedt, P. Wagner, M. Wark and A. Dyck, *Fuel Cells*, 2016, **16**, 480–489.
147 Y. H. Jeong, K. Oh, S. Ahn, N. Y. Kim, A. Byeon, H. Y. Park, S. Y. Lee, H. S. Park, S. J. Yoo, J. H. Jang, H. J. Kim, H. Ju and J. Y. Kim, *J. Power Sources*, 2017, **363**, 365–374.
148 E. Quartarone and P. Mustarelli, *Energy Environ. Sci.*, 2012, **5**, 6436.
149 S. Yu, L. Xiao and B. C. Benicewicz, *Fuel Cells*, 2008, **8**, 165–174.
150 Y. Özdemir, N. Üregen and Y. Devrim, *Int. J. Hydrogen Energy*, 2017, **42**, 2648–2657.
151 D. Úbeda, F. J. Pinar, D. C. Orozco, P. Cañizares, M. A. Rodrigo and J. Lobato, *J. Appl. Electrochem.*, 2012, **42**, 711–718.
152 S. Kaserer, K. M. Caldwell, D. E. Ramaker and C. Roth, *J. Phys. Chem. C*, 2013, **117**, 6210–6217.
153 D. Úbeda, P. Cañizares, M. A. Rodrigo, F. J. Pinar and J. Lobato, *Int. J. Hydrogen Energy*, 2014, **39**, 21678–21687.
154 J. Lobato, P. Cañizares, M. A. Rodrigo, F. J. Pinar and D. Úbeda, *J. Power Sources*, 2011, **196**, 4209–4217.
155 J. Li, L. Yang, H. Sun and G. Sun, *Energy Technol.*, 2022, **2100809**, 2100809.
156 T. Søndergaard, L. N. Cleemann, L. Zhong, H. Becker, T. Steenberg, H. A. Hjuler, L. Seerup, Q. Li and J. O. Jensen, *Electrocatalysis*, 2018, **9**, 302–313.
157 J. Halter, F. Marone, T. J. Schmidt and F. N. Büchi, *J. Electrochem. Soc.*, 2018, **165**, F1176–F1183.
158 L. N. Cleemann, F. Buazar, Q. Li, J. O. Jensen, C. Pan, T. Steenberg, S. Dai and N. J. Bjerrum, *Fuel Cells*, 2013, 822–831.
159 D. E. Hussin, Y. Budak and Y. Devrim, *Int. J. Energy Res.*, 2022, **46**, 4174–4186.
160 E. Quartarone and P. Mustarelli, *Energy Environ. Sci.*, 2012, **5**, 6436–6444.
161 E. Lee, D. H. Kim and C. Pak, *Appl. Surf. Sci.*, 2020, **510**, 145461.
162 G. Liu, H. Zhang, J. Hu, Y. Zhai, D. Xu and Z. gang Shao, *J. Power Sources*, 2006, **162**, 547–552.
163 J.-C. Lin, C.-M. Lai, F.-P. Ting, S.-D. Chyou and K.-L. Hsueh, *J. Appl. Electrochem.*, 2009, **39**, 1067–1073.
164 Q. Meyer, N. Mansor, F. Iacoviello, P. L. Cullen, R. Jervis, D. Finegan, C. Tan, J. Bailey, P. R. Shearing and D. J. L. Brett, *Electrochim. Acta*, 2017, **242**, 125–136.
165 A. Zucconi, J. Hack, T. A. M. Suter, M. Braglia, P. R. Shearing, D. J. L. Brett and A. J. E. Rettie, *J. Power Sources*, 2023, **584**, 233574.
166 P. Choi, N. H. Jalani and R. Datta, *J. Electrochem. Soc.*, 2005, **152**, E123.
167 M. Geormezi, F. Paloukis, A. Orfanidi, N. Shroti, M. K. Daletou and S. G. Neophytides, *J. Power Sources*, 2015, **285**, 499–509.
168 A. Kannan, Q. Li, L. N. Cleemann and J. O. Jensen, *Fuel Cells*, 2018, **18**, 103–112.
169 S. Thomas, S. S. Araya, J. R. Vang and S. K. Kær, *Int. J. Hydrogen Energy*, 2018, **43**, 14691–14700.
170 T. Tingelöf and J. K. Ihonen, *Int. J. Hydrogen Energy*, 2009, **34**, 6452–6456.
171 M. Boaventura and A. Mendes, *Int. J. Hydrogen Energy*, 2010, **35**, 11649–11660.
172 S. Galbiati, A. Baricci, A. Casalegno, G. Carcassola and R. Marchesi, *Int. J. Hydrogen Energy*, 2012, **37**, 14475–14481.
173 J. R. Vang, S. J. Andreasen, S. S. Araya and S. K. Kær, *Int. J. Hydrogen Energy*, 2014, **39**, 14959–14968.
174 G. Qian and B. C. Benicewicz, *ECS Trans.*, 2011, **41**, 1441–1448.

Open Access Article. Published on 07 March 2024. Downloaded on 1/20/2026 7:35:49 PM. This article is licensed under a Creative Commons Attribution 3.0 Unported Licence.

175 M. Zhiani, S. Majidi and M. M. Taghiabadi, *Fuel Cells*, 2013, **13**(5), 946–955.
176 M. Zhiani and S. Majidi, *Int. J. Hydrogen Energy*, 2013, **38**, 9819–9825.
177 X. Z. Yuan, S. Zhang, J. C. Sun and H. Wang, *J. Power Sources*, 2011, **196**, 9097–9106.
178 G. Tsotridis, A. Pilenga, G. De Marco and T. Malkow, *EU Harmonised Test Protocols for PEMFC MEA Testing in Single Cell Configuration for Automotive Applications*, JRC Science for Policy report, 2015.
179 Y. Wang, D. U. Sauer, S. Koehne and A. Ersöz, *Int. J. Hydrogen Energy*, 2014, **39**, 19067–19078.
180 R. K. Abdul Rasheed, S. M. M. Ehteshami and S. H. Chan, *Int. J. Hydrogen Energy*, 2014, **39**, 2246–2260.
181 H. Huang, Y. Zhou, H. Deng, X. Xie, Q. Du, Y. Yin and K. Jiao, *Int. J. Hydrogen Energy*, 2016, **41**, 3113–3127.
182 M. Choi, M. Kim, Y.-J. Sohn and S.-G. Kim, *Int. J. Hydrogen Energy*, 2021, **46**, 36982–36994.
183 J. Zhang, C. Zhang, D. Hao, M. Ni, S. Huang, D. Liu and Y. Zheng, *Int. J. Hydrogen Energy*, 2021, **46**, 2577–2593.
184 R. E. Rosli, A. B. Sulong, W. R. W. Daud, M. A. Zulkifley, M. I. Rosli, E. H. Majlan, M. A. Haque and N. A. M. Radzuan, *Int. J. Hydrogen Energy*, 2019, **44**, 30763–30771.
185 J. Zhao, D. Song, J. Jia, N. Wang, K. Liu, T. Zuo and Q. Che, *Appl. Surf. Sci.*, 2022, **585**, 152579.
186 S. Liu, M. Rasinski, Y. Rahim, S. Zhang, K. Wippermann, U. Reimer and W. Lehnert, *J. Power Sources*, 2019, **439**, 227090.
187 S. Galbiati, A. Baricci, A. Casalegno and R. Marchesi, *Int. J. Hydrogen Energy*, 2013, **38**, 6469–6480.
188 Y. Oono, T. Fukuda, A. Sounai and M. Hori, *J. Power Sources*, 2010, **195**, 1007–1014.
189 M. Rastedt, D. Schonvogel and P. Wagner, *ECS Trans.*, 2014, **64**, 741–753.
190 F. Zhou, S. J. Andreasen and S. K. Kær, *Int. J. Hydrogen Energy*, 2015, **40**, 6672–6680.
191 A. Stassi, I. Gatto, E. Passalacqua, V. Antonucci, A. S. Arico, L. Merlo, C. Oldani and E. Pagano, *J. Power Sources*, 2011, **196**, 8925–8930.
192 A. Suzuki, Y. Oono, M. C. Williams, R. Miura, K. Inaba, N. Hatakeyama, H. Takaba, M. Hori and A. Miyamoto, *Int. J. Hydrogen Energy*, 2012, **37**, 18272–18289.
193 T. Engl, L. Gubler and T. J. Schmidt, *J. Electrochem. Soc.*, 2015, **162**, F291–F297.
194 J. Li, L. Yang, Z. Wang, H. Sun and G. Sun, *Int. J. Hydrogen Energy*, 2021, **46**, 24353–24365.
195 Z. Chang, H. Pu, D. Wan, L. Liu, J. Yuan and Z. Yang, *Polym. Degrad. Stab.*, 2009, **94**, 1206–1212.
196 J. Liao, J. Yang, Q. Li, L. N. Cleemann, J. O. Jensen, N. J. Bjerrum, R. He and W. Xing, *J. Power Sources*, 2013, **238**, 516–522.
197 H. Schmies, D. Schonvogel, J. Büsselmann, P. Wagner and A. Dyck, *ECS Meet. Abstr.*, 2020, MA2020-02, p. 2161.
198 J. Büsselmann, M. Rastedt, T. Klicpera, K. Reinwald, H. Schmies, A. Dyck and P. Wagner, *Energies*, 2020, **13**, 567.
199 F. Zhou, S. J. Andreasen, S. K. Kær and J. O. Park, *Int. J. Hydrogen Energy*, 2015, **40**, 14932–14941.
200 Y. Rahim, H. Janßen and W. Lehnert, *Int. J. Hydrogen Energy*, 2017, **42**, 1189–1202.
201 C.-Y. Chen, C.-C. Chen, S.-W. Hsu, M.-P. Lai, W.-H. Lai and W.-M. Yang, *Energy Procedia*, 2012, **29**, 64–71.
202 H. Lu, L. Rihko-Struckmann, R. Hanke-Rauschenbach and K. Sundmacher, *Top. Catal.*, 2008, **51**, 89–97.
203 V. F. Valdés-López, T. Mason, P. R. Shearing and D. J. L. Brett, *Prog. Energy Combust. Sci.*, 2020, **79**, 100842.
204 A. Al-Qahtani, B. Parkinson, K. Hellgardt, N. Shah and G. Guillen-Gosalbez, *Appl. Energy*, 2021, **281**, 115958.
205 T. Engl, J. Kase, L. Gubler and T. J. Schmidt, *ECS Electrochem. Lett.*, 2014, **3**, F47–F49.
206 T. J. Schmidt and J. Baurmeister, *J. Power Sources*, 2008, **176**, 428–434.
207 H. Becker, U. Reimer, D. Aili, L. N. Cleemann, J. O. Jensen, W. Lehnert and Q. Li, *J. Electrochem. Soc.*, 2018, **165**, F863–F869.
208 S. H. Eberhardt, F. Marone, M. Stampanoni, F. N. Büchi and T. J. Schmidt, *J. Electrochem. Soc.*, 2016, **163**, F842–F847.
209 S. H. Eberhardt, M. Toulec, F. Marone, M. Stampanoni, F. N. Büchi and T. J. Schmidt, *J. Electrochem. Soc.*, 2015, **162**, F310–F316.
210 Q. Li, R. He, R. W. Berg, H. A. Hjuler and N. J. Bjerrum, *Solid State Ionics*, 2004, **168**, 177–185.
211 A. S. Lee, Y. K. Choe, I. Matanovic and Y. S. Kim, *J. Mater. Chem. A*, 2019, **7**, 9867–9876.
212 S. H. Eberhardt, T. Lochner, F. N. Büchi and T. J. Schmidt, *J. Electrochem. Soc.*, 2015, **162**, F1367–F1372.
213 Q. He, X. Yang, W. Chen, S. Mukerjee, B. Koel and S. Chen, *Phys. Chem. Chem. Phys.*, 2010, **12**, 12544–12555.
214 K. M. Caldwell, S. Kaserer, C. Roth and D. E. Ramaker, *ChemElectroChem*, 2015, **2**, 1502–1509.
215 K. S. Lee, S. Maurya, Y. S. Kim, C. R. Kreller, M. S. Wilson, D. Larsen, S. E. Elangovan and R. Mukundan, *Energy Environ. Sci.*, 2018, **11**, 979–987.
216 J. Hou, *Int. J. Hydrogen Energy*, 2011, **36**, 7199–7206.
217 U.S. Drive, Fuel Cell Technical Team, Fuel Cell Technical Team Roadmap, **https://www.energy.gov/sites/prod/files/2017/11/f46/FCTT_Roadmap_Nov_2017_FINAL.pdf**, accessed 17 February 2022.
218 Y. Wang, D. F. Ruiz Diaz, K. S. Chen, Z. Wang and X. C. Adroher, *Mater. Today*, 2020, **32**, 178–203.
219 J. Büsselmann, M. Rastedt, V. Tullius, K. Yezerska, A. Dyck and P. Wagner, *Int. J. Hydrogen Energy*, 2019, **4**, 19384–19394.
220 Q. Xie, Y. Li, X. Chen, J. Hu, L. Li and H. Li, *J. Power Sources*, 2015, **282**, 489–497.
221 Z. Di, Q. Xie, H. Li, D. Mao, M. Li, D. Zhou and L. Li, *J. Power Sources*, 2015, **273**, 688–696.
222 Y. Devrim, S. Erkan, N. Baç and I. Eroglu, *Int. J. Hydrogen Energy*, 2012, **37**, 16748–16758.
223 K. Oh, B. Son, J. Sanetuntikul and S. Shanmugam, *J. Membr. Sci.*, 2017, **541**, 386–392.

This journal is © The Royal Society of Chemistry 2024

Open Access Article. Published on 07 March 2024. Downloaded on 1/20/2026 7:35:49 PM. This article is licensed under a Creative Commons Attribution 3.0 Unported Licence.

224 N. H. Kim, A. K. Mishra, D.-Y. Kim and J. H. Lee, *Chem. Eng. J.*, 2015, **272**, 119–127.
225 European Commission, Volume Manufacturing of PEM FC Stacks for Transportation and In-line Quality Assurance, **https://cordis.europa.eu/project/id/671465/reporting**, accessed 17 February 2022.
226 A. Kongkanand and M. F. Mathias, *J. Phys. Chem. Lett.*, 2016, **7**, 1127–1137.
227 M. R. Berber and N. Nakashima, *J. Membr. Sci.*, 2019, **591**, 117354.
228 V. Elumalai, R. Annapooranan, M. Ganapathikrishnan and D. Sangeetha, *J. Appl. Polym. Sci.*, 2018, **135**, 45954.
229 C. Gao, M. Hu, L. Wang and L. Wang, *Polymers*, 2020, **12**, 515.
230 L. Wang, Y. Wu, M. Fang, J. Chen, X. Liu, B. Yin and L. Wang, *J. Membr. Sci.*, 2020, **602**, 117981.
231 N. Nambi Krishnan, A. Konovalova, D. Aili, Q. Li, H. S. Park, J. H. Jang, H.-J. Kim and D. Henkensmeier, *J. Membr. Sci.*, 2019, **588**, 117218.
232 H. Chen, S. Wang, F. Liu, D. Wang, J. Li, T. Mao, G. Liu, X. Wang, J. Xu and Z. Wang, *J. Membr. Sci.*, 2020, **596**, 117722.
233 B. WAHDAME, D. CANDUSSO, X. FRANCOIS, F. HAREL, M. PERA, D. HISSEL and J. KAUFFMANN, *Int. J. Hydrogen Energy*, 2007, **32**, 4523–4536.
234 S. J. C. Cleghorn, D. K. Mayfield, D. A. Moore, J. C. Moore, G. Rusch, T. W. Sherman, N. T. Sisofo and U. Beuscher, *J. Power Sources*, 2006, **158**, 446–454.
235 J. St-Pierre and N. Jia, *J. New Mater. Electrochem. Syst.*, 2002, **5**, 263–271.
236 J. Yu, T. Matsuura, Y. Yoshikawa, M. N. Islam and M. Hori, *Electrochem. Solid-State Lett.*, 2005, **8**, A156.
237 P. J. Ferreira, G. J. la O', Y. Shao-Horn, D. Morgan, R. Makharia, S. Kocha and H. A. Gasteiger, *J. Electrochem. Soc.*, 2005, **152**, A2256.
238 A. Kannan, A. Kabza and J. Scholta, *J. Power Sources*, 2015, **277**, 312–316.
239 F. J. Pinar, P. Cañizares, M. A. Rodrigo, D. Úbeda and J. Lobato, *J. Power Sources*, 2015, **274**, 177–185.
240 J. R. Kim, J. S. Yi and T. W. Song, *J. Power Sources*, 2012, **220**, 54–64.
241 T. Søndergaard, L. N. Cleemann, H. Becker, D. Aili, T. Steenberg, H. A. Hjuler, L. Seerup, Q. Li and J. O. Jensen, *J. Power Sources*, 2017, **342**, 570–578.
242 P. Moçotéguy, B. Ludwig, J. Scholta, R. Barrera and S. Ginocchio, *Fuel Cells*, 2009, **9**, 325–348.
243 C. Jeppesen, S. S. Araya, S. L. Sahlin, S. Thomas, S. J. Andreasen and S. K. Kær, *J. Power Sources*, 2017, **359**, 37–47.
244 J. Zhang, D. Aili, J. Bradley, H. Kuang, C. Pan, R. De Marco, Q. Li and S. P. Jiang, *J. Electrochem. Soc.*, 2017, **164**, F1615–F1625.
245 Y. Y. Jo, E. Cho, J. H. Kim, T.-H. Lim, I.-H. Oh, S.-K. Kim, H.-J. Kim and J. H. Jang, *J. Power Sources*, 2011, **196**, 9906–9915.
246 J. Han, J. Han and S. Yu, *Int. J. Hydrogen Energy*, 2020, **45**, 13045–13054.
247 K. Eom, G. Kim, E. Cho, J. H. Jang, H.-J. Kim, S. J. Yoo, S.-K. Kim and B. K. Hong, *Int. J. Hydrogen Energy*, 2012, **37**, 18455–18462.
248 K. Meng, H. Zhou, B. Chen and Z. Tu, *Energy*, 2021, **224**, 120168.
249 T. Chu, M. Xie, Y. Yu, B. Wang, D. Yang, B. Li, P. Ming and C. Zhang, *Energy*, 2022, **239**, 122356.
250 S. Komini Babu, D. Spernjak, J. Dillet, A. Lamibrac, G. Maranzana, S. Didierjean, O. Lottin, R. L. Borup and R. Mukundan, *Appl. Energy*, 2019, **254**, 113659.
251 R. K. Ahluwalia, X. Wang, J.-K. Peng, N. N. Kariuki, D. J. Myers, S. Rasouli, P. J. Ferreira, Z. Yang, A. Martinez-Bonastre, D. Fongalland and J. Sharman, *J. Electrochem. Soc.*, 2018, **165**, F3316–F3327.
252 C. Hartnig and T. J. Schmidt, *J. Power Sources*, 2011, **196**, 5564–5572.
253 S. Rigal, C. Turpin, A. Jaafar, T. Hordé, J. -B. Jollys and N. Chadourne, *Fuel Cells*, 2020, **20**, 272–284.
254 M. Baudy, A. Jaafar, C. Turpin, S. Abbou and S. Rigal, *Int. J. Hydrogen Energy*, 2023, **48**, 20945–20956.
255 S. S. Araya, S. J. Andreasen and S. K. Kær, *J. Fuel Cell Sci. Technol.*, 2014, **11**, 1–7.
256 C. Zhang, Z. Liu, W. Zhou, S. H. Chan and Y. Wang, *Energy*, 2015, **90**, 1949–1955.
257 U. Reimer, B. Schumacher and W. Lehnert, *J. Electrochem. Soc.*, 2015, **162**, F153–F164.
258 M. A. Rubio, A. Urquia and S. Dormido, *J. Power Sources*, 2007, **171**, 670–677.
259 K. R. Cooper and M. Smith, *J. Power Sources*, 2006, **160**, 1088–1095.
260 S. Wang, J. Zhang, O. Gharbi, V. Vivier, M. Gao and M. E. Orazem, *Nat. Rev. Methods Primers*, 2021, **1**, 41.
261 S. M. Rezaei Niya and M. Hoorfar, *J. Power Sources*, 2013, **240**, 281–293.
262 X. Yuan, H. Wang, J. Colin Sun and J. Zhang, *Int. J. Hydrogen Energy*, 2007, **32**, 4365–4380.
263 J. J. Giner-Sanz, E. M. Ortega and V. Pérez-Herranz, *Fuel Cells*, 2016, **16**, 469–479.
264 F. J. Pinar, M. Rastedt, N. Pilinski and P. Wagner, in *High Temperature Polymer Electrolyte Membrane Fuel Cells*, Springer International Publishing, Cham, 2016, pp. 353–386.
265 A. Weiß, S. Schindler, S. Galbiati, M. A. Danzer and R. Zeis, *Electrochim. Acta*, 2017, **230**, 391–398.
266 A. Baricci and A. Casalegno, *Energies*, 2023, **16**, 4671.
267 K. Ruan, L. Yang, H. Sun and G. Sun, *J. Power Sources*, 2022, **523**, 231000.
268 T. Gaumont, G. Maranzana, O. Lottin, J. Dillet, S. Didierjean, J. Pauchet and L. Guétaz, *Int. J. Hydrogen Energy*, 2017, **42**, 1800–1812.
269 I. Pivac and F. Barbir, *J. Power Sources*, 2016, **326**, 112–119.
270 X.-Z. Yuan, C. Song, H. Wang and J. Zhang, *Electrochemical Impedance Spectroscopy in PEM Fuel Cells*, Springer London, London, 2010.
271 A. Diedrichs, M. Rastedt, F. J. Pinar and P. Wagner, *J. Appl. Electrochem.*, 2013, **43**, 1079–1099.

Open Access Article. Published on 07 March 2024. Downloaded on 1/20/2026 7:35:49 PM. This article is licensed under a Creative Commons Attribution 3.0 Unported Licence.

272 S. Simon Araya, S. Thomas, A. Lotrič, S. Lennart Sahlin, V. Liso and S. J. Andreasen, *Energies*, 2021, **14**, 2994.
273 Q. Meyer, I. Pivac, F. Barbir and C. Zhao, *J. Power Sources*, 2020, **470**, 228285.
274 J. Chen, J. J. Bailey, L. Britnell, M. Perez-Page, M. Sahoo, Z. Zhang, A. Strudwick, J. Hack, Z. Guo, Z. Ji, P. Martin, D. J. L. Brett, P. R. Shearing and S. M. Holmes, *Nano Energy*, 2022, **93**, 106829.
275 S. Dierickx, A. Weber and E. Ivers-Tiffée, *Electrochim. Acta*, 2020, **355**, 136764.
276 M. Heinzmann, A. Weber and E. Ivers-Tiffée, *J. Power Sources*, 2019, **444**, 227279.
277 M. Hinaje, S. Raël, P. Noiying, D. A. Nguyen and B. Davat, *Energies*, 2012, **5**, 2724–2744.
278 F. Tiss, R. Chouikh and A. Guizani, *Int. J. Hydrogen Energy*, 2013, **38**, 8532–8541.
279 M. Heinzmann, A. Weber and E. Ivers-Tiffée, *J. Power Sources*, 2018, **402**, 24–33.
280 D. Klotz, A. Weber and E. Ivers-Tiffée, *Electrochim. Acta*, 2017, **227**, 110–126.
281 D. Yao, T. C. Jao, W. Zhang, L. Xu, L. Xing, Q. Ma, Q. Xu, H. Li, S. Pasupathi and H. Su, *Int. J. Hydrogen Energy*, 2018, **43**, 21006–21016.
282 X. Zhang, T. Zhang, H. Chen and Y. Cao, *Appl. Energy*, 2021, **286**, 116481.
283 S. K. Roy, M. E. Orazem and B. Tribollet, *J. Electrochem. Soc.*, 2007, **154**, B1378–B1388.
284 O. Antoine, Y. Bultel and R. Durand, *J. Electroanal. Chem.*, 2001, **499**, 85–94.
285 A. Schiefer, M. Heinzmann and A. Weber, *Fuel Cells*, 2020, **20**, 499–506.
286 H. Kuhn, A. Wokaun and G. G. Scherer, *Electrochim. Acta*, 2007, **52**, 2322–2327.
287 B. P. Setzler and T. F. Fuller, *J. Electrochem. Soc.*, 2015, **162**, F519–F530.
288 K. Wiezell, P. Gode and G. Lindbergh, *J. Electrochem. Soc.*, 2006, **153**, A749–A758.
289 N. Holmström, K. Wiezell and G. Lindbergh, *J. Electrochem. Soc.*, 2012, **159**, F369–F378.
290 I. A. Schneider, M. H. Bayer, A. Wokaun and G. G. Scherer, *J. Electrochem. Soc.*, 2008, **155**, B783.
291 C. Gerling, M. Hanauer, U. Berner and K. A. Friedrich, *J. Electrochem. Soc.*, 2023, **170**, 014504.
292 T. V. Reshetenko, K. Bethune and R. Rocheleau, *J. Power Sources*, 2012, **218**, 412–423.
293 N. Wagner and M. Schulze, *Electrochim. Acta*, 2003, **48**, 3899–3907.
294 T. V. Reshetenko, K. Bethune, M. A. Rubio and R. Rocheleau, *J. Power Sources*, 2014, **269**, 344–362.
295 M. Wagner, O. Lorenz, F. P. Lohmann-Richters, Á. Varga and B. Abel, *J. Mater. Chem. A*, 2021, **9**, 11347–11358.
296 T. H. Wan, M. Saccoccio, C. Chen and F. Ciucci, *Electrochim. Acta*, 2015, **184**, 483–499.
297 F. Ciucci and C. Chen, *Electrochim. Acta*, 2015, **167**, 439–454.
298 A. Kulikovsky, *J. Phys. Chem. C*, 2022, **126**, 2424–2429.
299 T. Reshetenko and A. Kulikovsky, *J. Electrochem. Soc.*, 2020, **167**, 144505.
300 N. Bevilacqua, M. A. Schmid and R. Zeis, *J. Power Sources*, 2020, **471**, 228469.
301 J. Xu, Y. Wu, S. Xiao, Y. Wang and X. Xu, *Renewable Energy*, 2023, **211**, 669–680.
302 Y. Zhang, Y. Chen, M. Yan and F. Chen, *J. Power Sources*, 2015, **283**, 464–477.
303 J. Weese, *Comput. Phys. Commun.*, 1992, **69**, 99–111.
304 E. Ivers-Tiffée and A. Weber, *J. Ceram. Assoc. Jpn.*, 2017, **125**, 193–201.
305 E. Brightman, G. Hinds and R. O'Malley, *J. Power Sources*, 2013, **242**, 244–254.
306 T. Engl, K. E. Waltar, L. Gubler and T. J. Schmidt, *J. Electrochem. Soc.*, 2014, **161**, F500–F505.
307 F. Wang, D. Yang, B. Li, H. Zhang, C. Hao, F. Chang and J. Ma, *Int. J. Hydrogen Energy*, 2014, **39**, 14441–14447.
308 K. H. Kim, K. Y. Lee, S. Y. Lee, E. Cho, T. H. Lim, H. J. Kim, S. P. Yoon, S. H. Kim, T. W. Lim and J. H. Jang, *Int. J. Hydrogen Energy*, 2010, **35**, 13104–13110.
309 H. Niu, C. Ji, S. Wang and C. Liang, *Int. J. Hydrogen Energy*, 2022, **47**, 2662–2672.
310 J. Xie, D. L. Wood, D. M. Wayne, T. A. Zawodzinski, P. Atanassov and R. L. Borup, *J. Electrochem. Soc.*, 2005, **152**, A104.
311 J. Parrondo, C. Venkateswara Rao, S. L. Ghatty and B. Rambabu, *Int. J. Electrochem.*, 2011, **2011**, 1–8.
312 P. N. Ross and P. C. Andricacos, *J. Electroanal. Chem. Interfacial Electrochem.*, 1983, **154**, 205–215.
313 E. Zagoraiou, F. Paloukis, S. G. Neophytides and M. K. Daletou, *Electrochim. Acta*, 2020, **356**, 136778.
314 S. S. Kocha, J. Deliang Yang and J. S. Yi, *AIChE J.*, 2006, **52**, 1916–1925.
315 S. Zhang, X.-Z. Yuan and H. Wang, in *PEM Fuel Cell Diagnostic Tools*, CRC Press, 2011, pp. 87–100.
316 S. R. Choi, D. Y. Kim, W. Y. An, S. Choi, K. Park, S. D. Yim and J. Y. Park, *Mater. Sci. Energy Technol.*, 2022, **5**, 66–73.
317 M. Geske, M. Heuer, G. Heideck and Z. A. Styczynski, *Energies*, 2010, **3**, 770–783.
318 G. Zhang, S. Shen, L. Guo and H. Liu, *Int. J. Hydrogen Energy*, 2012, **37**, 1884–1892.
319 D. Gerteisen, N. Zamel, C. Sadeler, F. Geiger, V. Ludwig and C. Hebling, *Int. J. Hydrogen Energy*, 2012, **37**, 7736–7744.
320 Y. Yu, X. Z. Yuan, H. Li, E. Gu, H. Wang, G. Wang and M. Pan, *Int. J. Hydrogen Energy*, 2012, **37**, 15288–15300.
321 D. J. L. Brett, S. Atkins, N. P. Brandon, N. Vasileiadis, V. Vesovic and A. R. Kucernak, *J. Power Sources*, 2007, **172**, 2–13.
322 D. J. Brett, S. Atkins, N. P. Brandon, V. Vesovic, N. Vasileiadis and A. R. Kucernak, *Electrochem. Commun.*, 2001, **3**, 628–632.
323 T. Nasu, Y. Matsushita, J. Okano and K. Okajima, *J. Int. Counc. Electr. Eng.*, 2012, **2**, 391–396.
324 K.-H. Hauer, R. Potthast, T. Wüster and D. Stolten, *J. Power Sources*, 2005, **143**, 67–74.

 This journal is © The Royal Society of Chemistry 2024

Open Access Article. Published on 07 March 2024. Downloaded on 1/20/2026 7:35:49 PM. This article is licensed under a Creative Commons Attribution 3.0 Unported Licence.

325 J. Dillet, D. Spernjak, A. Lamibrac, G. Maranzana, R. Mukundan, J. Fairweather, S. Didierjean, R. L. Borup and O. Lottin, *J. Power Sources*, 2014, **250**, 68–79.
326 V. Lilavivat, S. Shimpalee, J. W. Van Zee, H. Xu and C. K. Mittelsteadt, *Electrochim. Acta*, 2015, **174**, 1253–1260.
327 D. Gerteisen, W. Mérida, T. Kurz, P. Lupotto, M. Schwager and C. Hebling, *Fuel Cells*, 2011, **11**, 339–349.
328 Q. Zhang, R. Lin, L. Técher and X. Cui, *Energy*, 2016, **115**, 550–560.
329 Q. Meyer, K. Ronaszegi, J. B. Robinson, M. Noorkami, O. Curnick, S. Ashton, A. Danelyan, T. Reisch, P. Adcock, R. Kraume, P. R. Shearing and D. J. L. Brett, *J. Power Sources*, 2015, **297**, 315–322.
330 C. Siegel, G. Bandlamudi, F. Filusch and A. Heinzel, *Fuel Cells*, 2011, **11**, 489–500.
331 T. Sousa, M. Mamlouk, K. Scott and C. M. Rangel, *Fuel Cells*, 2012, **12**, 566–576.
332 H. Agarwal, A. U. Thosar, S. D. Bhat and A. K. Lele, *J. Power Sources*, 2022, **532**, 231319.
333 D. Úbeda, P. Cañizares, P. Ferreira-Aparicio, A. M. Chaparro, J. Lobato and M. A. Rodrigo, *Int. J. Hydrogen Energy*, 2016, **41**, 20294–20304.
334 A. Bergmann, T. Kurz, D. Gerteisen and C. Hebling, in *18th World Hydrogen Energy Conference 2010 - WHEC 2010 Parallel Sessions Book 1*: Fuel Cell Basics/Fuel Infrastructures, 2010.
335 K. Yezerska, A. Dushina, F. Liu, M. Rastedt, P. Wagner, A. Dyck and M. Wark, *Int. J. Hydrogen Energy*, 2019, **44**, 18330–18339.
336 S. Litster, W. K. Epting, E. A. Wargo, S. R. Kalidindi and E. C. Kumbur, *Fuel Cells*, 2013, 935–945.
337 V. S. Bethapudi, J. Hack, P. Trogadas, J. I. S. Cho, L. Rasha, G. Hinds, P. R. Shearing, D. J. L. Brett and M.-O. Coppens, *Energy Convers. Manage.*, 2019, **202**, 112198.
338 Q. Meyer, J. Hack, N. Mansor, F. Iacoviello, J. J. Bailey, P. R. Shearing and D. J. L. Brett, *Fuel Cells*, 2019, **19**, 35–42.
339 J. Park, H. Oh, H. Park, J. W. Moon, S. J. Lee and S. Y. Jung, *Int. J. Energy Res.*, 2022, **46**, 9058–9070.
340 J. Hack, T. M. M. Heenan, F. Iacoviello, N. Mansor, Q. Meyer, P. Shearing, N. Brandon and D. J. L. Brett, *J. Electrochem. Soc.*, 2018, **165**, F3045–F3052.
341 T. M. M. Heenan, C. Tan, J. Hack, D. J. L. Brett and P. R. Shearing, *Mater. Today*, 2019, **31**, 69–85.
342 E. Hoppe, H. Janßen, M. Müller and W. Lehnert, *J. Power Sources*, 2021, **501**, 230036.
343 F. Javier Pinar, M. Rastedt, N. Pilinski and P. Wagner, *Int. J. Hydrogen Energy*, 2016, **41**, 19463–19474.
344 J. J. Bailey, J. Chen, J. Hack, M. Perez-Page, S. M. Holmes, D. J. L. Brett and P. R. Shearing, *J. Power Sources*, 2021, **509**, 230347.
345 K. Tang, Q. Meyer, R. White, R. T. Armstrong, P. Mostaghimi, Y. Da Wang, S. Liu, C. Zhao, K. Regenauer-Lieb and P. K. M. Tung, *Comput. Chem. Eng.*, 2022, **161**, 107768.
346 O. Sekizawa, T. Uruga, N. Ishiguro, H. Matsui, K. Higashi, T. Sakata, Y. Iwasawa and M. Tada, *J. Phys.: Conf. Ser.*, 2017, **849**, 012022.
347 W. K. Epting, J. Gelb and S. Litster, *Adv. Funct. Mater.*, 2012, **22**, 555–560.
348 S. Komini Babu, H. T. Chung, P. Zelenay and S. Litster, *ACS Appl. Mater. Interfaces*, 2016, **8**, 32764–32777.
349 A. Pokhrel, M. El Hannach, F. P. Orfino, M. Dutta and E. Kjeang, *J. Power Sources*, 2016, **329**, 330–338.
350 A. Mularczyk, Q. Lin, D. Niblett, A. Vasile, M. J. Blunt, V. Niasar, F. Marone, T. J. Schmidt, F. N. Büchi and J. Eller, *ACS Appl. Mater. Interfaces*, 2021, **13**, 34003–34011.
351 M. Sepe, P. Satjaritanun, I. V. Zenyuk, N. Tippayawong and S. Shimpalee, *J. Electrochem. Soc.*, 2021, **168**, 074507.
352 A. D. Shum, C. P. Liu, W. H. Lim, D. Y. Parkinson and I. V. Zenyuk, *Transp. Porous Media*, 2022, **144**, 715–737.
353 Y.-C. Chen, A. Berger, S. De Angelis, T. Schuler, M. Bozzetti, J. Eller, V. Tileli, T. J. Schmidt and F. N. Büchi, *ACS Appl. Mater. Interfaces*, 2021, **13**, 16227–16237.
354 S. Chevalier, N. Ge, J. Lee, M. G. George, H. Liu, P. Shrestha, D. Muirhead, N. Lavielle, B. D. Hatton and A. Bazylak, *J. Power Sources*, 2017, **352**, 281–290.
355 S. S. Alrwashdeh, A. M. Al-Falahat, H. Markötter and I. Manke, *Case Stud. Chem. Environ. Eng.*, 2022, **6**, 100260.
356 A. Kato, S. Kato, S. Yamaguchi, T. Suzuki and Y. Nagai, *J. Power Sources*, 2022, **521**, 230951.
357 D. Kulkarni, S. J. Normile, L. G. Connolly and I. V Zenyuk, *JPhys Energy*, 2020, **2**, 044005.
358 R. T. White, A. Wu, M. Najm, F. P. Orfino, M. Dutta and E. Kjeang, *J. Power Sources*, 2017, **350**, 94–102.
359 R. T. White, S. H. Eberhardt, Y. Singh, T. Haddow, M. Dutta, F. P. Orfino and E. Kjeang, *Sci. Rep.*, 2019, **9**, 1–12.
360 J. Hack, L. Rasha, P. L. Cullen, J. J. Bailey, T. P. Neville, P. R. Shearing, N. P. Brandon and D. J. L. Brett, *Electrochim. Acta*, 2020, **352**, 136464.
361 D. Ramani, Y. Singh, R. T. White, M. Wegener, F. P. Orfino, M. Dutta and E. Kjeang, *Int. J. Hydrogen Energy*, 2020, **45**, 10089–10103.
362 Y. Singh, R. T. White, M. Najm, A. Boswell, F. P. Orfino, M. Dutta and E. Kjeang, *J. Electrochem. Soc.*, 2021, **168**, 034521.
363 S. H. Eberhardt, F. Marone, M. Stampanoni, F. N. Büchi and T. J. Schmidt, *J. Synchrotron Radiat.*, 2014, **21**, 1319–1326.
364 S. Pollastri, M. Bogar, R. Fiala, H. Amenitsch, Y. Yakovlev, A. Lavacchi, G. Aquilanti and V. Matolin, *Int. J. Hydrogen Energy*, 2022, **47**, 8799–8810.
365 Y. Cheng, J. Zhang, X. Wu, C. Tang, S. Yang, P. Su, L. Thomsen, F. Zhao, S. Lu, J. Liu and S. P. Jiang, *Nano Energy*, 2021, **80**, 105534.
366 Y. Cheng, M. Wang, S. Lu, C. Tang, X. Wu, J.-P. Veder, B. Johannessen, L. Thomsen, J. Zhang, S. Yang, S. Wang and S. P. Jiang, *Appl. Catal., B*, 2021, **284**, 119717.
367 Y. Ji, Y. il Cho, Y. Jeon, C. Lee, D.-H. Park and Y.-G. Shul, *Appl. Catal., B*, 2017, **204**, 421–429.
368 C. Roth, S. Kaserer, C. Brieger, K. M. Caldwell, J. Melke and D. E. Ramaker, *ECS Trans.*, 2015, **69**, 147–156.
369 A. S. Leach, J. Hack, M. Amboage, S. Diaz-Moreno, H. Huang, P. L. Cullen, M. Wilding, E. Magliocca, T. S. Miller, C. A. Howard, D. J. L. Brett, P. R. Shearing,

Open Access Article. Published on 07 March 2024. Downloaded on 1/20/2026 7:35:49 PM. This article is licensed under a Creative Commons Attribution 3.0 Unported Licence.

P. F. McMillan, A. E. Russell and R. Jervis, *J. Phys.: Condens.Matter*, 2021, **33**, 314002.
370 H.-Y. Park, I. Y. Cha, Y.-H. Chung, M. K. Cho, S. J. Yoo, H.-J. Kim, D. Henkensmeier, J. Y. Kim, S. W. Nam and J. H. Jang, *ECS Meet. Abstr.*, 2015, MA2015-01, p.1855.
371 B. F. Gomes, M. Prokop, T. Bystron, R. Loukrakpam, J. Melke, C. M. S. Lobo, M. Fink, M. Zhu, E. Voloshina, M. Kutter, H. Hoffmann, K. V. Yusenko, A. G. Buzanich, B. Röder, K. Bouzek, B. Paulus and C. Roth, *ACS Catal.*, 2022, **12**, 11472–11484.
372 Q. He, B. Shyam, M. Nishijima, D. Ramaker and S. Mukerjee, *J. Phys. Chem. C*, 2013, **117**, 4877–4887.
373 K. Higashi, S. Takao, G. Samjeské, H. Matsui, M. Tada, T. Uruga and Y. Iwasawa, *Phys. Chem. Chem. Phys.*, 2020, **22**, 18919–18931.
374 H. Matsui, N. Ishiguro, Y. Tan, N. Maejima, Y. Muramoto, T. Uruga, K. Higashi, D. Nguyen, H. Dam, G. Samjeské and M. Tada, *ChemNanoMat*, 2022, **8**(4), e202200008.
375 H. Matsui, S. Takao, K. Higashi, T. Kaneko, G. Samjeské, T. Uruga, M. Tada and Y. Iwasawa, *ACS Appl. Mater. Interfaces*, 2022, **14**, 6762–6776.
376 T. Uruga, M. Tada, O. Sekizawa, Y. Takagi, T. Yokoyama and Y. Iwasawa, *Chem. Rec.*, 2019, **19**, 1444–1456.
377 H. Park, D.-K. Kim, H. Kim, S. Oh, W. S. Jung and S.-K. Kim, *Appl. Surf. Sci.*, 2020, **510**, 145444.
378 N. Üregen, K. Pehlivanoğlu, Y. Özdemir and Y. Devrim, *Int. J. Hydrogen Energy*, 2017, **42**, 2636–2647.
379 I. I. Ponomarev, K. M. Skupov, A. V. Naumkin, V. G. Basu, O. M. Zhigalina, D. Y. Razorenov, I. I. Ponomarev and Y. A. Volkova, *RSC Adv.*, 2019, **9**, 257–267.
380 D. Batet, F. T. Zohra, S. B. Kristensen, S. J. Andreasen and L. Diekhöner, *Appl. Energy*, 2020, **277**, 115588.
381 T. Ossiander, C. Heinzl, S. Gleich, F. Schönberger, P. Völk, M. Welsch and C. Scheu, *J. Membr. Sci.*, 2014, **454**, 12–19.
382 I. Martens, R. Chattot, M. Rasola, M. V. Blanco, V. Honkimäki, D. Bizzotto, D. P. Wilkinson and J. Drnec, *ACS Appl. Energy Mater.*, 2019, **2**, 7772–7780.
383 I. Martens, R. Chattot and J. Drnec, *J. Power Sources*, 2022, **521**, 230851.
384 I. Martens, A. Vamvakeros, N. Martinez, R. Chattot, J. Pusa, M. V. Blanco, E. A. Fisher, T. Asset, S. Escribano, F. Micoud, T. Starr, A. Coelho, V. Honkimäki, D. Bizzotto, D. P. Wilkinson, S. D. M. Jacques, F. Maillard, L. Dubau, S. Lyonnard, A. Morin and J. Drnec, *ACS Energy Lett.*, 2021, **6**, 2742–2749.
385 P. Trtik and E. H. Lehmann, *J. Phys.: Conf. Ser.*, 2016, **746**, 012004.
386 M. Grosse and N. Kardjilov, *Phys. Procedia*, 2017, **88**, 266–274.
387 N. Kardjilov, I. Manke, R. Woracek, A. Hilger and J. Banhart, *Mater. Today*, 2018, **21**, 652–672.
388 T. A. Trabold, J. P. Owejan, D. L. Jacobson, M. Arif and P. R. Huffman, *Int. J. Heat Mass Transfer*, 2006, **49**, 4712–4720.
389 Y. Wu, J. I. S. Cho, T. P. Neville, Q. Meyer, R. Ziesche, P. Boillat, M. Cochet, P. R. Shearing and D. J. L. Brett, *J. Power Sources*, 2018, **399**, 254–263.
390 A. Iranzo and P. Boillat, *Int. J. Hydrogen Energy*, 2014, **39**, 17240–17245.
391 N. Kulkarni, J. I. S. Cho, L. Rasha, R. E. Owen, Y. Wu, R. Ziesche, J. Hack, T. Neville, M. Whiteley, N. Kardjilov, H. Markötter, I. Manke, P. R. Shearing and D. J. L. Brett, *J. Power Sources*, 2019, **439**, 227074.
392 Q. Meyer, S. Ashton, P. Boillat, M. Cochet, E. Engebretsen, D. P. Finegan, X. Lu, J. J. Bailey, N. Mansor, R. Abdulaziz, O. O. Taiwo, R. Jervis, S. Torija, P. Benson, S. Foster, P. Adcock, P. R. Shearing and D. J. L. Brett, *Electrochim. Acta*, 2016, **211**, 478–487.
393 P. Boillat, D. Kramer, B. C. Seyfang, G. Frei, E. Lehmann, G. G. Scherer, A. Wokaun, Y. Ichikawa, Y. Tasaki and K. Shinohara, *Electrochem. Commun.*, 2008, **10**, 546–550.
394 M. Siegwart, F. Huang, M. Cochet, T. J. Schmidt, J. Zhang and P. Boillat, *J. Electrochem. Soc.*, 2020, **167**, 064510.
395 J. Biesdorf, P. Oberholzer, F. Bernauer, A. Kaestner, P. Vontobel, E. H. Lehmann, T. J. Schmidt and P. Boillat, *Phys. Rev. Lett.*, 2014, **112**, 248301.
396 P. Stahl, J. Biesdorf, P. Boillat and K. A. Friedrich, *Fuel Cells*, 2017, **17**, 778–785.
397 P. Boillat, G. G. Scherer, A. Wokaun, G. Frei and E. H. Lehmann, *Electrochem. Commun.*, 2008, **10**, 1311–1314.
398 I. Manke, C. Hartnig, N. Kardjilov, M. Messerschmidt, A. Hilger, M. Strobl, W. Lehnert and J. Banhart, *Appl. Phys. Lett.*, 2008, **92**, 244101.
399 T. Arlt, W. Lüke, N. Kardjilov, J. Banhart, W. Lehnert and I. Manke, *J. Power Sources*, 2015, **299**, 125–129.
400 Y. Lin, T. Arlt, N. Kardjilov, I. Manke and W. Lehnert, *Energies*, 2018, **11**, 2214.
401 P. Boillat, J. Biesdorf, P. Oberholzer, A. Kaestner and T. J. Schmidt, *J. Electrochem. Soc.*, 2014, **161**, F192–F198.
402 A. Santamaria, H.-Y. Tang, J. W. Park, G.-G. Park and Y.-J. Sohn, *Int. J. Hydrogen Energy*, 2012, **37**, 10836–10843.
403 H.-Y. Tang, A. Santamaria, J. Kurniawan, J. W. Park, T.-H. Yang and Y.-J. Sohn, *J. Power Sources*, 2010, **195**, 6774–6781.
404 V. Manzi-Orezzoli, A. Mularczyk, P. Trtik, J. Halter, J. Eller, T. J. Schmidt and P. Boillat, *ACS Omega*, 2019, **4**, 17236–17243.
405 S. S. Alrwashdeh, F. M. Alsaraireh, M. A. Saraireh, H. Markötter, N. Kardjilov, M. Klages, J. Scholta and I. Manke, *AIMS Energy*, 2018, **6**, 607–614.
406 R. F. Ziesche, J. Hack, L. Rasha, M. Maier, C. Tan, T. M. M. Heenan, H. Markötter, N. Kardjilov, I. Manke, W. Kockelmann, D. J. L. Brett and P. R. Shearing, *Nat. Commun.*, 2022, **13**, 1616.
407 N. Martinez, A. Morin, Q. Berrod, B. Frick, J. Ollivier, L. Porcar, G. Gebel and S. Lyonnard, *J. Phys. Chem. C*, 2018, **122**, 1103–1108.
408 B. Hopfenmüller, R. Zorn, O. Holderer, O. Ivanova, W. Lehnert, W. Lüke, G. Ehlers, N. Jalarvo, G. J. Schneider, M. Monkenbusch and D. Richter, *J. Chem. Phys.*, 2018, **148**(20), 204906.
409 J. Malugani, M. Tachez, R. Mercier, A. Dianoux and P. Chieux, *Solid State Ionics*, 1987, **23**, 189–196.

 This journal is © The Royal Society of Chemistry 2024

Open Access Article. Published on 07 March 2024. Downloaded on 1/20/2026 7:35:49 PM. This article is licensed under a Creative Commons Attribution 3.0 Unported Licence.

410 M. Kruteva, *Adsorption*, 2021, **27**, 875–889.
411 A. Putra, H. Iwase, D. Yamaguchi, S. Koizumi, Y. Maekawa, M. Matsubayashi and T. Hashimoto, *J. Phys.: Conf. Ser.*, 2010, **247**, 012044.
412 S. Koizumi, S. Ueda, T. Inada, Y. Noda and R. A. Robinson, *J. Appl. Crystallogr.*, 2019, **52**, 791–799.
413 T. Kusano, T. Hiroi, K. Amemiya, M. Ando, T. Takahashi and M. Shibayama, *Polym. J.*, 2015, **47**, 546–555.
414 W. Yoshimune and M. Harada, *Chem. Lett.*, 2019, **48**, 487–490.
415 M. Harada, S. Takata, H. Iwase, S. Kajiya, H. Kadoura and T. Kanaya, *ACS Omega*, 2021, **6**, 15257–15263.
416 O. Holderer, M. Carmo, M. Shviro, W. Lehnert, Y. Noda, S. Koizumi, M.-S. Appavou, M. Appel and H. Frielinghaus, *Materials*, 2020, **13**, 1474.
417 O. Holderer, M. Khaneft, Y. Lin, S. Liu, A. Feoktystov, M. Kruteva, R. Zorn and W. Lehnert, *ECS Trans.*, 2017, **80**, 19–25.
418 K. Ito, T. Yamada, A. Shinohara, S. Takata and Y. Kawakita, *J. Phys. Chem. C*, 2021, **125**, 21645–21652.
419 M. Khaneft, O. Holderer, O. Ivanova, W. Lüke, E. Kentzinger, M. S. Appavou, R. Zorn and W. Lehnert, *Fuel Cells*, 2016, **16**, 406–413.
420 O. Holderer, O. Ivanova, B. Hopfenmüller, M. Zamponi, W. Maier, A. Majerus, W. Lehnert, M. Monkenbusch and R. Zorn, *Int. J. Hydrogen Energy*, 2014, **39**, 21657–21662.
421 B. Frick, L. Vilčiauskas, P. P. Deen and S. Lyonnard, *Solid State Ionics*, 2013, **252**, 26–33.
422 D. J. L. Brett, A. R. Kucernak, P. Aguiar, S. C. Atkins, N. P. Brandon, R. Clague, L. F. Cohen, G. Hinds, C. Kalyvas, G. J. Offer, B. Ladewig, R. Maher, A. Marquis, P. Shearing, N. Vasileiadis and V. Vesovic, *ChemPhysChem*, 2010, **11**, 2714–2731.
423 E. Öner, A. Öztürk and A. B. Yurtcan, *Int. J. Hydrogen Energy*, 2020, **45**, 34818–34836.
424 W. Zhang, J. Chen, G. F. Swiegers, Z.-F. Ma and G. G. Wallace, *Nanoscale*, 2010, **2**, 282–286.
425 F. Charreteur, F. Jaouen, S. Ruggeri and J.-P. Dodelet, *Electrochim. Acta*, 2008, **53**, 2925–2938.
426 P. Gode, J. Ihonen, A. Strandroth, H. Ericson, G. Lindbergh, M. Paronen, F. Sundholm, G. Sundholm and N. Walsby, *Fuel Cells*, 2003, **3**, 21–27.
427 M. Holber, P. Johansson and P. Jacobsson, *Fuel Cells*, 2011, **11**, 459–464.
428 Z. Peng, P. Huguet, S. Deabate, A. Morin and A. K. Sutor, *J. Raman Spectrosc.*, 2013, **44**, 321–328.
429 S. Deabate, P. Huguet, A. Morin, G. Gebel, Y. Lanteri, Z. Peng and A.-K. Sutor, *Fuel Cells*, 2014, **14**, 677–693.
430 H. Nishiyama, S. Takamuku, K. Oshikawa, S. Lacher, A. Iiyama and J. Inukai, *J. Phys. Chem. C*, 2020, **124**, 9703–9711.
431 V. G. Zhigalina, O. M. Zhigalina, I. I. Ponomarev, K. M. Skupov, D. Y. Razorenov, I. I. Ponomarev, N. A. Kiselev and G. Leitinger, *CrystEngComm*, 2017, **19**, 3792–3800.
432 R. Wang, Z. Chang, Z. Fang, T. Xiao, Z. Zhu, B. Ye, C. Xu and J. Cheng, *Int. J. Hydrogen Energy*, 2020, **45**, 28190–28195.
433 P. Ghosh, S. Mandal, S. Majumdar, A. Sarkar, S. Ganguly and K. Kargupta, *Int. J. Hydrogen Energy*, 2020, **45**, 16708–16723.
434 F. Mack, S. Heissler, R. Laukenmann and R. Zeis, *J. Power Sources*, 2014, **270**, 627–633.
435 A. Haug, H. Renate, M. Schulze, G. Schiller and K. A. Friedrich, in *PEM Fuel Cell Diagnostic Tools*, CRC Press, 2011, pp. 389–400.
436 G. A. Giffin, F. Conti, S. Lavina, A. Majerus, G. Pace, C. Korte, W. Lehnert and V. Di Noto, *Int. J. Hydrogen Energy*, 2014, **39**, 2776–2784.
437 M. Wilhelm, M. Jeske, R. Marschall, W. L. Cavalcanti, P. Tölle, C. Köhler, D. Koch, T. Frauenheim, G. Grathwohl, J. Caro and M. Wark, *J. Membr. Sci.*, 2008, **316**, 164–175.
438 M. S. M. Yusof, A. A. Jalil, A. Ahmad, S. Triwahyono, M. H. D. Othman, T. A. T. Abdullah, M. L. Firmansyah, H. D. Setiabudi, A. Johari and W. Nabgan, *Int. J. Hydrogen Energy*, 2019, **44**, 20760–20769.
439 F. C. Nart and T. Iwasita, *Electrochim. Acta*, 1992, **37**, 385–391.
440 G. Neophytides, L. Quaroni, F. N. Büchi, A. Orfanidi, S. G. Neophytides and T. J. Schmidt, *Electrochem. Commun.*, 2013, **34**, 200–203.
441 E. Yli-Rantala, A. Pasanen, P. Kauranen, V. Ruiz, M. Borghei, E. Kauppinen, A. Oyarce, G. Lindbergh, C. Lagergren, M. Darab, S. Sunde, M. Thomassen, S. Ma-Andersen and E. Skou, *Fuel Cells*, 2011, **11**, 715–725.
442 V. Bandlamudi, P. Bujlo, C. Sita and S. Pasupathi, *Mater. Today: Proc.*, 2018, **5**, 10602–10610.
443 K. Tüber, D. Pócza and C. Hebling, *J. Power Sources*, 2003, **124**, 403–414.
444 A. Hakenjos, H. Muenter, U. Wittstadt and C. Hebling, *J. Power Sources*, 2004, **131**, 213–216.
445 X. G. Yang, F. Y. Zhang, A. L. Lubawy and C. Y. Wang, *Electrochem. Solid-State Lett.*, 2004, **7**, A408.
446 X. Liu, H. Guo and C. Ma, *J. Power Sources*, 2006, **156**, 267–280.
447 M. Rahimi-Esbo, A. Ramiar, A. A. Ranjbar and E. Alizadeh, *Int. J. Hydrogen Energy*, 2017, **42**, 11673–11688.
448 M. I. Rosli, D. J. Borman, D. B. Ingham, M. S. Ismail, L. Ma and M. Pourkashanian, *J. Fuel Cell Sci. Technol.*, 2010, **7**, 1–7.
449 C.-Y. Hsu and F.-B. Weng, in *PEM Fuel Cell Diagnostic Tools*, CRC Press, 2011, pp. 209–227.
450 N. A. David, P. M. Wild, J. Jensen, T. Navessin and N. Djilali, *J. Electrochem. Soc.*, 2010, **157**, B1173.
451 N. David, K. Von Schilling, P. M. Wild and N. Djilali, *Int. J. Hydrogen Energy*, 2014, **39**, 17638–17644.
452 Y. P. Patil, T. A. P. Seery, M. T. Shaw and R. S. Parnas, *Ind. Eng. Chem. Res.*, 2005, **44**, 6141–6147.
453 V. Prabhakaran, C. G. Arges and V. Ramani, *Proc. Natl. Acad. Sci. U. S. A.*, 2012, **109**, 1029–1034.
454 J. F. Botero-Cadavid, P. Wild and N. Djilali, *Electrochim. Acta*, 2014, **129**, 416–424.
455 C. Y. Lee, Y. C. Chiang, F. B. Weng, S. C. Li, P. H. Wu and H. I. Yueh, *Renewable Energy*, 2017, **108**, 126–131.

Open Access Article. Published on 07 March 2024. Downloaded on 1/20/2026 7:35:49 PM. This article is licensed under a Creative Commons Attribution 3.0 Unported Licence.

456 S. Wu, W. Cheng, Y. Qiu, Z. Li, S. Shuang and C. Dong, *Sens. Actuators, B*, 2010, **144**, 255–259.
457 O. Belhadj Miled, D. Grosso, C. Sanchez and J. Livage, *J. Phys. Chem. Solids*, 2004, **65**, 1751–1755.
458 J. Robinson, P. Shearing and D. Brett, *J. Imaging*, 2016, **2**, 2.
459 L. Dubau, L. Castanheira, M. Chatenet, F. Maillard, J. Dillet, G. Maranzana, S. Abbou, O. Lottin, G. De Moor, A. El Kaddouri, C. Bas, L. Flandin, E. Rossinot and N. Caqué, *Int. J. Hydrogen Energy*, 2014, **39**, 21902–21914.
460 R. Shimoi, M. Masuda, K. Fushinobu, Y. Kozawa and K. Okazaki, *J. Energy Resour. Technol.*, 2004, **126**, 258–261.
461 A. Hakenjos and C. Hebling, *J. Power Sources*, 2005, **145**, 307–311.
462 H. Guo, M. H. Wang, J. X. Liu, Z. H. Nie, F. Ye and C. F. Ma, *J. Power Sources*, 2015, **273**, 775–783.
463 M. M. Daino, Z. Lu, J. M. LaManna, J. P. Owejan, T. A. Trabold and S. G. Kandlikar, *Electrochem. Solid-State Lett.*, 2011, **14**, B51.
464 J. Scholta, M. Messerschmidt, L. Jörissen and C. Hartnig, *J. Power Sources*, 2009, **190**, 83–85.
465 H. Becker, T. Bacquart, M. Perkins, N. Moore, J. Ihonen, G. Hinds and G. Smith, *J. Power Sources Adv.*, 2020, **6**, 100036.
466 L. C. Pérez, P. Koski, J. Ihonen, J. M. Sousa and A. Mendes, *J. Power Sources*, 2014, **258**, 122–128.
467 J. St-Pierre, J. Ge, Y. Zhai, T. V. Reshetenko and M. Angelo, *ECS Trans.*, 2013, **58**, 519–528.
468 D. Liang, Q. Shen, M. Hou, Z. Shao and B. Yi, *J. Power Sources*, 2009, **194**, 847–853.
469 M. M. Mench, C. Y. Wang and M. Ishikawa, *J. Electrochem. Soc.*, 2003, **150**, A1052.
470 J. Zhang, H. Zhang, J. Wu and J. Zhang, *Pem Fuel Cell Test Diagnosis*, 2013, pp. 171–185s.
471 F. Liu, B. Yi, D. Xing, J. Yu and H. Zhang, *J. Membr. Sci.*, 2003, **212**, 213–223.
472 E. Endoh, S. Terazono, H. Widjaja and Y. Takimoto, *Electrochem. Solid-State Lett.*, 2004, **7**, A209.
473 K. Teranishi, K. Kawata, S. Tsushima and S. Hirai, *Electrochem. Solid-State Lett.*, 2006, **9**, A475.
474 J. Wu, X.-Z. Yuan, J. J. Martin, H. Wang, D. Yang, J. Qiao and J. Ma, *J. Power Sources*, 2010, **195**, 1171–1176.
475 C. Noack, J. Kallo and A. K. Friedrich, *J. Appl. Electrochem.*, 2012, **42**, 833–841.
476 F. Zhou, S. J. Andreasen, S. K. Kær and D. Yu, *Int. J. Hydrogen Energy*, 2015, **40**, 2833–2839.
477 E. Jannelli, M. Minutillo and A. Perna, *Appl. Energy*, 2013, **108**, 82–91.
478 A. Jo, K. Oh, J. Lee, D. Han, D. Kim, J. Kim, B. Kim, J. Kim, D. Park, M. Kim, Y.-J. Sohn, D. Kim, H. Kim and H. Ju, *Int. J. Hydrogen Energy*, 2017, **42**, 1698–1714.
479 N. Pilinski and P. Wagner, in *4th PEFC and H2 Forum B1108*, 2013.
480 S. Liu, K. Wippermann and W. Lehnert, *Int. J. Hydrogen Energy*, 2021, **46**, 14687–14698.
481 D. Schonvogel, J. Büsselmann, H. Schmies, H. Langnickel, P. Wagner and A. Dyck, *Int. J. Hydrogen Energy*, 2021, **46**, 33934–33947.
482 S. T. Ali, Q. Li, C. Pan, J. O. Jensen, L. P. Nielsen and P. Møller, *Int. J. Hydrogen Energy*, 2011, **36**, 1628–1636.
483 X. Z. Yuan, S. Zhang, S. Ban, C. Huang, H. Wang, V. Singara, M. Fowler, M. Schulze, A. Haug, K. Andreas Friedrich and R. Hiesgen, *J. Power Sources*, 2012, **205**, 324–334.
484 L. Luo, B. Huang, Z. Cheng and Q. Jian, *Int. J. Energy Res.*, 2020, **44**, 4784–4799.
485 Y. Zhai, K. Bethune, G. Bender and R. Rocheleau, *J. Electrochem. Soc.*, 2012, **159**, B524–B530.
486 P. Marocco, K. Sundseth, T. Aarhaug, A. Lanzini, M. Santarelli, A. O. Barnett and M. Thomassen, *J. Power Sources*, 2021, **483**, 1–38.
487 H. Yu, J. M. Roller, S. Kim, Y. Wang, D. Kwak and R. Maric, *J. Electrochem. Soc.*, 2014, **161**, F622–F627.
488 S. Liu, M. Rasinski, Y. Lin, K. Wippermann, A. Everwand and W. Lehnert, *Electrochim. Acta*, 2018, **289**, 354–362.
489 K. Hengge, C. Heinzl, M. Perchthaler, D. Varley, T. Lochner and C. Scheu, *J. Power Sources*, 2017, **364**, 437–448.
490 M. Prokop, M. Vesely, P. Capek, M. Paidar and K. Bouzek, *Electrochim. Acta*, 2022, **413**, 140133.
491 M. Prokop, P. Capek, M. Vesely, M. Paidar and K. Bouzek, *Electrochim. Acta*, 2022, **413**, 140121.
492 X. Liu, K. Park, M. So, S. Ishikawa, T. Terao, K. Shinohara, C. Komori, N. Kimura, G. Inoue and Y. Tsuge, *J. Power Sources Adv.*, 2022, **14**, 100084.
493 K. Sasiwimonrit and W.-C. Chang, *Int. J. Hydrogen Energy*, 2020, **45**, 14491–14499.
494 F. Seland, T. Berning, B. Børresen and R. Tunold, *J. Power Sources*, 2006, **160**, 27–36.
495 H. Su, C. Felix, O. Barron, P. Bujlo, B. J. Bladergroen, B. G. Pollet and S. Pasupathi, *Electrocatalysis*, 2014, **5**, 361–371.
496 H. Su, Q. Xu, J. Chong, H. Li, C. Sita and S. Pasupathi, *J. Power Sources*, 2017, **341**, 302–308.
497 D. Yao, W. Zhang, Q. Ma, Q. Xu, S. Pasupathi and H. Su, *J. Power Sources*, 2019, **426**, 124–133.
498 M.-J. Choo, K.-H. Oh, H.-T. Kim and J.-K. Park, *ChemSusChem*, 2014, **7**, 2335–2341.
499 W. Xiao, Z. Xia, H. Li, R. Sun, S. Wang and G. Sun, *Energy Technol.*, 2020, **8**, 2000085.
500 Z. Jabbari, B. Nassernejad, N. Fallah, M. Javanbakht and N. Afsham, *Surf. Eng.*, 2019, **35**, 1013–1020.
501 Y. Özdemir, N. Özkan and Y. Devrim, *Electrochim. Acta*, 2017, **245**, 1–13.
502 A. Orfanidi, M. K. Daletou and S. G. Neophytides, *Appl. Catal., B*, 2011, **106**, 379–389.
503 A. Taniguchi, T. Akita, K. Yasuda and Y. Miyazaki, *Int. J. Hydrogen Energy*, 2008, **33**, 2323–2329.
504 A. Taniguchi, T. Akita, K. Yasuda and Y. Miyazaki, *J. Power Sources*, 2004, **130**, 42–49.
505 Y. Kiros, *Int. J. Electrochem. Sci.*, 2007, **2**, 285–300.
506 K. Wikander, H. Ekström, A. E. C. Palmqvist and G. Lindbergh, *Electrochim. Acta*, 2007, **52**, 6848–6855.
507 L. Yan, Y. Hu, X. Zhang and B. Yue, *Annu. Rep. NMR Spectrosc.*, 2016, **88**, 149–213.
508 S. Suarez and S. Greenbaum, *Chem. Rec.*, 2010, **10**, 377–393.

 This journal is © The Royal Society of Chemistry 2024

Open Access Article. Published on 07 March 2024. Downloaded on 1/20/2026 7:35:49 PM. This article is licensed under a Creative Commons Attribution 3.0 Unported Licence.

509 M. Robert, A. El Kaddouri, J.-C. Perrin, S. Leclerc and O. Lottin, *J. Electrochem. Soc.*, 2018, **165**, F3209–F3216.
510 J. Healy, C. Hayden, T. Xie, K. Olson, R. Waldo, M. Brundage, H. Gasteiger and J. Abbott, *Fuel Cells*, 2005, **5**, 302–308.
511 C. Simari, G. Potsi, A. Policicchio, I. Perrotta and I. Nicotera, *J. Phys. Chem. C*, 2016, **120**, 2574–2584.
512 F. Xu, S. Leclerc, D. Stemmelen, J.-C. Perrin, A. Retournard and D. Canet, *J. Membr. Sci.*, 2017, **536**, 116–122.
513 E. Galitskaya, A. F. Privalov, M. Weigler, M. Vogel, A. Kashin, M. Ryzhkin and V. Sinitsyn, *J. Membr. Sci.*, 2020, **596**, 117691.
514 S. Tsushima, T. Ikeda, T. Koido and S. Hirai, *J. Electrochem. Soc.*, 2010, **157**, B1814.
515 T. Kotaka, S. Tsushima and S. Hirai, *ECS Trans.*, 2007, **11**, 445–450.
516 J. Bedet, G. Maranzana, S. Leclerc, O. Lottin, C. Moyne, D. Stemmelen, P. Mutzenhardt and D. Canet, *Int. J. Hydrogen Energy*, 2008, **33**, 3146–3149.
517 K. Ogawa, Y. Yokouchi, T. Haishi and K. Ito, *J. Magn. Reson.*, 2013, **234**, 147–153.
518 Z. Zhang and B. Balcom, in *PEM Fuel Cell Diagnostic Tools*, CRC Press, 2011, pp. 229–254.
519 Y. Liu, Y. Gu and X. Yu, *Quant. Imaging Med. Surg.*, 2017, **7**, 707–716.
520 R. Brown, O. Khegai and P. Parasoglou, *Sci. Rep.*, 2016, **6**, 30568.
521 U.S. Department of Energy, *3.4 Fuel Cells - Multi-Year Research, Development, and Demonstration Plan*, 2016.
522 The European Commission, 2021.
523 A. Bisello, E. Colombo, A. Baricci, C. Rabissi, L. Guetaz, P. Gazdzicki and A. Casalegno, *J. Electrochem. Soc.*, 2021, **168**, 054501.
524 Y. Nosaka, K. Ohtaka, N. Ohguri and A. Y. Nosaka, *J. Electrochem. Soc.*, 2011, **158**, B430.
525 F. D. Coms, *ECS Trans.*, 2008, **16**, 235–255.
526 K. H. Wong and E. Kjeang, *J. Electrochem. Soc.*, 2014, **161**, F823–F832.
527 M. Inaba, T. Kinumoto, M. Kiriake, R. Umebayashi, A. Tasaka and Z. Ogumi, *Electrochim. Acta*, 2006, **51**, 5746–5753.
528 J. W. Frisk, M. T. Hicks, R. T. Atanasoski, W. M. Boand, A. K. Schmoeckel and M. J. Kurkowski, in *2004 Fuel Cell Seminar*, San Antonio, TX, November, 2004.
529 H. Liu, M. G. George, R. Banerjee, N. Ge, J. Lee, D. Muirhead, P. Shrestha, S. Chevalier, J. Hinebaugh, R. Zeis, M. Messerschmidt, J. Scholta and A. Bazylak, *J. Electrochem. Soc.*, 2017, **164**, F704–F713.
530 T. Arlt, M. Klages, M. Messerschmidt, J. Scholta and I. Manke, *Energy*, 2017, **118**, 502–511.
531 R. Mukundan, J. R. Davey, K. Rau, D. A. Langlois, D. Spernjak, J. D. Fairweather, K. Artyushkova, R. Schweiss and R. L. Borup, *ECS Trans.*, 2013, **58**, 919–926.
532 G. Athanasaki, N. Chauhan, R. Ahmad and A. M. Kannan, *Int. J. Hydrogen Energy*, 2021, **46**, 31754–31763.
533 V. Stanic, *ECS Proc*, 2004, **21**, 391–401.
534 A. Jung, I. M. Kong, C. Y. Yun and M. S. Kim, *J. Membr. Sci.*, 2017, **523**, 138–143.
535 R. Lin, E. Gülzow, M. Schulze and K. A. Friedrich, *J. Electrochem. Soc.*, 2011, **158**, B11.
536 C. Lim, L. Ghassemzadeh, F. Van Hove, M. Lauritzen, J. Kolodziej, G. G. Wang, S. Holdcroft and E. Kjeang, *J. Power Sources*, 2014, **257**, 102–110.
537 A. Kusoglu and A. Z. Weber, *J. Electrochem. Soc.*, 2014, **161**, E3311–E3322.
538 H. Tang, Z. Qi, M. Ramani and J. F. Elter, *J. Power Sources*, 2006, **158**, 1306–1312.
539 A. Pandy, Z. Yang, M. Gummalla, V. V. Atrazhev, N. Y. Kuzminyh, V. I. Sultanov and S. Burlatsky, *J. Electrochem. Soc.*, 2013, **160**, F972–F979.
540 H. Schulenburg, B. Schwanitz, N. Linse, G. G. Scherer, A. Wokaun, J. Krbanjevic, R. Grothausmann and I. Manke, *J. Phys. Chem. C*, 2011, **115**, 14236–14243.
541 N. Macauley, D. D. Papadias, J. Fairweather, D. Spernjak, D. Langlois, R. Ahluwalia, K. L. More, R. Mukundan and R. L. Borup, *J. Electrochem. Soc.*, 2018, **165**, F3148–F3160.
542 J. C. Meier, C. Galeano, I. Katsounaros, J. Witte, H. J. Bongard, A. A. Topalov, C. Baldizzone, S. Mezzavilla, F. Schüth and K. J. J. Mayrhofer, *Beilstein J. Nanotechnol.*, 2014, **5**, 44–67.
543 Q. Meyer, Y. Zeng and C. Zhao, *J. Power Sources*, 2019, **437**, 226922.
544 D. J. S. Sandbeck, N. M. Secher, F. D. Speck, J. E. Sørensen, J. Kibsgaard, I. Chorkendorff and S. Cherevko, *ACS Catal.*, 2020, **10**, 6281–6290.
545 P. Podleschny, U. Rost, R. Muntean, G. Marginean, A. Heinzel, V. Peinecke, I. Radev, M. Muhler and M. Brodmann, *Fuel Cells*, 2018, **18**, 586–593.
546 A. Kumar and V. Ramani, *ACS Catal.*, 2014, **4**, 1516–1525.
547 S. Thomas, C. Jeppesen, T. Steenberg, S. S. Araya, J. R. Vang and S. K. Kær, *Int. J. Hydrogen Energy*, 2017, **42**, 27230–27240.
548 Z. Guo, J. Chen, J. J. Byun, M. Perez-Page, Z. Ji, Z. Zhao and S. M. Holmes, *J. Membr. Sci.*, 2022, **641**, 119868.
549 N. Pilinski, M. Rastedt and P. Wagner, *ECS Trans.*, 2015, **69**, 323–335.
550 F. J. Pinar, M. Rastedt, N. Bruns and P. Wagner, *EFC 2013 - Proc. 5th Eur. Fuel Cell Piero Lunghi Conf.*, 2013, pp. 19–20.
551 V. Bandlamudi, P. Bujlo, V. Linkov and S. Pasupathi, *Fuel Cells*, 2019, **19**, 231–243.
552 S. Stariha, N. Macauley, B. T. Sneed, D. Langlois, K. L. More, R. Mukundan and R. L. Borup, *J. Electrochem. Soc.*, 2018, **165**, F492–F501.
553 C. H. Paik, G. S. Saloka and G. W. Graham, *Electrochem. Solid-State Lett.*, 2007, **10**, B39.
554 G. S. Harzer, J. N. Schwämmlein, A. M. Damjanović, S. Ghosh and H. A. Gasteiger, *J. Electrochem. Soc.*, 2018, **165**, F3118–F3131.
555 J. O. Leader, Y. Yue, M. R. Walluk and T. A. Trabold, *Int. J. Hydrogen Energy*, 2022, **47**, 18820–18830.
556 E. Colombo, A. Bisello, A. Casalegno and A. Baricci, *J. Electrochem. Soc.*, 2021, **168**, 054508.

Open Access Article. Published on 07 March 2024. Downloaded on 1/20/2026 7:35:49 PM.
This article is licensed under a Creative Commons Attribution 3.0 Unported Licence.

557 J. Park, L. Wang, S. G. Advani and A. K. Prasad, *Electrochim. Acta*, 2014, **120**, 30–38.
558 P. Ren, P. Pei, Y. Li, Z. Wu, D. Chen and S. Huang, *Prog. Energy Combust. Sci.*, 2020, **80**, 100859.
559 Q. Li, J. O. Jensen, R. F. Savinell and N. J. Bjerrum, *Prog. Polym. Sci.*, 2009, **34**, 449–477.
560 N. Garland, T. Benjamin and J. Kopasz, *ECS Trans.*, 2007, **11**, 923–931.
561 R. Mukundan, A. M. Baker, A. Kusoglu, P. Beattie, S. Knights, A. Z. Weber and R. L. Borup, *J. Electrochem. Soc.*, 2018, **165**, F3085–F3093.
562 J. Kerres and V. Atanasov, *Int. J. Hydrogen Energy*, 2015, **40**, 14723–14735.
563 V. Weissbecker, K. Wippermann and W. Lehnert, *J. Electrochem. Soc.*, 2014, **161**, F1437–F1447.
564 L. Tian, W. Zhang, Z. Xie, K. Peng, Q. Ma, Q. Xu, S. Pasupathi and H. Su, *Acta Phys.-Chim. Sin.*, 2020, **37**, 2009049.
565 G. Bin Jung, H. H. Chen and W. M. Yan, *J. Power Sources*, 2014, **247**, 354–359.
566 M. Tomas, P. Novotny, F. Gholami, O. Tucek and F. Marsik, *Environ. Clim. Technol.*, 2020, **24**, 529–544.
567 P. Moçotéguy, B. Ludwig, J. Scholta, Y. Nedellec, D. J. Jones and J. Rozière, *Fuel Cells*, 2010, **10**, 299–311.

This journal is © The Royal Society of Chemistry 2024